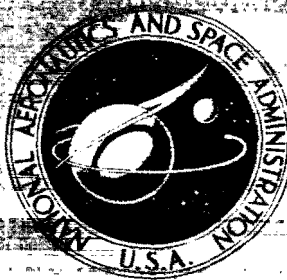


NASA CONTRACTOR REPORT



NASA CR-1

4.1
0.1

NASA CR-1543

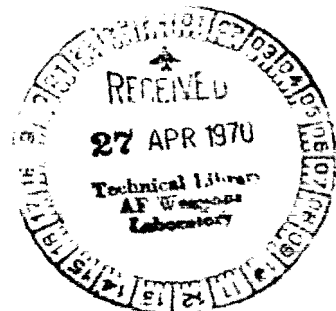
LOAN COPY: RETURN TO
AFWL (WLOL)
KIRTLAND AFB, N MEX

WAKE ANALYSIS FOR SUPERSONIC DECELERATOR APPLICATIONS

Volume I - Theoretical Analysis and Correlation
of Wind-Tunnel and Shallow-Water Tow Channel Results

by Richard A. Lau

Prepared by
GOODYEAR AEROSPACE CORPORATION
Akron, Ohio
for Langley Research Center





WAKE ANALYSIS FOR
SUPERSONIC DECELERATOR APPLICATIONS

Volume I - Theoretical Analysis and Correlation of Wind-Tunnel and
Shallow-Water Tow Channel Results

By Richard A. Lau

Distribution of this report is provided in the interest of
information exchange. Responsibility for the contents
resides in the author or organization that prepared it.

Prepared under Contract No. NAS 1-8010 by
GOODYEAR AEROSPACE CORPORATION
Akron, Ohio

for Langley Research Center

NATIONAL AERONAUTICS AND SPACE ADMINISTRATION



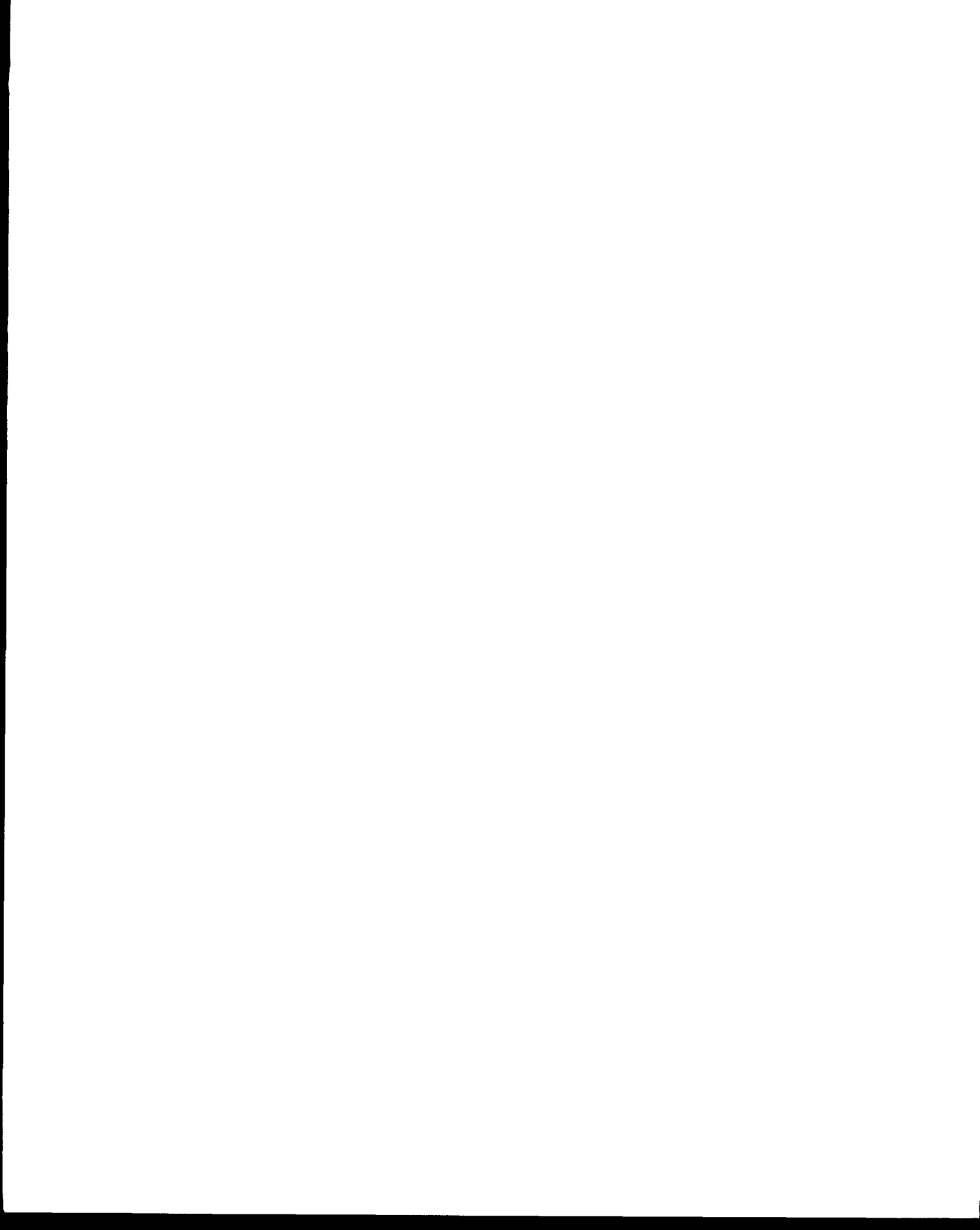
PREFACE

The work described in this document was performed by Goodyear Aerospace Corporation, Akron, Ohio under NASA Contract NAS1-8010, Supersonic Decelerator Wake Studies. Results of these studies are presented in two volumes:

Volume I - Theoretical Analysis and Correlation of
Wind Tunnel and Shallow-Water Tow
Channel Results

Volume II - Application of Gas-Hydraulic Analogy to
Shallow-Water Tow-Channel Results (NASA CR-1544)

Contractor's number for this report is GER-14330.



CONTENTS

		<u>Page</u>
PREFACE		iii
SUMMARY		xiii
<u>Section</u>	<u>Title</u>	
I	INTRODUCTION	1
II	ANALYSIS OF TOW CHANNEL RESULTS	3
	1. Purpose	3
	2. Forebody Flow Field Considerations	3
	a. Elements of the Flow Field Structure	3
	b. Data Trends and Independent Parameter Effects	6
	3. Forebody Wake Profiles	17
	a. Preliminary Discussion	17
	b. Determination of Wake Froude Number Profiles	17
	c. Comparison of Theoretical and Experimental Results Across a Near-Normal Hydraulic Jump	26
III	THEORETICAL WAKE ANALYSIS AND DEVELOPMENT	29
	1. Accomplishments	29
	2. Summary of Boundary Layer and Forebody Flow Field Calculation Procedure	29
	3. Two-Dimensional Viscous Wake Analysis	29
	a. Formulation of the Viscous Wake Problem	29
	b. General Solution of the Viscous Wake Problem	33
	c. Complete Viscous Wake Solutions for Special Cases	36
	d. Asymptotic Wake Behavior.	43
	4. Two-Dimensional Inviscid Wake Solution	47
	5. Unification of Viscous and Inviscid Wake Results	50
	a. General	50
	b. Unified Viscous Wake Results	50
	c. Unified Inviscid Wake Results	56
	6. Program Modifications for Subsonic or Incompressible Wakes	56

<u>Section</u>	<u>Title</u>	<u>Page</u>
	7. Matching Viscous and Inviscid Wakes	58
IV	CORRELATION STUDY	59
	1. General	59
	2. Correlation of Tow-Channel Results	59
	a. Correlation Methods	59
	b. Investigation of the Inviscid Flow Fields	60
	c. Boundary Layer Considerations	65
	d. Comparison of Tow-Channel and Two-Dimensional Wind-Tunnel and Theoretical Wake Results	67
	e. Correlation of Detached Air and Water Bow-Wave Shapes	68
	3. Comparison of Experimental and Theoretical Wake Results	83
	a. General	83
	b. Comparison of Two- and Three-Dimensional Profiles	83
V	CONCLUSIONS AND RECOMMENDATIONS	99
	1. Conclusions	99
	2. Recommendations	99
 <u>Appendix</u>		
A	BOUNDARY LAYER THEORY	101
B	FOREBODY FLOW FIELD PROGRAM	113
C	BOUNDARY LAYER AND WAKE COMPUTER PROGRAM	117
	LIST OF SYMBOLS	127
	LIST OF REFERENCES	131

ILLUSTRATIONS

Figure	Title	Page
1	Basic Flow Structure	4
2	Effects of Free-Stream Froude Number on Ogive-Block Data	7
3	Effects of Free-Stream Froude Number on Tow Channel Cylinder and Half-Cylinder Data	8
4	Effects of Free-Stream Froude Number on Tow Channel Wedge Data	9
5	Effects of Wedge Semiapex Angle on Tow Channel Wedge Data	10
6	Effect of Rounding Base Shoulders on Tow Channel Wedge Data ($Fr_{\infty} = 2.0$).	11
7	Effects of Angle of Attack on Bow Wave	12
8	Effects of Model Size on Approximate Wake Neck Location.	14
9	Comparison of Tow Channel Wedge Data with Theoretical Results in $\gamma = 2$ Gas	16
10	Tow Channel Froude Number Results Along Wake Centerline: Slender Wedge Method	22
11	Tow Channel Froude Number Results Along Wake Centerline: Blunt Body Method	23
12	Tow Channel Froude Number Wake Profiles Obtained with Stereo Camera/Projector	25
13	Prediction of Upstream Froude Number Values with Water Depth Contour Maps.	27
14	Viscous Wake Coordinate System	31
15	Laminar Wake Shape Factor as a Function of Form Factor for Two-Dimensional Compressible Wake.	39
16	Axial Wake Parameter versus Form Factor for a Two-Dimensional Turbulent Wake (Adiabatic Wall Case)	44

<u>Figure</u>	<u>Title</u>	<u>Page</u>
17	Axial Wake Parameter versus Form Factor for a Two-Dimensional Turbulent Wake (Cold Wall Case)	45
18	Axial Wake Parameter versus Form Factor for Two-Dimensional and Axisymmetric Wakes at $M = 3.0$	46
19	Isentropic Gas and Actual Gas Results Across a Shock Wave	61
20	Attached Bow Shock Angles at Small Deflection Angles	62
21	Static Depth and Density Ratios Across Oblique Wave as Function of Upstream Mach (Froude) Number	64
22	Comparison of Theoretical Compressible Wake and Water Wake Size for Blunted Wedge-Block-Flare Forebody	66
23	Comparison of Experimental Two-Dimensional Wind-Tunnel and Tow-Channel Predicted Wake Results for Wedge-Block Forebody	67
24	Comparison of Theoretical and Tow-Channel Predicted Wake Results	69
25	Tow-Channel Shock Shapes for 120-Deg Blunted Wedge at $M_{\infty} = 2.0$	74
26	Tow-Channel Shock Shapes for 120-Deg Blunted Wedge at $M_{\infty} = 2.2$	75
27	Tow-Channel Shock Shapes for 120-Deg Blunted Wedge at $M_{\infty} = 2.5$	76
28	Tow-Channel Shock Shapes for Circular Cylinders at $M_{\infty} = 1.5$	77
29	Tow-Channel Shock Shapes for Circular Cylinders at $M_{\infty} = 2.0$	78
30	Tow-Channel Shock Shapes for Circular Cylinders at $M_{\infty} = 2.5$	79
31	Actual and Predicted Three-Dimensional Air Shock Shapes for a 120-Deg Blunted Cone	81

<u>Figure</u>	<u>Title</u>	<u>Page</u>
32	Actual and Predicted Three-Dimensional Air Shock Shapes for a Flat Plate	82
33	Actual and Predicted Three-Dimensional Air Shock Shapes for a Sphere	82
34	Cone-Cylinder Wake Pitot Pressure Profiles at $x/D = 2.52$ ($M_{\infty} = 2.3$)	84
35	Cone-Cylinder Wake Pitot Pressure Profiles at $x/D = 5.04$ and $x/D = 7.56$ ($M_{\infty} = 2.3$)	85
36	Cone-Cylinder Wake Pitot Pressure Profiles at $x/D = 2.52$ ($M_{\infty} = 4.65$)	86
37	Cone-Cylinder Wake Pitot Pressure Profiles at $x/D = 5.04$ ($M_{\infty} = 4.65$)	87
38	Cone-Cylinder Wake Pitot Pressure Profiles at $x/D = 7.56$ ($M_{\infty} = 4.65$)	88
39	Wake Mach Number Profiles for Cone Cylinder and Wedge Block at $x/D = 2.52$	89
40	Wake Mach Number Profiles for Cone Cylinder and Wedge Block at $x/D = 5.04$	90
41	Wake Mach Number Profiles for Cone Cylinder at $x/D = 7.52$	91
42	Measured Local Wake Static Pressure for Cone-Cylinder and Wedge Block	91
43	Wake Mach Number Profiles for 120-Deg Cone and 120-Deg Wedge at $x/D = 2.5$	93
44	Wake Mach Number Profiles for 120-Deg Cone and 120-Deg Wedge at $x/D = 5.04$ and $x/D = 8.33$	94
45	Measured Local Wake Static Pressures for 120-Deg Cone and 120-Deg Wedge	95
46	Blunted Cone-Cylinder-Flare Wake Mach Number Profiles at $x/D = 5.0$	96
47	Blunted Cone-Cylinder-Flare Wake Mach Number Profiles at $x/D = 7.0$	97
48	Blunted Cone-Cylinder-Flare Wake Mach Number Profiles at $x/D = 11.0$	97

<u>Figure</u>	<u>Title</u>	<u>Page</u>
49	Free Stream Turbulence, U'/U	107
50	Boundary Layer Transition on a Blunt Cone at $M_{\infty} = 5.5$	111

TABLES

<u>Table</u>	<u>Title</u>	<u>Page</u>
I	Hydraulic Jump Coordinates and Local Froude Number Values (Stereo Camera/Projector Method).	24
II	Unified Viscous Wake Results	51
III	Unified Inviscid Wake Results	55
IV	Tow Channel Configurations and Associated Hydraulic Jump Parameters	73
V	Experimental Water Values of A and n for Shock Shape Relations	80
VI	Theoretical Values of A and n for Shock Shape Relations	81



SUMMARY

Two methods for predicting the compressible wake characteristics behind two-dimensional and axisymmetric bodies in a supersonic free stream have been investigated. The first method involves use of shallow-water tow-channel data and the mathematical relationships that exist between water with a free surface and a two-dimensional, compressible gas. The second method is theoretically developed and uses a momentum integral solution for the viscous wake and a mass flow balance across the bow shock for the inviscid wake. As part of this investigation, the theoretical solution for the two-dimensional wake was developed and the results were combined with available axisymmetric wake results into a general set of unified equations.

Predicted results obtained from both methods have been compared with experimental wind-tunnel data. Tow-channel results were found to be indicative of gas results with respect to observable flow patterns and qualitative data trends. They were generally found to be unsuitable for quantitatively predicting compressible wake characteristics; although reasonable agreement was found to exist in a limited number of cases. Theoretically predicted results were found to agree reasonably well with experimental data, although the method could be further improved with removal of certain limiting assumptions.

WAKE ANALYSIS FOR SUPERSONIC DECELERATOR APPLICATIONS

Volume 1 - Theoretical Analysis and Correlation of Wind-Tunnel and Shallow-Water Tow Channel Results

By Richard A. Lau
Goodyear Aerospace Corporation

SECTION I - INTRODUCTION

Present and future requirements for successful entry and descent into the atmosphere of earth and other planets indicate a need for improved methods of analyzing and designing trailing deceleration and stabilization devices. One aspect of primary importance to ensure the establishment of lightweight, predictable-performing designs is knowledge of the payload's trailing wake. Characteristics of the trailing wake are of importance for two reasons:

1. Ejection velocity of the decelerator pack into the wake must be sufficiently high to achieve satisfactory deployment yet must not impose an undue weight penalty on the ejection system.
2. Performance of the decelerator is inherently dependent upon the nonuniform wake characteristics that serve as the effective free-stream flow in which it must operate.

In the supersonic wake analysis program, theoretical and experimental methods of analyzing the high-speed trailing wake were investigated. The following major tasks were performed:

1. Analysis of the utility of the shallow-water tow channel for predicting characteristics of high-speed compressible wake flows
2. Development and analysis of theoretical two-dimensional wake equations
3. Unification of two-dimensional and axisymmetric wake equations into a general combined form
4. Correlation of theoretical and experimental results with wind-tunnel results

All tow-channel tests were conducted at Wright-Patterson Air Force Base, Ohio, with technical assistance and advice rendered by Mr. C. A. Babish, III, of the Flight Dynamics Laboratory (FDFR). Consultant services for the development of the theoretical wake equations were provided by Dr. R. M. Nerem of Ohio State University, Columbus, Ohio.



SECTION II - ANALYSIS OF TOW CHANNEL RESULTS

1. PURPOSE

Because trailing decelerators are typically constrained to operations in the wake of a leading payload, the problems of analysis are generally difficult and complex. Often a considerable amount of wind-tunnel testing is required even in preliminary stages of development to facilitate later selection and evaluation of the final design. The shallow-water tow channel offers substantial economic advantages over wind-tunnel testing, and its application as a screening device conceivably could reduce the time and expense of decelerator development.

A major portion of the supersonic wake analysis program was devoted to an investigation of the shallow-water tow channel and the mathematical relationships existing between (1) an incompressible fluid (water) having a free surface and (2) a two-dimensional compressible gas. The correspondence between the two fluids has been the subject of previous studies, such as that of Orlin, *et al.*,^{1, a} and has resulted in the formulation of the gas-hydraulic analogy. This analogy relates the water depth to the density, pressure, and temperature of the so-called "hydraulic gas" which is two-dimensional, isentropic, irrotational, and has a specific heat ratio, γ , of 2. Although the gas-hydraulic analogy itself is not valid for any real gas, the analogous nature of the two fluids merited further consideration. Consequently, the purpose of this investigation was to study the potential utility of the tow channel as an analytical tool in the investigation of compressible flows and as a possible screening device for candidate high-speed decelerators.

2. FOREBODY FLOW FIELD CONSIDERATIONS

a. Elements of the Flow Field Structure

The nature and structure of a high-speed (supersonic) compressible flow about a body in either gas or liquid is illustrated in Figure 1. Presented parenthetically in Figure 1 is the corresponding water terminology for supercritical flow indicating the existence of a geometrically analogous structure. In both cases, as the upstream flow approaches the body, it becomes unstable and passes through the primary wave, or jump, to the stable region on the downstream side. This wave may be attached, or it may be detached as shown.

As indicated in Figure 1, the transition across the wave occurs in a similar manner for both gasses and liquids. There are, however, several differences worth noting. First, the gaseous shock wave and the hydraulic jump are of different shapes. Theoretically, the shape of the hydraulic jump is equivalent to that incurred in the hydraulic gas. Second, the

^aSuperior numbers in the text refer to items in the List of References.

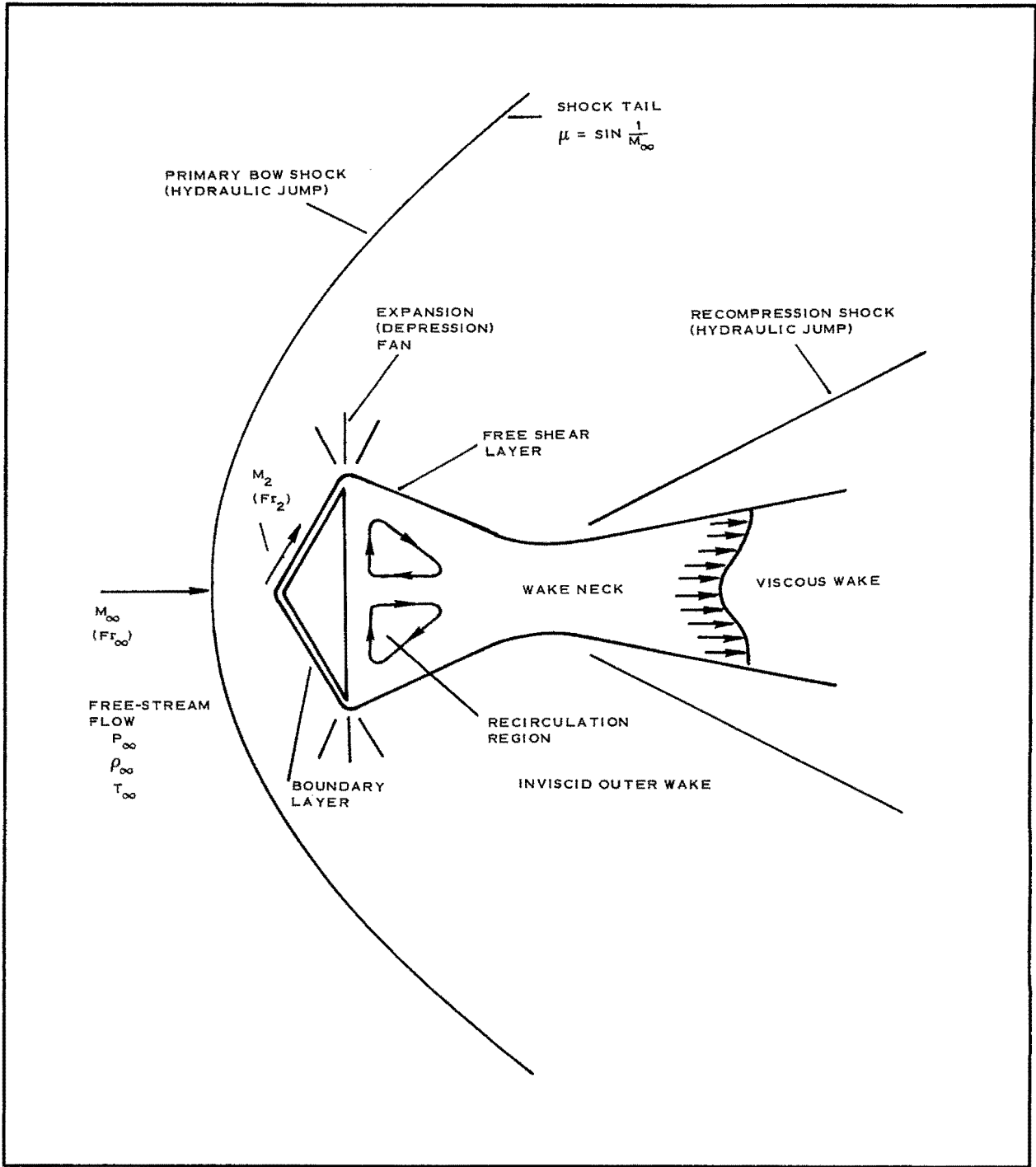


Figure 1 - Basic Flow Structure

change in internal energy across a shock wave is not equivalent to the change across a hydraulic jump. In water, the change in internal energy manifests itself by an increase in the water temperature on the downstream side. This condition has no analogous counterpart in a compressible fluid. Unlike water, however, internal energy changes in a gas result in an increase in entropy. Moreover, when the bow shock is curved, an entropy gradient is introduced on the downstream side of the shock wave; and the flow immediately behind the shock is rotational (except for the flow on the centerline) in accordance with Crocco's vorticity law. The degree of rotation is dependent upon the curvature of the bow shock and the density ratio across the shock.

These and other differences are presented and discussed in greater detail in Section IV. They are mentioned here to stress that this discussion is qualitative in nature and limited to the observable flow pattern similarities.

In the vicinity of the body in both fluids, two separate and distinct regions are formed. Immediately adjacent to the body, a boundary layer develops that is marked by various gradients. Outside the boundary layer exists a region that is inviscid. In this region, the hydraulic analogy predicts, qualitatively, the increased gas density from the free stream by an analogous rise in water level. As the flow passes the body, expansion in both fluids occurs in which the boundary layer forms the recirculating base region, the wake neck, and the downstream viscous wake. The inviscid region expands about the corner and occupies the region outside the edge of the viscous wake. In the process of expansion, the fluids perform in an analogous manner in the inviscid region. The gas undergoes a decrease in density and an increase in Mach number. In water, a corresponding level drop occurs accompanied by an increase in Froude number.^a The gas then is recompressed at the wake neck with the formation of the recompression shock. In a geometrically analogous manner, the water undergoes a rise in its level accompanied by a hydraulic jump.

Other observable flow phenomena in gases are also visually apparent in water. An example is the compression shock formed at the junction to a flare. Secondary imbedded shocks, such as the lip shock, which form at a sharp base corner and result from an over-expansion and subsequent compression of the gas, are also believed to have a typical geometrical counterpart in water. Careful analysis of water results, however, is necessary to avoid confusing capillary ripples prevalent in water with hydraulic jumps. This is particularly true in regions where secondary or weak jumps occur.

Thus, geometrically similar patterns are formed between two fluid flows about a body in supercritical flow. These patterns, however, are not equivalent, and the processes undergone are not the same. Nevertheless,

^aFroude number, as used in this report, is the ratio of local velocity in water to the surface wave propagation velocity and is analogous to Mach number in a gas.

the flow of water appears, at least, to be qualitatively indicative of the flow of a compressible gas.

b. Data Trends and Independent Parameter Effects

Some typical results obtained with the tow channel in this program are presented in the following discussion. This discussion is as qualitatively applicable to wind-tunnel test data as it is to the tow-channel test results being discussed.

Data trends resulting from changes in the Froude number, selected geometrical parameters, or angle-of-attack are presented in Figures 2 through 7. Figure 2 presents results for three ogive-block configurations. It can be seen from Figure 2 that the bow angle decreases with either an increase in Froude number or an increase in the ogive fineness ratio. The ogive shape, however, has little apparent influence on either the approximate wake neck location, as determined by the convergence point of the hydraulic jump legs (analogous to the recompression shock legs in a gas), or on the divergence angle of these legs. As might be expected, the latter two parameters increase and decrease respectively with increasing Froude number.

Example blunt body data is provided in Figure 3. Here, the primary hydraulic jump is detached in all cases. Again, the trends experienced are consistent with those obtained from wind-tunnel tests. An increase in Froude number results in a decrease in primary jump detachment distance and higher local Froude number values along the body surface. This, in turn, decreases the expansion angle which increases the magnitude of the approximate wake neck location parameter, x_0/D and reduces the magnitude of the trailing wave divergence half angle, ϵ . The difference in the x_0/D values for the cylinder and the half-cylinder can be attributed primarily to flow separation that is slightly delayed on the continuous cylindrical surface.

Flow results over slender and blunt wedges are presented in Figures 4 through 6. It is immediately apparent that the previous discussion is generally applicable to these shapes with respect to the free-stream Froude number. As indicated by Figures 4 and 5, an increase in wedge angle has an effect on data trends opposite to that of an increase in Froude number. The effects of rounding the base shoulders are shown in Figure 6. In general, the effect is small, with the approximate wake location being the most affected. Again, the trend is logical considering the mechanisms involved in flow separation.

One observed phenomenon reflected in Figures 2, 4, and 5 is the existence in the tow channel of attached normal hydraulic jumps. Such a situation is incurred for deflection angles of 10 deg and 12.66 deg at $Fr_\infty = 1.5$ as shown in Figure 4 ($\theta = 90$ deg). These often occurred at or near the critical angle between attached and detached shocks as predicted by oblique shock theory for a $\gamma = 2$ gas. The existence of attached normal jumps is not predicted by oblique shock theory, and consequently present

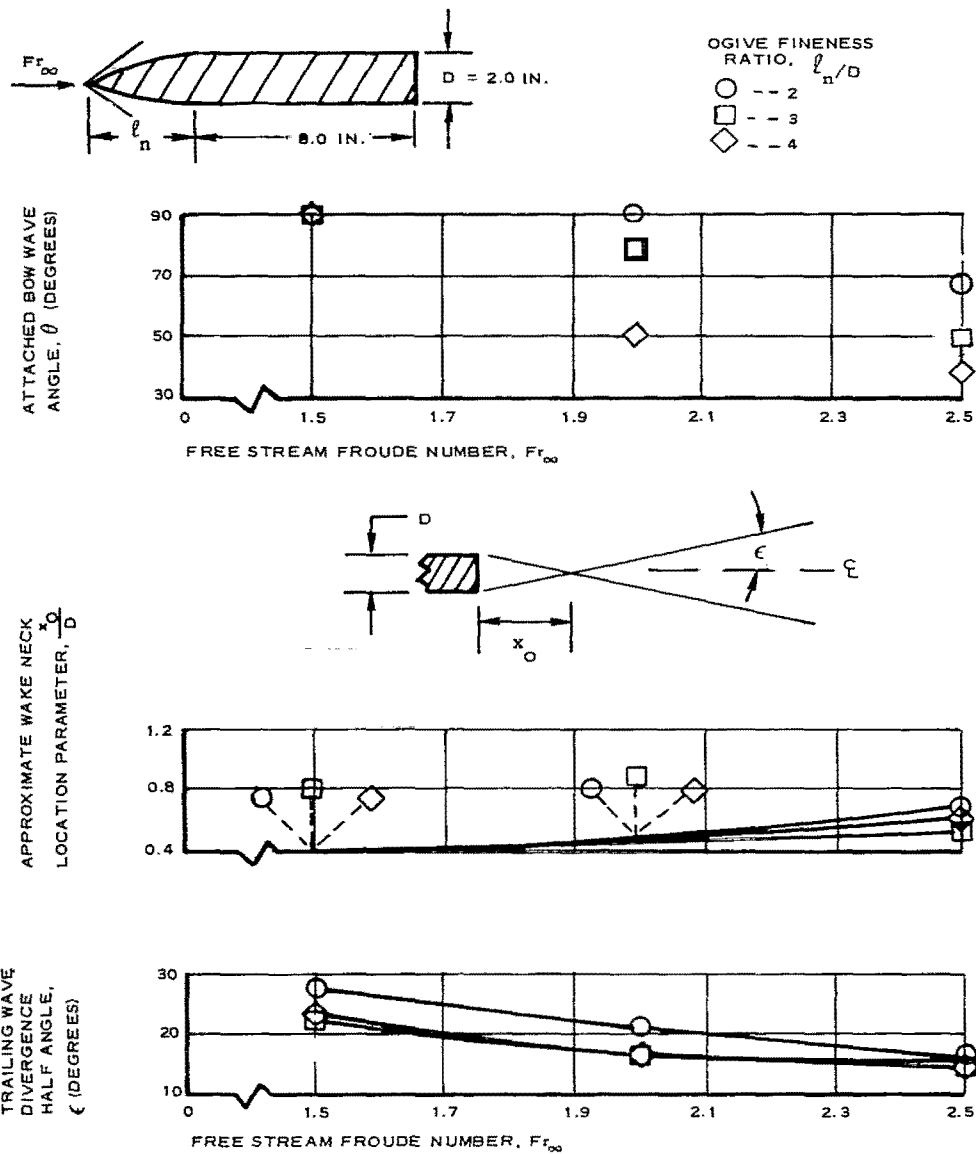


Figure 2 - Effects of Free-Stream Froude Number on Ogive-Block Data

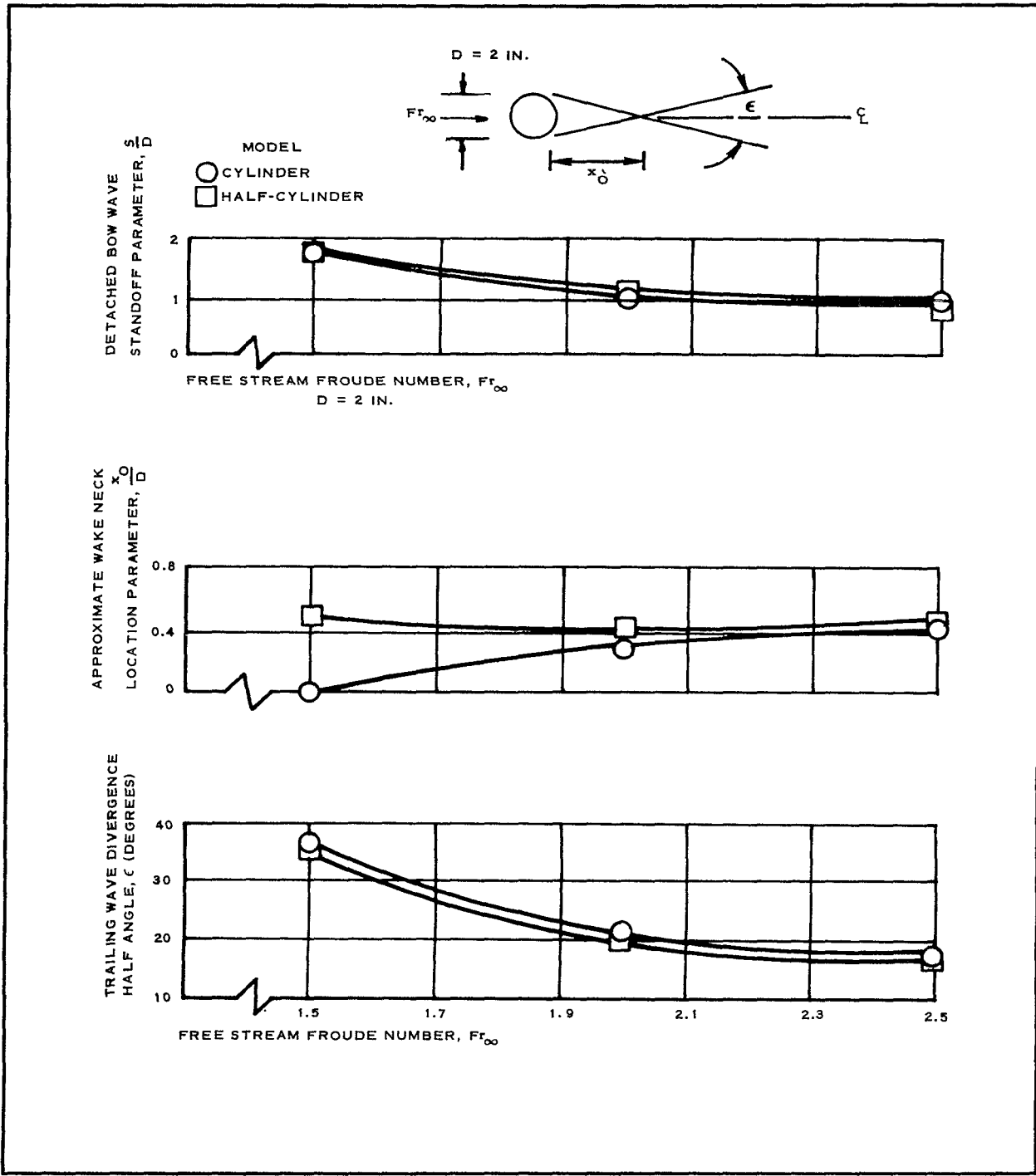


Figure 3 - Effects of Free-Stream Froude Number on Tow Channel Cylinder and Half-Cylinder Data

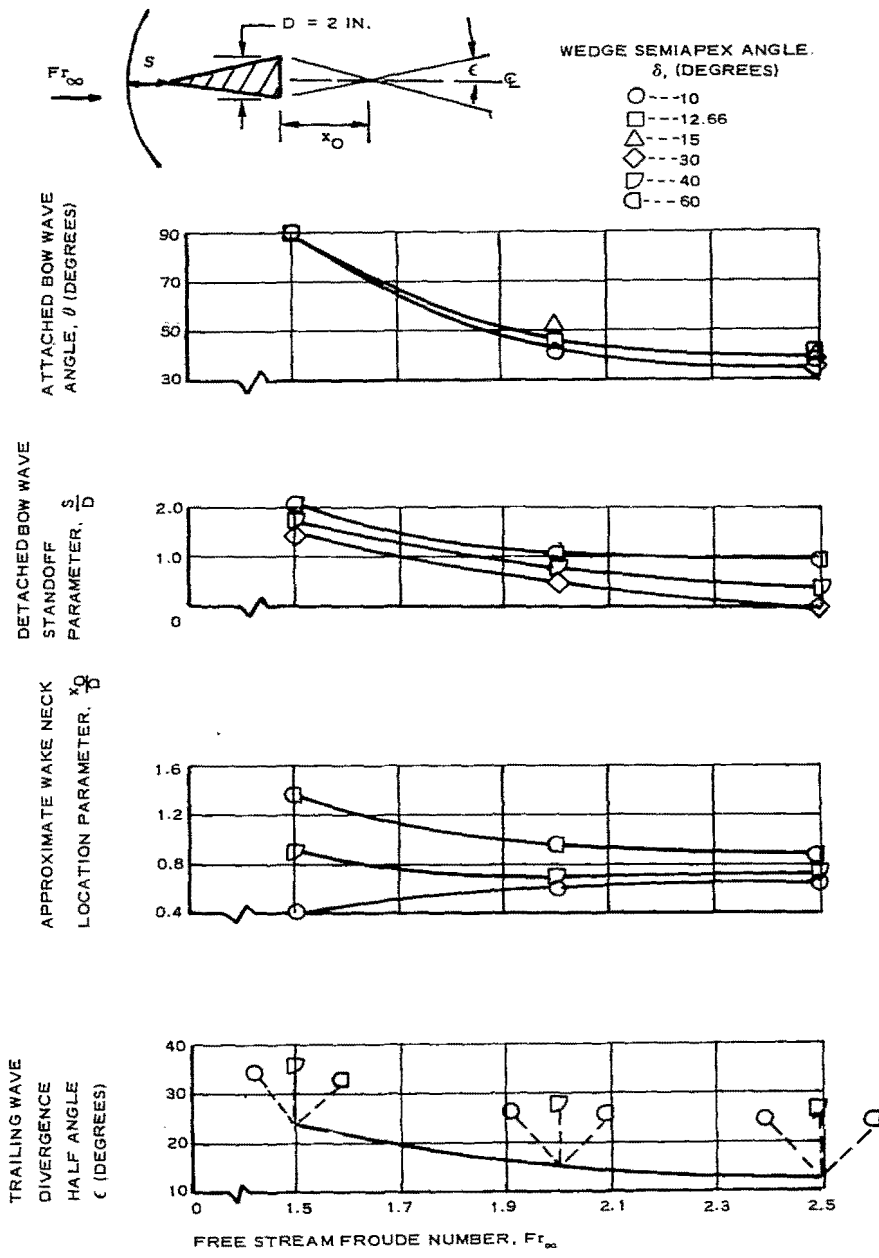


Figure 4 - Effects of Free-Stream Froude Number on Tow Channel Wedge Data

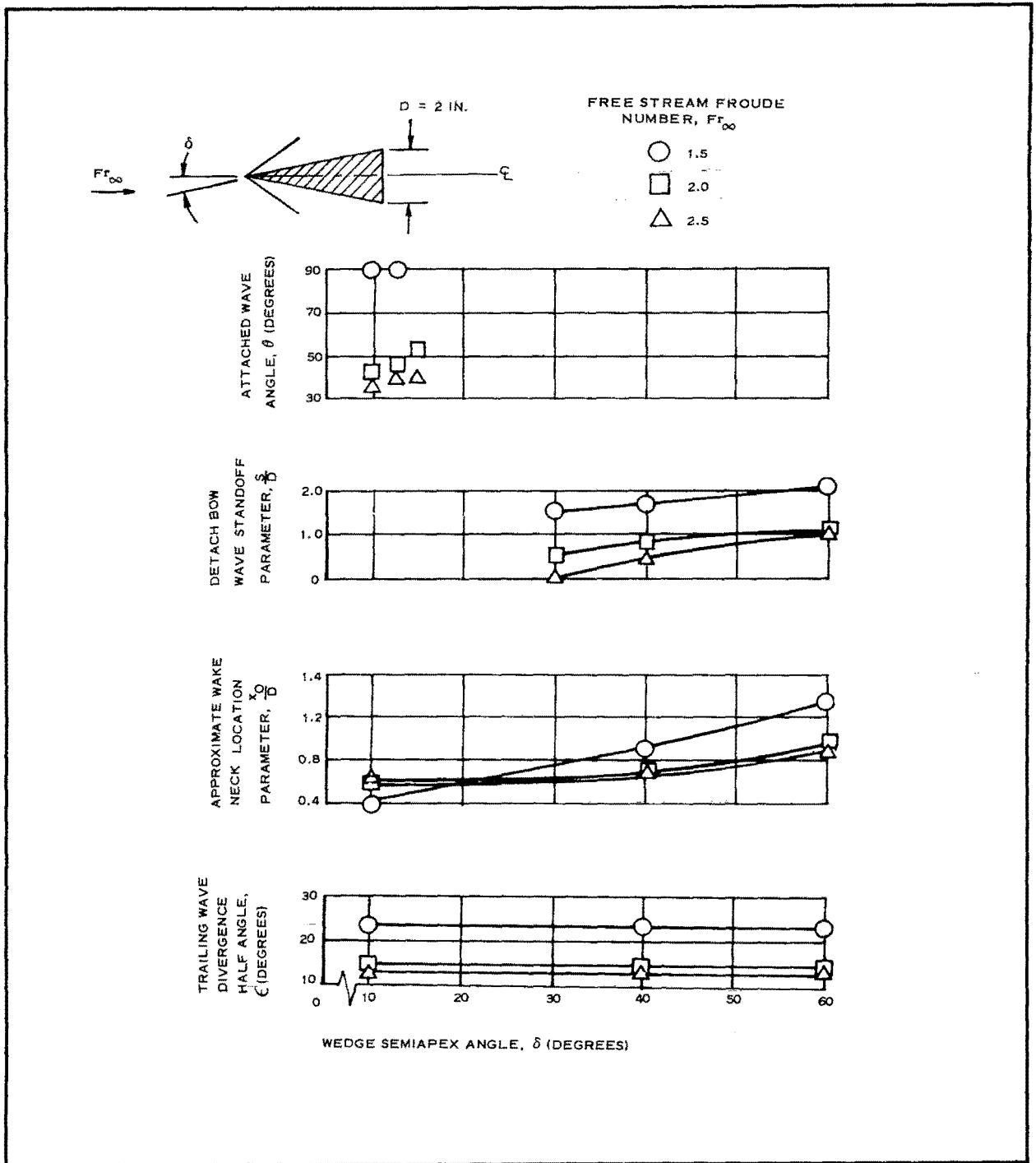


Figure 5 - Effects of Wedge Semiapex Angle on Tow Channel Wedge Data

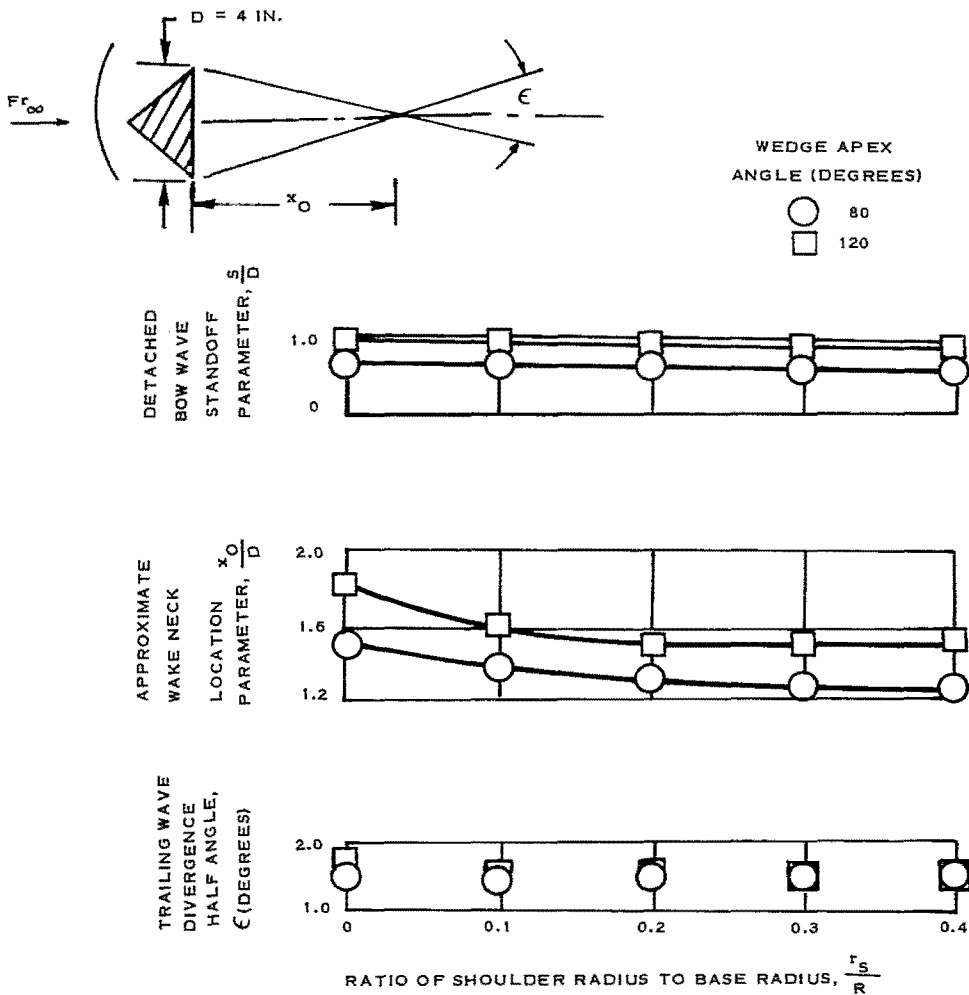
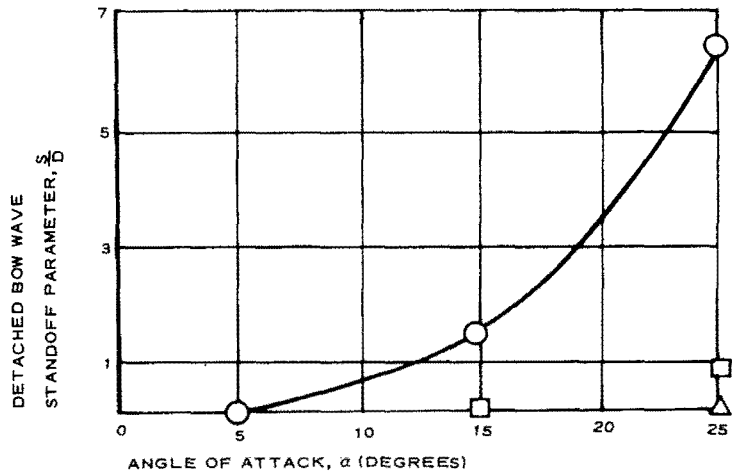
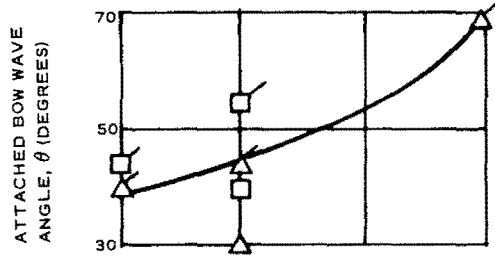
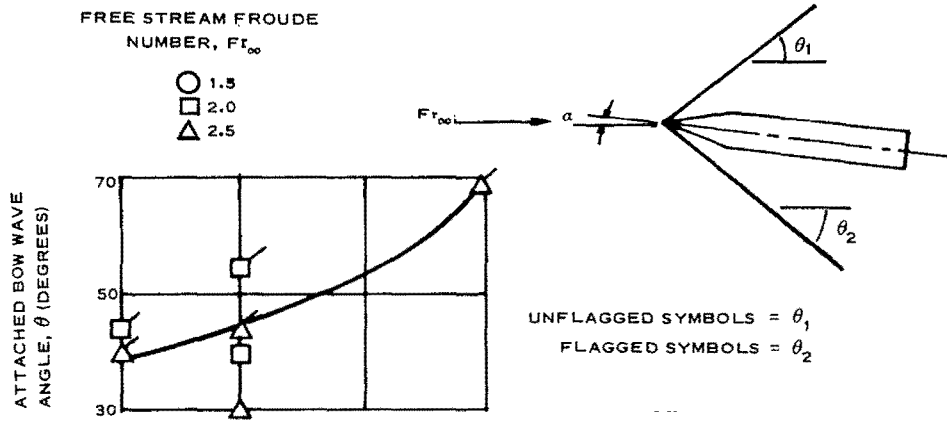
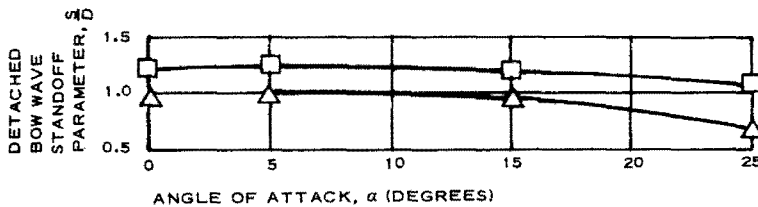


Figure 6 - Effect of Rounding Base Shoulders on Tow Channel Wedge Data ($Fr_\infty = 2.0$)



A. WEDGE-BLOCK TOW CHANNEL DATA



B. 120-DEG WEDGE TOW-CHANNEL DATA

Figure 7 - Effects of Angle of Attack on Bow Wave

an area of possible theoretical interest. In water, it appears that once the theoretical critical angle has been reached, a decrease in Froude number or an increase in wedge angle still can be tolerated without detachment of the shock wave.

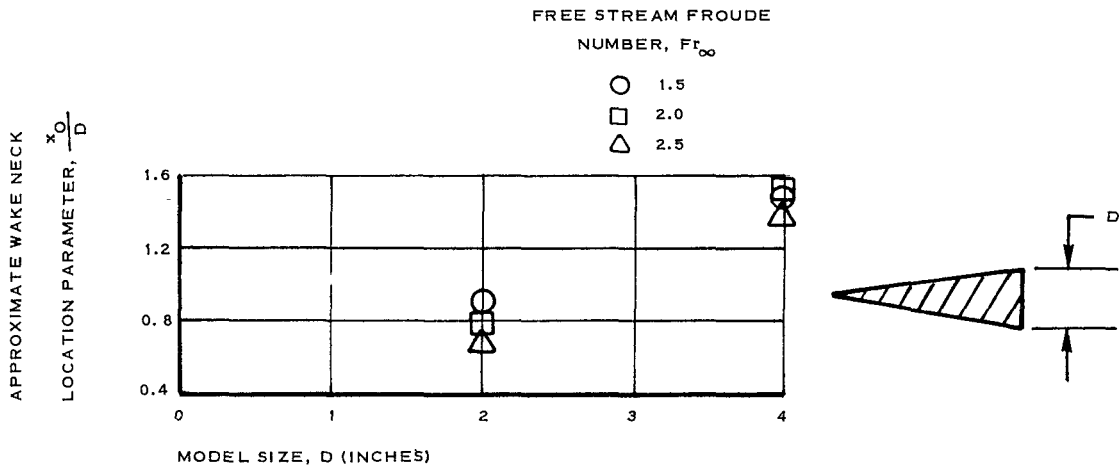
Figure 7 presents angle-of-attack effects for the indicated configurations. For the wedge-block, the data shows the hydraulic jump to be attached at small angle-of-attack values. As the angle of attack increases, the wave angle increases on the upstream side and decreases on the downstream side. It is noted that at $M = 2.5$ and $\alpha = 15$ deg, only one attached wave angle (θ_2) data point is obtained. This is consistent with gas results because the flow over the upper (downstream) surface is entirely expansionary ($\delta = 12.66$ deg). At larger angle-of-attack and smaller Froude-number values, the jump is detached as illustrated in the lower portion of Figure 7A. For the 120-deg wedge, the bow jump is detached in all cases. The general decline in stand-off distance with increased angle of attack is attributed to the combination of increasing bluntness but decreasing effective size.

Data trends presented thus far are generally consistent with results that might be anticipated from wind-tunnel experiments or theoretical predictions. These results are generally typical of similar data obtained for several other configurations in the tow channel experiments. There were, however, some observed water flow phenomena which cannot be considered even qualitatively correct for a gas. One of these is the effect of freestream water depth on the geometrical flow pattern, in particular, on the primary hydraulic jump. This effect has no counterpart in a gas. A second effect is that of model size on the base separation point.

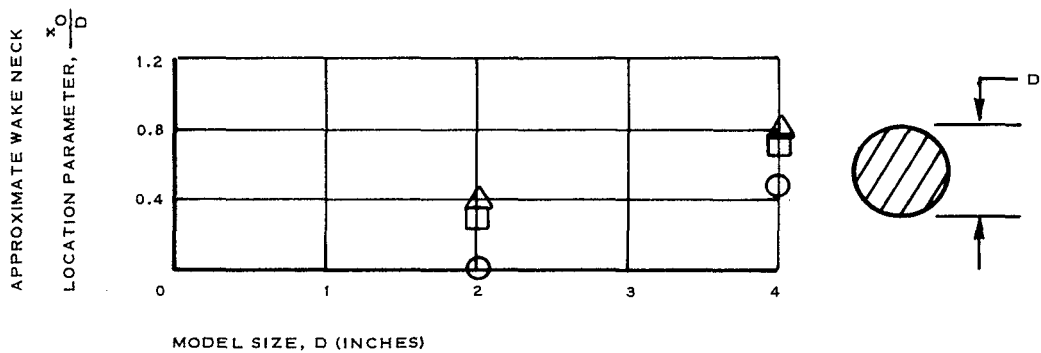
Tow channel data presented in Figure 8 show the effect of model size on x_0/D . When the nondimensional character of the dependent x_0/D parameter and the positive size effect indicated are considered, it must be concluded that such effect does, in fact, exist and that similar results in a gas would not be anticipated to the same degree. Furthermore, as indicated by the cylinder data, results were obtained in which the flow followed the body contour to the extent that the wake neck appeared to form at the base face of the body. This latter phenomena is geometrically similar to a "blown" wake; although, in this case, no trailing body is present which would alter the basic wake structure.

The size effect, in general, is attributed to a form of the "Coanda effect," in this case, the tendency of water to "wrap" itself about even sharp corners such as exist at the base of a wedge. Hence, flow separation may not occur at the base edge, for example, but may actually continue around the body (at a reduced height level, however) and finally separate from the base surface. The pattern of separation appears as if it had resulted from a much smaller model.

The Coanda effect in water is considered to result from a combination of a very low boundary layer velocity in the water and its comparatively high value of surface tension. The degree of wrapping observed appears



A - TOW CHANNEL WEDGE DATA (40-DEG SEMIAPEX ANGLE)



B - TOW CHANNEL CYLINDER DATA

Figure 8 - Effects of Model Size on Approximate Wake Neck Location

to be largely dependent on model geometry, being less pronounced on configurations having well-defined base separation points (such as exists at the base of a wedge, for example). Also, the effect is less severe on large models than on smaller models of the same geometry. Hence, from the standpoint of wake analysis, it is desirable to use as large a model as practical.

From the data in Figures 2 through 7, some direct comparisons with predicted gas results can now be made. Other comparisons, which involve a correlation analysis, are discussed in Section IV.

Some experimental and theoretical wedge data relating to the primary wave are presented in Figure 9. In Figure 9A, tow channel wave angles are compared with theoretical results for the "hydraulic gas." The theoretical values are from graphical results obtained by applying the following equation (oblique shock theory):

$$\tan \delta = (2 \cot \theta) \frac{M_{\infty}^2 \sin^2 \theta - 1}{M_{\infty}^2 (\gamma + \cos 2\theta) + 2} . \quad (1)$$

Of course γ is set equal to 2 for the "hydraulic gas" rather than to the customary value of 1.4 for air. The experimental wave angle actually exhibits some curvature with the angle at the shock tail approaching the limiting Mach angle. Accordingly, the angles used in Figure 9 are those obtained by constructing tangents to the waves in the immediate vicinity of the wedge apex. Experimental and theoretical data agree very well.

In Figure 9B, experimental and theoretical standoff distances are given for some "blunt" wedges. The theoretical data was obtained using Moeckel's geometric equation.²

$$\frac{R_B'}{S + \ell'} = \tan \beta_{\max} , \quad (2)$$

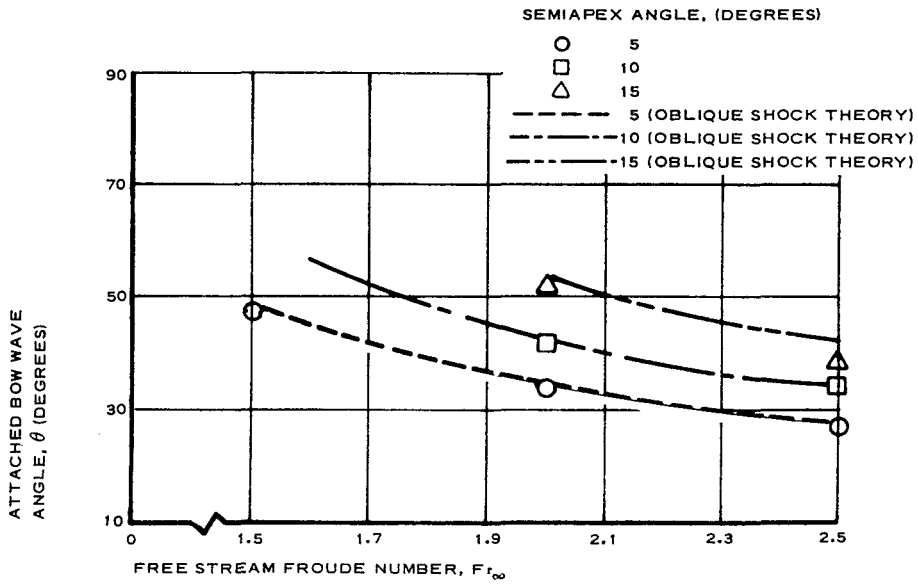
where

β_{\max} = maximum stream tube deflection at a given free-stream Mach number,

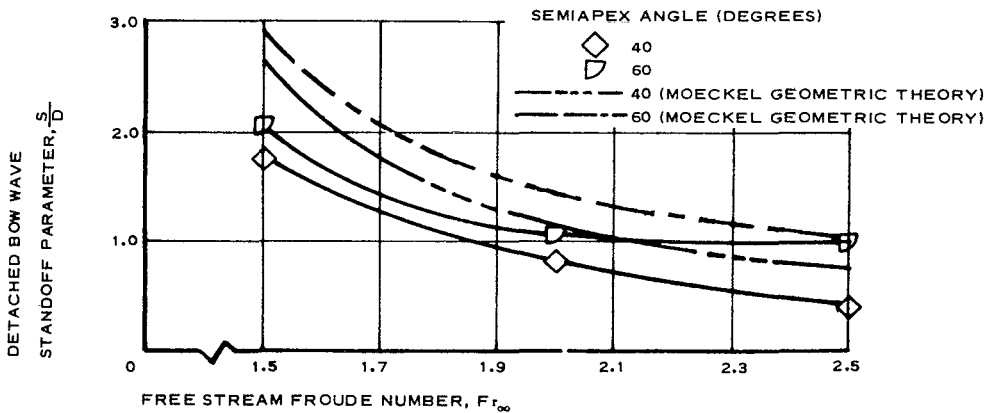
R_B' = radial dimension of body in plane containing body sonic point (the base plane for wedges, for example)

S = shock standoff distance, and

ℓ' = body length from nose to plane containing sonic point.



A - BOW WAVES ATTACHED



B - BOW WAVES DETACHED

Figure 9 - Comparison of Tow Channel Wedge Data with Theoretical Results in $\gamma = 2$ Gas

This equation is based on the assumption that body geometry forward of the sonic point is not influential in determining the combined $(s + \ell')$ value. This assumption is not completely valid because it is known from experimental data that the body shape ahead of the sonic points does have secondary effects.

A comparison of the results of Figure 9B shows that the theoretical values predict a larger standoff distance than were obtained in the tow channel; particularly at the lower Froude-number values.

3. FOREBODY WAKE PROFILES

a. Preliminary Discussion

During the course of the tow channel test program, several attempts were made to determine local Froude number values in the trailing wakes of various forebodies, because such information was potentially useful in the analysis of high-speed compressible wakes. Consideration of the shallow-water tow channel as a potential analytical tool in the investigation of high-speed wakes is not without precedent. Babish³ discusses the possibility and provides information which correctly shows, in a qualitative manner, the existence of a Froude number defect in the water wake.

To quantitatively predict compressible gas wake properties from tow-channel water data, however, the following major problem areas must be resolved:

1. Tow-channel results must be relatable to properties of a real gas as opposed to the hypothetical gas specified by the gas-hydraulic analogy.
2. Physical characteristics of the water wake may differ substantially from those obtained in a gas.
3. Satisfactory determination of the water wake characteristics must be possible.

Problem Area 3, the measurement and calculation of the viscous and inviscid water wake characteristics, is discussed in Item 3, b, below. Problem Areas 1 and 2 are discussed in Section IV.

b. Determination of Wake Froude Number Profiles

(1) Methods of Predicting Local Wake Values

Three different approaches were employed in attempting to find a satisfactory method for determining local Froude number values in the water wake.

(a) Slender Wedge Method

The first method involved placing a slender wedge (analytical wedge, 5-deg half angle) in the wake of the test body. The Froude number immediately forward of the wedge apex then was predicted from the bow wave emanating from the apex. Predicted values along the wake centerline at different axial wake stations were obtained in this manner. Lateral values, although not found, could be obtained by placing the wedge at different lateral stations. Photographs were taken of the two-body configuration during each test run, and the appropriate measurements were obtained from these pictures. To do this, tangent lines to each wave were drawn in the vicinity of the wedge apex.

(b) Blunt-Body Method

The second approach involved a similar procedure except that a blunt body (analytical blunt body) was used in the wake in place of the slender wedge. With this method, the bow wave standoff distance from the blunt body (a 4-in. -diameter half cylinder with its flat face forward) was obtained from free-stream test results where the free-stream Froude number was known. This blunt body was placed at several axial wake stations to predict centerline values. Lateral values, although not obtained, could be found by placing the body at various lateral stations.

(c) Application of Stereo Camera/Projector^a

The third method involved the application of the stereo camera/projector facility available at Wright-Patterson Air Force Base. This approach is inherently more involved than either of the former methods and requires use of special photographic/projection equipment. The method is at least as accurate as the other two methods and offers the additional advantage of enabling the user to obtain complete radial profile from a single test.

In this method, the test subject and surrounding flow field are photographed simultaneously from two different locations. The processed images (formed on transparent glass slides) are then projected so that an analogic three-dimensional stereo model is created. Water depth contour maps are then constructed from these stereo models, permitting the application of the hydraulic analogy and other mathematical relationships. To facilitate the use of this method, a blunt body (a 4-in. half cylinder with its flat face forward) was placed in the trailing wake of the test body. The change in water level across the half cylinder's standoff bow wave then is related to the Froude number immediately forward of the wave.

As predictions by this method are based on a change in water level, it is instructive to present the theoretical mathematics involved. Babish⁴

^aA complete description of this equipment and its physical application is given in Volume II of this report.

provides the mathematical relations necessary to theoretically describe the physical changes.

Equations for normal hydraulic jump are as follows:

$$\frac{d_2}{d_1} = \left(2Fr_1^2 + \frac{1}{4} \right)^{\frac{1}{2}} - \frac{1}{2}. \quad (3)$$

$$\frac{d_{2o}}{d_1} = \left(\frac{d_2}{d_1} \right) + \frac{1}{4} \left[1 + \left(\frac{d_2}{d_1} \right)^{-1} \right]. \quad (4)$$

$$Fr_2^2 = \frac{1}{2} \left[\frac{1}{2} + \frac{1}{\left(\frac{d_2}{d_1} \right)} \right]^2 - \frac{1}{8}. \quad (5)$$

Equations for a slant hydraulic jump are as follows:

$$\frac{d_2}{d_1} = \left(2Fr_1^2 \sin^2 \theta + \frac{1}{4} \right)^{\frac{1}{2}} - \frac{1}{2}. \quad (6)$$

$$\frac{d_{2o}}{d_1} = \frac{\left[4 \left(\frac{d_2}{d_1} \right) + 1 + \frac{1}{\left(\frac{d_2}{d_1} \right)} \right] \left\{ 1 + \frac{1}{4 \sin^2 \theta} \left[\left(\frac{d_2}{d_1} \right)^2 + \frac{d_2}{d_1} \right] \right\}}{\left(\frac{d_2}{d_1} \right)^2 + \left(\frac{d_2}{d_1} \right) + 4}. \quad (7)$$

$$Fr_2^2 \sin^2 (\theta - \delta) = \frac{1}{2} \left[\frac{1}{2} + \frac{1}{\left(\frac{d_2}{d_1} \right)} \right]^2 - \frac{1}{8}, \quad (8)$$

where

$$\delta = \tan^{-1} \left\{ \frac{\tan \theta \left[\left(1 + 8Fr_1^2 \sin^2 \theta \right)^{\frac{1}{2}} - 3 \right]}{\left(2 \tan^2 \theta - 1 \right) + \left(1 + 8Fr_1^2 \sin^2 \theta \right)^{\frac{1}{2}}} \right\}. \quad (9)$$

Equations (3) through (8) provide the relationship between the total-to-static depth ratio and the static depth ratio as well as the relationship between the Froude number and the static depth ratio because the water in front of the body (in particular, along the centerline) is stagnated. This is of concern here because the hydraulic jump is not a near discontinuity as is its counterpart, the shock wave, in a gas. Consequently, the static water height immediately behind the wave but in front of the blunt body was not detectable as the water level continued to rise until it came to rest near the body. For this reason, it is necessary to have relationships available which include a total depth value behind the bow wave.

With these relationships, wake Froude number profiles were determined by the following procedure:

1. With the use of stereo contour maps, the ratio $(d_{t,2}/d_1)$ along the centerline was calculated and the corresponding (x/D) value immediately forward of the bow wave was determined. (Note: the bow wave is normal across the centerline and $y/D = 0$)
2. With the use of Equation 4, the centerline value of (d_2/d_1) and d_2 was calculated.
3. A line that contains the centerline value of d_2 was constructed parallel to the bow wave. This line is, approximately, the locus of the static depth values behind the shock for the applicable lateral range
4. Static depth ratios (d_2/d_1) were calculated and, with equation (3) or (6), the local Froude number value in front of the wave was determined. Corresponding values of (x/D) and (y/D) then were recorded.

In Procedure 3, above, the distance between the front of the hydraulic jump and the constructed parallel essentially defines the "effective thickness" of the wave. As was mentioned earlier, it is not a near discontinuity as is the shock wave in a gas. The effective thickness appears to increase (i. e., the bow wave "flattens out") with increasing lateral displacement from the trailing body. For these tests, however, the trailing blunt body (reversed half cylinder) more than spanned the viscous region of the wake and generated a bow shock that was nearly normal to the axial flow for a considerable distance into the inviscid wake.

Because this flow region generally encompassed the area of interest, the assumption made is considered a good approximation. This condition imposes no inherent restrictions on tow channel testing in general because a comparatively large trailing body presumably could always be used.

In Item 4, no stream tube deflection was considered. This can be justified by the near-normal wave shape in the region of interest indicating

that deflections would be small. Also, the desired local Froude number values are not known beforehand. Hence, the tracing of streamlines through the wave could be done only with some difficulty; possibly through an iterative procedure whereby successive approximations of the desired Froude number are obtained.

(2) Local Wake Froude Number Results

Results obtained using the three previously described methods are presented and discussed below. As previously indicated, the first two methods involve simple geometric comparisons while the latter method uses mathematical relationships theoretically applicable to a water flow.

In Figure 10 data are presented that indicate the results obtained using the slender wedge method. One aspect of these data which is readily apparent is that the local data trends are irregular and inconsistent while general trends, where they seem to exist, are contrary to what would be expected. One possible explanation is the difficulty encountered in making accurate measurements of the wave angle in the vicinity of the wedge apex. Measurements were taken from conventional two-dimensional photographs. From these photographs, the existence of the nonuniform wake stream forward of the slender wedge was indicated by the curvature of the attached bow wave produced by the wedge. The degree of curvature compounded the difficulty of making accurate measurements near the wedge apex. Also, secondary effects on local wave angles may be produced by the adjacent conditions. In nearly all cases, however, it can be observed that a Froude number defect was correctly indicated.

Results obtained using the blunt body method are presented in Figure 11 for three different configurations. In these data, little or no Froude number defect in the wake is indicated. These results tend to indicate that bow wave standoff distance (although not necessarily the wave shape itself) is a poor indicator of wake conditions. The reasons for this are not clear although lack of accurate representative measurements may pose part of the problem. Wave oscillations resulting from small fluctuations in the velocity of the test configuration, for example, are a definite possibility.

Results obtained with the stereo camera/projector equipment for three representative forebody configurations are presented in Table I. It can be seen from the table that the profiles obtained are not purely lateral. This results from following the contour of the trailing hydraulic jump to obtain the local upstream Froude number values.

In Figure 12, lateral Froude number profiles are plotted for the configurations of Table I. These data were obtained by extrapolating between the profiles indicated in Table I. Results of Figure 12 appear to be at least qualitatively indicative of compressible gas wake. The nondimensional Froude number values at the centerline appear to be reasonable, although the order in which they occur with respect to the axial wake station is somewhat inconsistent. Those portions of the curves that are above the

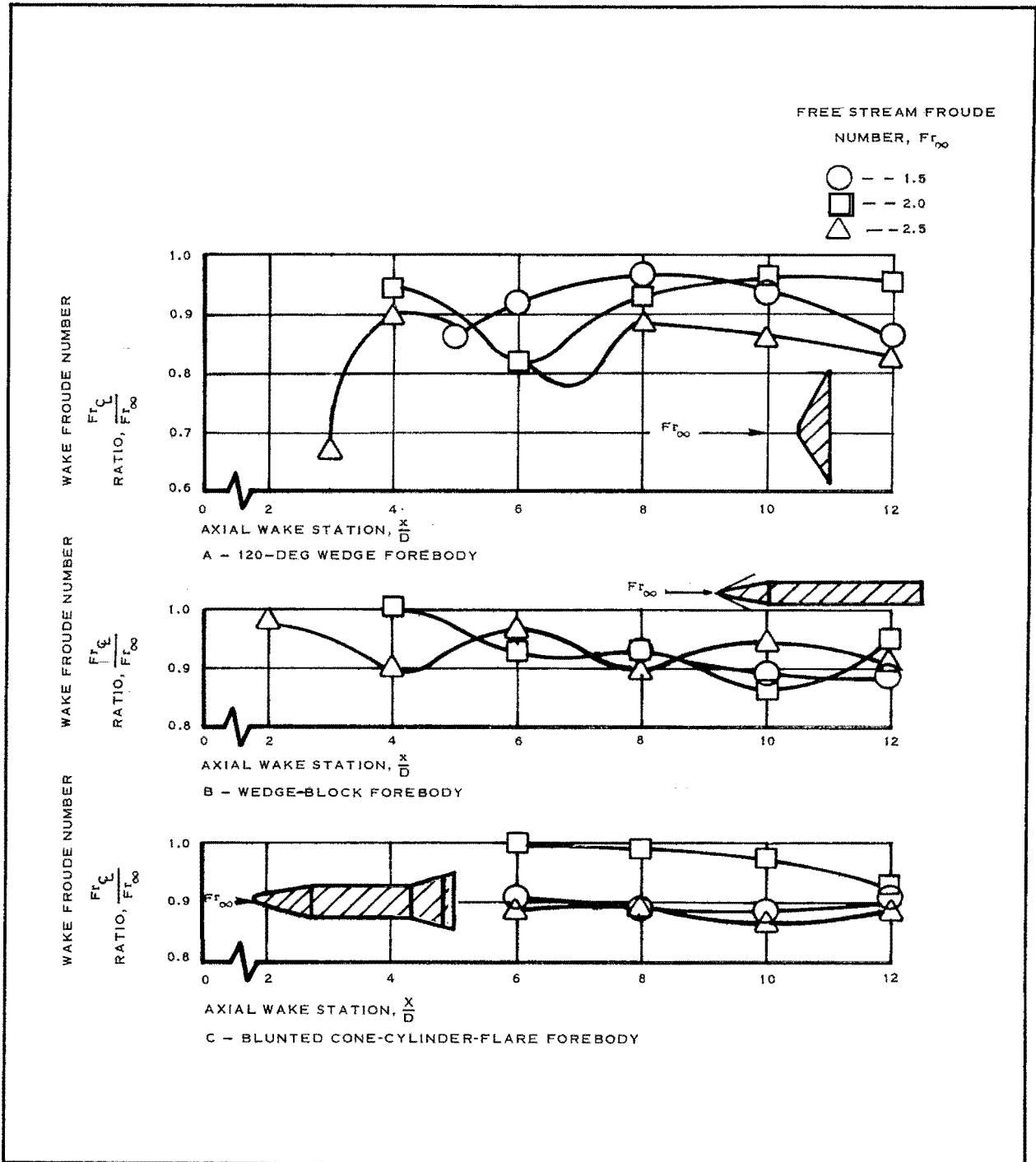
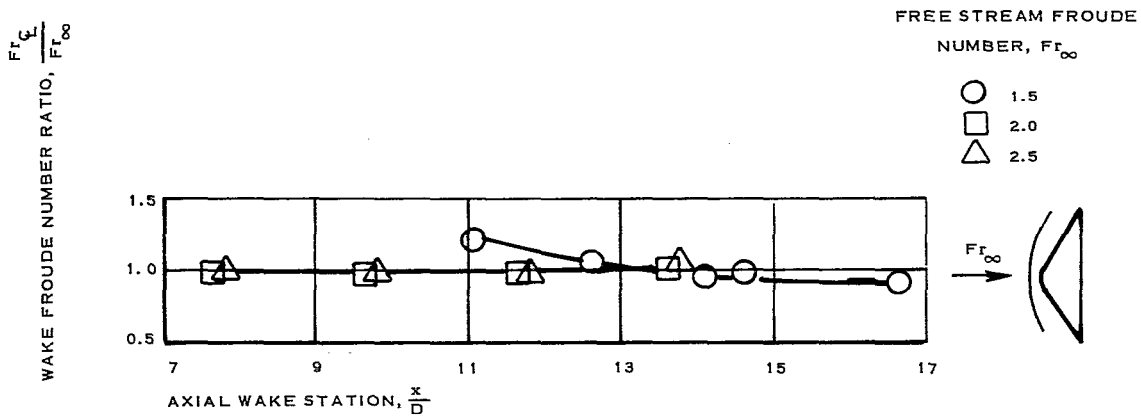
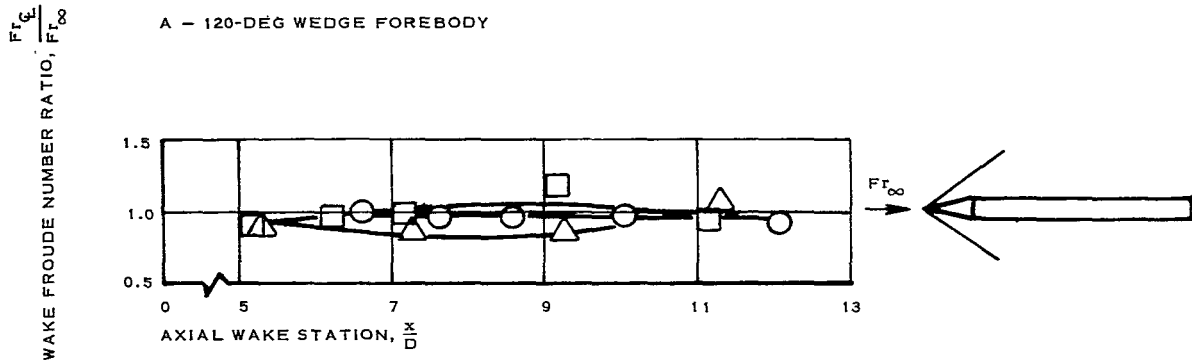


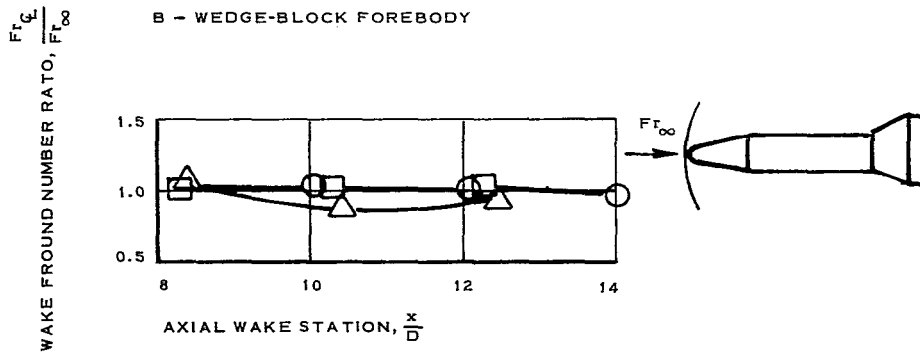
Figure 10 - Tow Channel Froude Number Results along Wake Centerline:
Slender Wedge Method



A - 120-DEG WEDGE FOREBODY



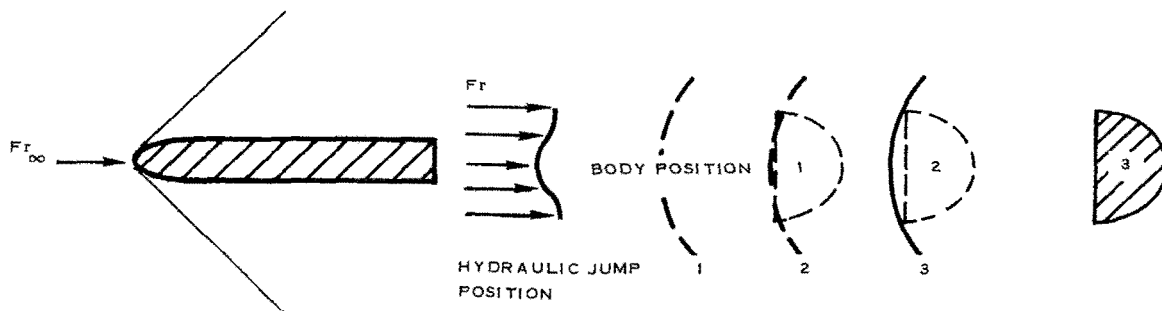
B - WEDGE-BLOCK FOREBODY



C - BLUNTED WEDGE-BLOCK-FLARE FOREBODY

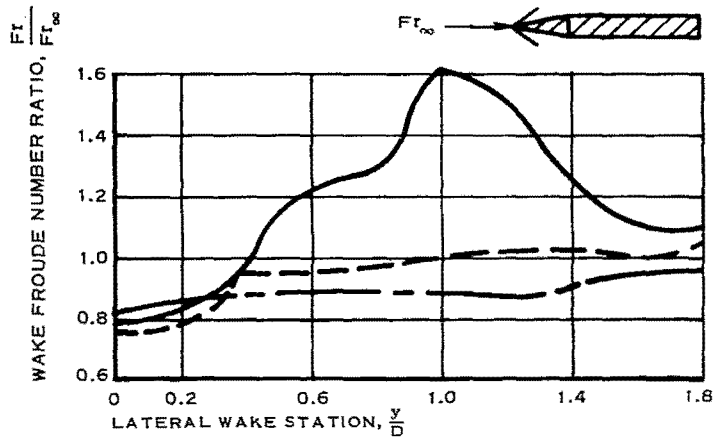
Figure 11 - Tow Channel Froude Number Results along Wake Centerline:
Blunt Body Method

TABLE I - HYDRAULIC JUMP COORDINATES AND
 LOCAL FROUDE NUMBER VALUES
 (STEREO CAMERA/PROJECTOR METHOD)

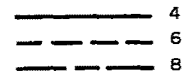


Hydraulic jump location	Wedge-block wake data			120-deg-wedge wake data			Blunted wedge-block-flare wake data		
	$\frac{x}{D}$	$\frac{y}{D}$	$\frac{Fr}{Fr_{\infty}}$	$\frac{x}{D}$	$\frac{y}{D}$	$\frac{Fr}{Fr_{\infty}}$	$\frac{x}{D}$	$\frac{y}{D}$	$\frac{Fr}{Fr_{\infty}}$
1	3.40	0.000	0.850	3.98	0.000	0.720	4.95	0.000	0.764
	3.42	0.155	0.850	3.98	0.040	0.723	4.97	0.229	0.780
	3.54	0.304	1.000	4.07	0.265	0.784	5.06	0.486	0.480
	3.74	0.538	1.240	4.07	0.392	0.874	5.17	0.887	0.820
	3.89	0.925	1.720	4.05	0.490	1.390	5.20	1.057	0.860
	4.00	1.230	1.430	4.03	0.687	1.350	5.26	1.230	0.956
	4.24	1.610	1.190	4.03	0.842	1.200	5.34	1.515	1.060
2	5.54	0.000	0.772	5.90	0.000	0.840	6.75	0.000	0.810
	5.55	0.154	0.773	5.95	0.115	0.840	6.86	0.143	0.810
	5.63	0.462	0.850	6.02	0.688	0.855	7.12	0.628	0.890
	5.75	0.730	0.970	6.04	1.040	0.973	7.43	1.544	0.875
	5.95	1.120	1.040	6.07	1.200	1.315	7.55	1.915	0.910
	6.05	1.460	1.260	6.16	1.450	1.240	7.60	2.110	0.955
	6.05	1.840	1.120	6.30	1.760	1.090	7.66	2.480	1.070
3	7.75	0.000	0.795	7.75	0.000	0.850	11.14	0.000	0.825
	7.92	0.230	0.840	7.80	0.186	0.850	11.16	0.286	0.830
	8.10	0.770	0.880	7.80	0.431	0.855	11.20	0.686	0.845
	8.23	1.190	0.900	7.82	0.920	0.880	11.25	0.944	0.855
	8.38	1.770	0.922	7.85	1.080	0.910	11.37	1.370	0.875
	8.51	2.190	1.070	8.05	1.630	0.946	11.50	1.515	0.890
	8.55	2.620	1.020	8.04	1.710	1.210	11.78	2.165	0.910

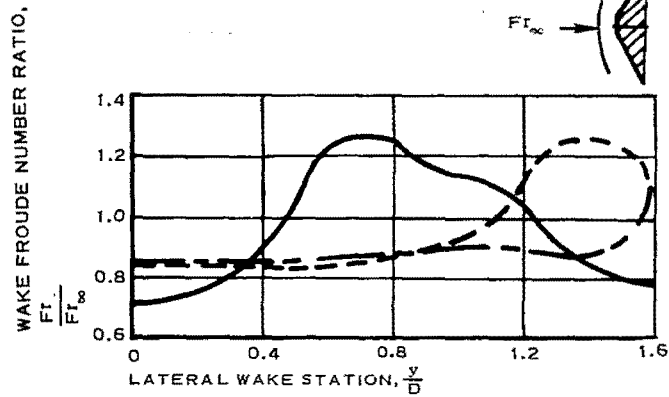
A - WEDGE-BLOCK FOREBODY



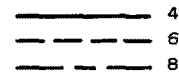
AXIAL WAKE STATION, $\frac{x}{D}$



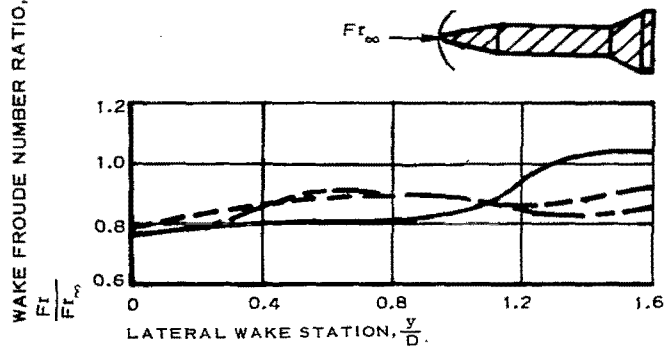
B - 120-DEG WEDGE FOREBODY



AXIAL WAKE STATION, $\frac{x}{D}$



C - BLUNTED WEDGE-BLOCK-FLARE FOREBODY



AXIAL WAKE STATION, $\frac{x}{D}$

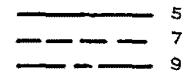


Figure 12 - Tow Channel Froude Number Wake Profiles Obtained with Stereo Camera/Projector

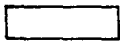
freestream Froude number value are representative of the gas case in the vicinity of the recompression shock where the flow expansion results in local Mach number values in excess of the free-stream values. As in a gas, the values reach some peak and then decline toward the free-stream value. In this regard, the order of the curves is entirely consistent and correct. Certain differences between these results and gas results do exist, however. These differences, along with comparative data, are discussed in Section IV.

c. Comparison of Theoretical and Experimental Results across a Near-Normal Hydraulic Jump

Of the methods for predicting local wake Froude number, the stereo camera/projector method seems the most promising although the validity of the method is dependent upon the accuracy of both the equations used and the assumptions made. To indicate the validity of this method, the following results obtained from known upstream conditions are presented. These results are also used in Section IV for correlation of water and gas results.

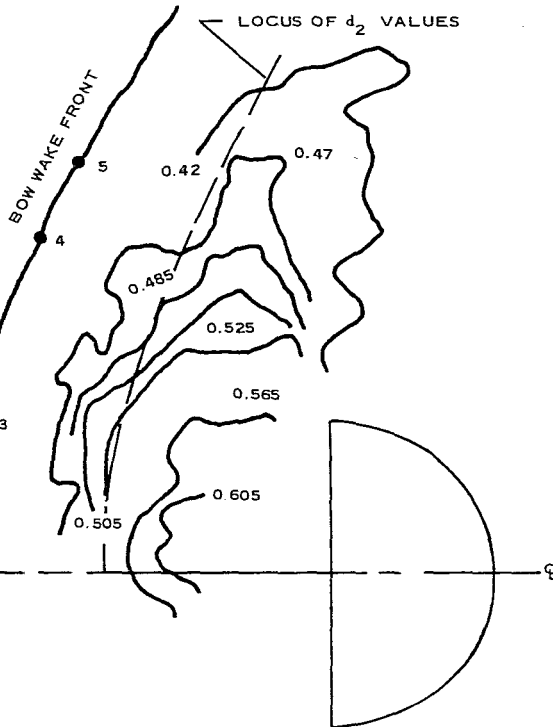
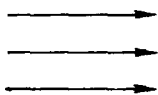
During the program, tests were conducted with an analytical blunt body (reversed half cylinder) located in a uniform freestream flow, i. e., without a leading body. Stereo photographs of these tests were taken and the data subsequently were reduced to water-depth contour maps. A typical map is schematically shown in Figure 13 where it is apparent that both the free-stream depth and Froude number are known parameters. The static depth ratio, determined as previously described, is used to predict the free-stream Froude number. These results then can be compared with the actual values. Typical comparative results are tabulated at the bottom of Figure 13 where the predicted values were determined using Equation (6). Extremely good agreement is seen to exist, well within both the tolerances on the actual free-stream Froude number and the accuracy of the depth values used. These results tend to support the validity of the theoretical equations previously presented and add credence to their application for wake profiles.

REFERENCE GAGE BLOCK = 0.5 IN.



FREE STREAM DEPTH = 0.2 IN.

$Fr_{\infty} = 2.2$



POINT	θ (DEG)	d_2 (IN.)	d_2/d_1	Fr_{∞} (PREDICTED)	Fr_{∞} (ACTUAL)	PERCENT ERROR
1	90	0.536	2.68	2.22	2.2	0.91
2	83	0.536	2.68	2.24	2.2	1.82
3	77	0.525	2.63	2.24	2.2	1.82
4	65	0.450	2.25	2.15	2.2	2.25
5	61	0.460	2.30	2.23	2.2	1.36

Figure 13 - Prediction of Upstream Froude Number Values with Water Depth Contour Maps



SECTION III - THEORETICAL WAKE ANALYSIS AND DEVELOPMENT

1. ACCOMPLISHMENTS

The initial development of a method for carrying out wake calculations for axisymmetric bodies is presented in Reference 5. In the present program, these equations were extended to include wake calculations for two-dimensional bodies and combined with the previous results to form a general set of unified equations. In addition, the modifications required to provide the capability of calculating wake profiles for two-dimensional and axisymmetric bodies in subsonic and incompressible ($M = 0$) flow regimes were established. Hence, the present method of solution is suitable for flow environments ranging in Mach number from zero to hypersonic (not including temperature effects of dissociation and ionization). Finally, wake calculations can be made for any gas which can be represented by an effective specific heat ratio and gas constant and for which a Prandtl number of one is a reasonable assumption.

2. SUMMARY OF BOUNDARY LAYER AND FOREBODY FLOW FIELD CALCULATION PROCEDURE

One necessary prerequisite to any wake analysis is the development of suitable boundary-layer and forebody-flow-field equations. The detailed mathematical development of these equations, from Reference 5, is given in Appendixes A and B. In general, laminar boundary layer calculations are carried out with the use of local similarity solutions by Kemp, Rose and Detra⁶ for compressible flow. An approximate turbulent boundary layer solution is obtained using the methods of Reshotko and Tucker.⁷ Forebody pressure distributions are predicted, when necessary, using tangent wedge, tangent cone, or Newtonian flow theory.

3. TWO-DIMENSIONAL VISCOUS WAKE ANALYSIS

a. Formulation of the Viscous Wake Problem

Any calculation of the properties of the high-speed wake must include both the viscous and inviscid wake regions. The former may be either laminar or turbulent in nature and is an extension of the boundary layer of the body into its downstream region. The properties of the inviscid wake, on the other hand, are primarily influenced by the presence of shock waves in the flow field of the body, *i. e.*, the bow shock wave or various embedded shock waves. Thus, any variation in the properties of a wake from those of the free stream are due to the presence of non-isentropic phenomena in the flow field.

An integral method is applied to the problem of determining properties of both laminar and turbulent viscous wakes. Important assumptions contained in the theory are:

1. The fluid is thermally and calorically perfect and there are no chemical reactions or other real-gas phenomena.
2. Both the molecular and turbulent Prandtl numbers are unity ($Pr = 1$).
3. Prandtl's concept of viscous flow phenomena is valid for the high speed compressible wake so that gradients in the streamwise or axial direction are much smaller than those normal to the wake axis; thus, boundary layer equations may be used.
4. Details of the base flow and free shear layer regions may be largely ignored. Thus the region of validity for the present analysis must be considered to extend from somewhere in the vicinity of the wake neck or further downstream and on down into the far wake.
5. Effects due to the existence of an external pressure gradient are negligible.

Use of such assumptions simplifies the method presented in this report. They are justified on the basis that they permit the development of a solution which, to a first approximation, provides good results (see Reference 5 and Section IV of this document). Basic governing differential equations for two-dimensional flow, in accordance with Assumption 3, above, are:

1. Continuity -

$$\frac{\partial}{\partial r}(\rho v) + \frac{\partial}{\partial x}(\rho u) = 0. \quad (10)$$

2. Momentum -

$$\rho u \frac{\partial u}{\partial x} + \rho v \frac{\partial u}{\partial r} = \frac{\partial}{\partial r} \left(\mu \frac{\partial u}{\partial r} \right). \quad (11)$$

3. Energy -

$$\rho u \frac{\partial h}{\partial x} + \rho v \frac{\partial h}{\partial r} = \frac{\partial}{\partial r} \left(\frac{k}{c_p} \frac{\partial h}{\partial r} \right) + \mu \left(\frac{\partial u}{\partial r} \right)^2. \quad (12)$$

The coordinate system in which these equations are written is shown in Figure 14. For laminar flow the properties in the above equations are the conventional local properties, while for turbulent flow u , v , p , and ρ must be interpreted as time-averaged quantities (as opposed to the fluctuating component of each of these properties). Viscosity, μ , takes a different form for laminar flow than for turbulent flow as will be discussed later.

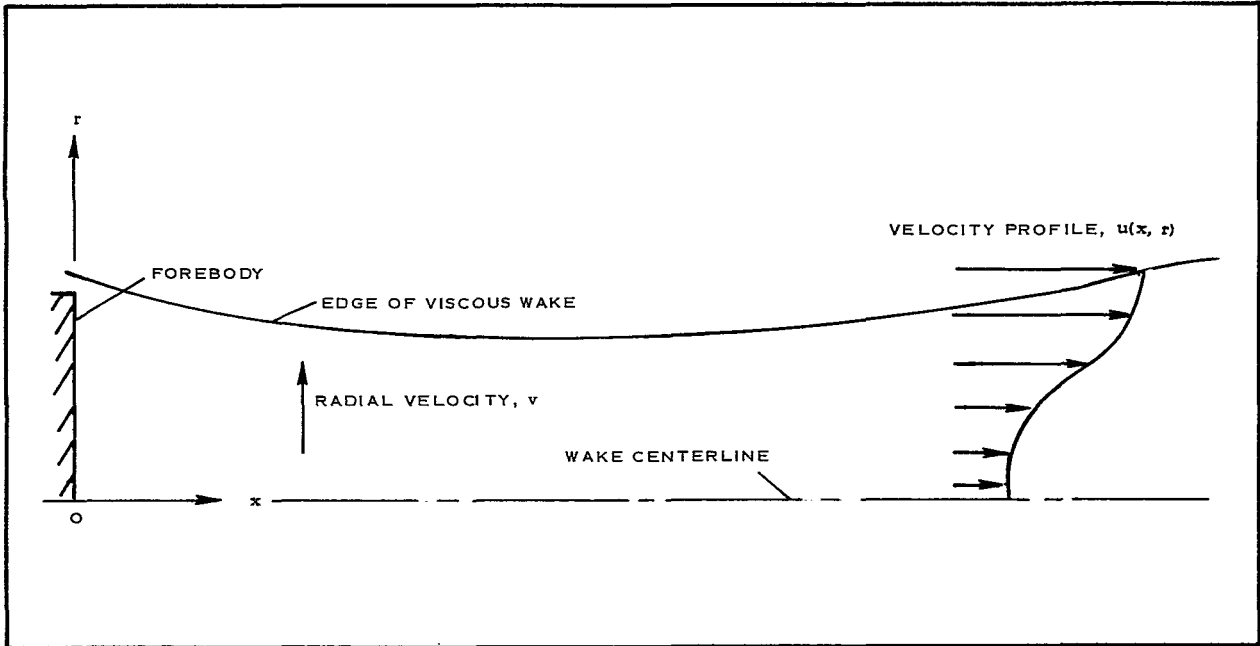


Figure 14 - Viscous Wake Coordinate System

The solutions of Equations (10) through (12) as applied to a wake will take a dissimilar form, *i. e.*, they will not reduce to ordinary differential equations using a conventional boundary layer transformation. The only suitable methods of solution would be numerical ones using various finite-difference schemes. Such solutions are time-consuming; therefore, it is of interest to consider the application of the Karman-Pohlhausen integral method. Such a general method has been applied previously to axisymmetric wakes and will be used here in the analysis of the two-dimensional case.

In such an integral method, the governing equations are the integrated forms of the axial momentum and energy equations. As applied to a wake and using Assumption 5, these equations, in differential form, are:

$$\frac{d}{dx}(\rho_1 u_1^2 \theta_1) = 0 \quad (13)$$

and

$$\frac{d}{dx}(\rho_1 u_1 H_1 \theta_{T_1}) = 0, \quad (14)$$

where

$$\rho_1 u_1^2 \theta_1 = \int_0^\delta \rho u (u_1 - u) dr \quad (15)$$

and

$$\rho_1 u_1 H_1 \theta_{T_1} = \int_0^\delta \rho u (H_1 - H) dr \quad (16)$$

These represent the momentum and energy defects respectively; using Assumption 5, both may be shown to be constant with respect to x . For example, because the pressure gradient has been assumed to be negligible, there is no external work being done on the wake and the momentum and energy defects must be constant. Thus, as the trailing wake grows, its momentum and energy defects are spread out over an increasingly larger area due to the viscous and thermal conduction transport phenomena and remain unchanged.

In Equations (13) through (16) above, θ_1 is the momentum thickness and θ_{T_1} is the total enthalpy thickness.

By ignoring the details of the base flow and shear layer regions and assuming that no external work is done on the wake fluid in these regions, then the wake momentum defect may be evaluated by equating it to the momentum defect of the boundary layer at the base of the forebody. This may be stated mathematically as

$$\rho_B u_B^2 \theta_B = \rho_1 u_1^2 \theta_1, \quad (17)$$

where the subscript "1" refers to properties associated with the outer edge of the wake, and the subscript "B" to properties at the base of the vehicle where the boundary layer separates. ρ_B and u_B are inviscid properties, while D is the forebody base diameter for the axisymmetric case.

The energy defect may be directly related to the momentum defect for $Pr = 1$ and thus it takes a form similar to that of Equation (17). It is these two related defects of energy and momentum that tie the wake to the forebody boundary layer. To carry out quantitative calculations, the forebody boundary layer characteristics must first be calculated. Of particular importance is the boundary layer momentum defect and the calculation of this quantity for the case of an arbitrary pressure-gradient and a laminar or turbulent flow (including transition).

With the momentum and energy integral equations available, as well as a means for relating the corresponding defects to the forebody boundary layer, the wake profiles are then determined using assumed polynomial forms in which coefficients are determined from suitable boundary

conditions. Such a general analysis will be carried out in the next part of this section for two-dimensional laminar and turbulent flows.

b. General Solution of the Viscous Wake Problem

In carrying out a momentum integral method of solution for two-dimensional laminar and turbulent viscous wake flow, it is the momentum integral equation, in the form of Equation (17), that will be of most interest. This is the equation which the final solution must satisfy. The governing differential equations primarily provide a means for obtaining additional boundary conditions to be imposed on the solution. The solution obtained will not satisfy the normal continuity, momentum, and energy equations exactly; it is only the mean properties of the flow that are obtained. On the other hand, the sacrifice in exactness is in many cases more than compensated for by the resulting simplifications in the method of calculation.

To obtain a solution for the wake velocity profile, a transformed coordinate system is introduced where for the two-dimensional case

$$dn = \frac{\rho}{\rho_1} dr. \tag{18}$$

This is generally called a Dorodnitsyn transformation; and in this new x, n coordinate system, the wake thickness Δ is found through integration to be

$$\Delta = \int_0^{\delta} \frac{\rho}{\rho_1} dr. \tag{19}$$

where δ is the actual wake thickness or radius in physical coordinates.

A nondimensional variable,

$$\eta = \frac{n}{\Delta}, \tag{20}$$

then may be introduced so that $\eta = 0$ at the center of the wake and $\eta = 1$ at the outer edge where $y = \delta$. In this x, η coordinate system it is assumed that the velocity profile may be expressed as

$$\frac{u}{u_1} = \sum_{i=0}^4 a_i \eta^i. \tag{21}$$

Here, u_1 is the velocity at the edge of the viscous wake and the a_i 's are coefficients in the fourth-order polynomial which are functions only of x and not of η . These coefficients are determined from the following boundary conditions.

At the centerline of the wake, where $r = \eta = 0$:

1. The velocity gradient is zero, i. e., $\partial u / \partial r = \partial u / \partial \eta = 0$.
2. X-direction momentum equation must be satisfied.

At the outer edge of the wake, where $r = \delta$ and $\eta = 1$:

1. Velocity is equal to that from inviscid flow, i. e., $u = u_1$.
2. Velocity gradient is zero, i. e., $\partial u / \partial r = \partial u / \partial \eta = 0$.
3. Second derivative of the velocity is zero, i. e., $\partial^2 u / \partial r^2 = \partial^2 u / \partial \eta^2 = 0$.

Applying these boundary conditions, one can force the resulting form for the two-dimensional velocity profile to be identical to that for axisymmetric flow, i. e.,

$$\frac{u}{u_1} = (6\eta^2 - 8\eta^3 + 3\eta^4 - 1) \frac{\xi}{24} + 1 \quad (22)$$

by defining ξ , the form factor, to be

$$\xi = 2 \frac{\rho_1}{\rho_0} \frac{u_0}{u_1} \Delta^2 \frac{\rho_1}{\mu_0} \frac{du_0}{dx} \quad (23)$$

Here the subscript, o, refers to wake centerline conditions. ξ is similar to the pressure gradient parameter in the Karman-Pohlhausen solution for two-dimensional boundary layers.⁸ The wake centerline velocity is related to ξ through the equation

$$\frac{\xi}{24} = 1 - \frac{u_0}{u_1} \quad (24)$$

At the rear stagnation-point, $\xi = 24$ and $u_0 = 0$; while at $x = \infty$, $u_0 = u_1$ and $\xi = 0$.

It is necessary to also consider the relationship between θ_1 , the wake momentum thickness, and Δ . This is obtained from Equation (15); and upon transformation, substitution, and integration results in

$$\frac{\theta_1}{\Delta} = \frac{\xi}{60} - \frac{\xi^2}{2016} \quad (25)$$

for two-dimensional flow.

Using Equation (23), the general relation for ξ as a function of x now may be obtained through integration. However, in doing this, a form for the centerline viscosity, μ_o , must be specified, as well as the centerline density, ρ_o . The former will depend on whether the flow is laminar or turbulent and the type of viscosity model chosen. The latter, on the other hand, is obtained from the solution of the energy equation.

Using the energy equation and the solution for the wake enthalpy profile, it may be shown that for the case of $Pr = 1$ and for a zero pressure gradient this solution gives a particularly simple form in which the total enthalpy H is given by Crocco's equation as

$$H = C_1 u + C_2. \quad (26)$$

Here the constants C_1 and C_2 may be re-expressed using the conditions that when $u = u_o$, $H = H_o$, and $u = u_1$, $H = H_1$. The resulting equation for H then has the form

$$\frac{H_1 - H}{H_1 - H_o} = \frac{1 - \frac{u}{u_1}}{1 - \frac{u_o}{u_1}}. \quad (27)$$

Although H_1 is known from the inviscid flow conditions at the outer edge of the wake, H_o is not known and must be determined from application of the energy integral equation, Equation (14). Transforming this equation, substituting, and comparing with the momentum integral equation, it may be shown that

$$\frac{H_o}{H_1} = 1 - \left(\frac{\theta_{T1}}{\theta_1} \right) \left(1 - \frac{u_o}{u_1} \right), \quad (28)$$

where

$$\frac{\theta_{T1}}{\theta_1} = \left(1 - \frac{h_w}{H_1} \right) \frac{u_1}{u_B}. \quad (29)$$

Here θ_{T1} is the total enthalpy thickness, h_w is the gas enthalpy based on the temperature of the body, and u_B is the velocity at the base of the body where the boundary layer separates. Equation (29) results from matching the forebody boundary layer and viscous wake defects.

Knowing the total enthalpy profile, the static enthalpy may be obtained from the relation

$$h = H - \frac{u^2}{2}, \quad (30)$$

and the gas density from the equation of state

$$\rho = \frac{\gamma}{\gamma - 1} \frac{P}{h}. \quad (31)$$

Thus, to complete the viscous wake solution, only two tasks still remain. One of these is to determine the relationship between r and η . This may be done using Equation (18) and integrating. The result is

$$\begin{aligned} \frac{r}{\Delta} = & \frac{H_1}{h_1} \eta + \left(\frac{\theta_{T_1}}{\theta_1} \right) \frac{H_1}{h_1} \frac{\xi}{24} \left(2\eta^3 - 2\eta^4 + \frac{3}{5}\eta^5 - \eta \right) - \\ & \frac{(\gamma - 1)M_1^2}{2} \left[\eta + \frac{\xi}{12} \left(2\eta^3 - 2\eta^4 + \frac{3}{5}\eta^5 - \eta \right) + \frac{\xi^2}{576} \left(\eta - 4\eta^3 + 4\eta^4 + 6\eta^5 - \right. \right. \\ & \left. \left. 16\eta^6 + \frac{100}{7}\eta^7 - 6\eta^8 + \eta^9 \right) \right]. \quad (32) \end{aligned}$$

The wake displacement thickness can now be readily calculated as

$$\delta^* = \Delta \left[\frac{H_1}{h_1} - \frac{\xi}{60} \frac{H_1}{h_1} \frac{\theta_{T_1}}{\theta_1} - \left(\frac{\gamma - 1}{2} \right) M_1^2 - \left(1 - \frac{\xi}{30} + \frac{\xi^2}{2016} \right) - 1 + \frac{\xi}{60} \right] \quad (33)$$

The second task is to determine the relationship between ξ and x . This will be done using Equation (23) and is discussed in Item 3, c, below for three separate cases. Once this relationship is known, then for a given x and wake outer edge conditions, ξ can be determined, the wake thickness can be determined from Equation (25), the velocity profile can be determined as a function of η from Equation (22), and the enthalpy profile can be determined from Equations (28) through (30). These may then be transformed into physical coordinates using Equation (32) to complete the solution.

c. Complete Viscous Wake Solutions for Special Cases

(1) General

Consideration of the relationship between ξ and x for the following three special viscous wake cases or models completes the analysis in Item 3, b, above:

1. Conventional laminar wake

2. Two-dimensional laminar "cylindrical" wake
3. Conventional turbulent wake

The second wake model constitutes a special laminar wake case for axisymmetric flow. It arises from consideration of the wake problem when a thin tow cable or riser line is assumed to connect a decelerator with the forebody, and, thus, imposes a no-slip condition along the wake centerline. Such a consideration, therefore, is appropriate here.

The concept of a laminar "cylindrical" wake model for axisymmetric flow is considered well-founded,^{5,9} and as applied here refers only to the logical extension of that case. Such a model is conceptually valid (although possibly not realistic) for two-dimensional flow and alters the results accordingly. In this discussion, the word "cylindrical" is used to denote the extension from the axisymmetric case, and should be interpreted as meaning a two-dimensional laminar wake of constant thickness unless otherwise indicated.

For the turbulent wake model no such special counterpart apparently exists even in the axisymmetric case. It is hypothesized that the no-slip condition, when a riser line is present, is satisfied by the thin laminar sublayer existing at its surface. Consequently, the viscous turbulent wake profiles may be calculated using the mathematical formulation for a conventional turbulent wake.

(2) Conventional Laminar Wake

As was indicated previously, in order to evaluate Equation (23) and obtain ξ as a function of x , it is necessary to specify a relation for the viscosity coefficient. For laminar flow, the viscosity may be assumed to have a linear dependence on the fluid temperature, *i. e.*, $\mu/R_1 T = \text{constant}$. Since in this analysis the radial pressure gradient is assumed to be zero, then from the equation of state it may be shown that $\rho\mu$ is constant with respect to r and that $\rho\mu = \rho_1\mu_1$. Equation (23) may then be written as

$$\xi = 2 \frac{u_o}{u_1} \Delta^2 \frac{\rho_1}{\mu_1} \frac{du_o}{dx}. \quad (34)$$

Because

$$\frac{u_o}{u_1} = 1 - \frac{\xi}{24},$$

then

$$\frac{du_o}{dx} = - \frac{u_1}{24} \frac{d\xi}{dx}.$$

Furthermore, the relationship between Δ and ξ is known from Equation (25). Substituting these results into Equation (34) yields the following results:

$$\left(\frac{\theta}{\Delta}\right)^2 \xi = -2 \left(1 - \frac{\xi}{24}\right) \theta^2 \frac{\rho_1}{\mu_1} \frac{u_1}{24} \frac{d\xi}{dx}, \quad (35)$$

where θ/Δ is given by Equation (25). Because ρ_o has not been specified in terms of ξ or x , these variables are not yet uniquely related to each other. This is accomplished by first using the equation of state,

$$\begin{aligned} \rho_o &= \frac{p_1}{R_1 T_o} \\ &= \frac{\gamma}{\gamma - 1} \frac{p_1}{h_o}, \end{aligned}$$

then substituting for the static enthalpy from Equation (30). With the use of Equation (28), ρ_o then may be expressed as

$$\rho_o = \frac{\gamma}{\gamma - 1} \frac{p_1}{H_1 - \left(\frac{\theta}{\theta_1}\right) H_1 \left(1 - \frac{u_o}{u_1}\right) - \frac{u_o}{2}}. \quad (36)$$

Because the relationship between u_o/u_1 and ξ is known, Equation (35), upon rearranging, may be put in the form

$$\begin{aligned} \frac{x}{\theta} \left(\frac{1}{Re_\theta}\right) &= \frac{Re_x}{Re_\theta^2} \\ &= - \int_{24}^{\xi} \frac{1 - \frac{\xi}{24}}{12 \frac{\theta^2}{\Delta}} \frac{d\xi}{\xi}, \end{aligned} \quad (37)$$

where θ/Δ is taken from Equation (25). Here x is measured from the point where the wake centerline velocity physically is zero, i. e., the rear stagnation point. For known flow conditions, the above equation gives the variation of ξ with x . This is shown in Figure 15 for the two-dimensional case. Using Figure 15 and the results of Item 3, b, above a complete solution for the wake flow then may be obtained.

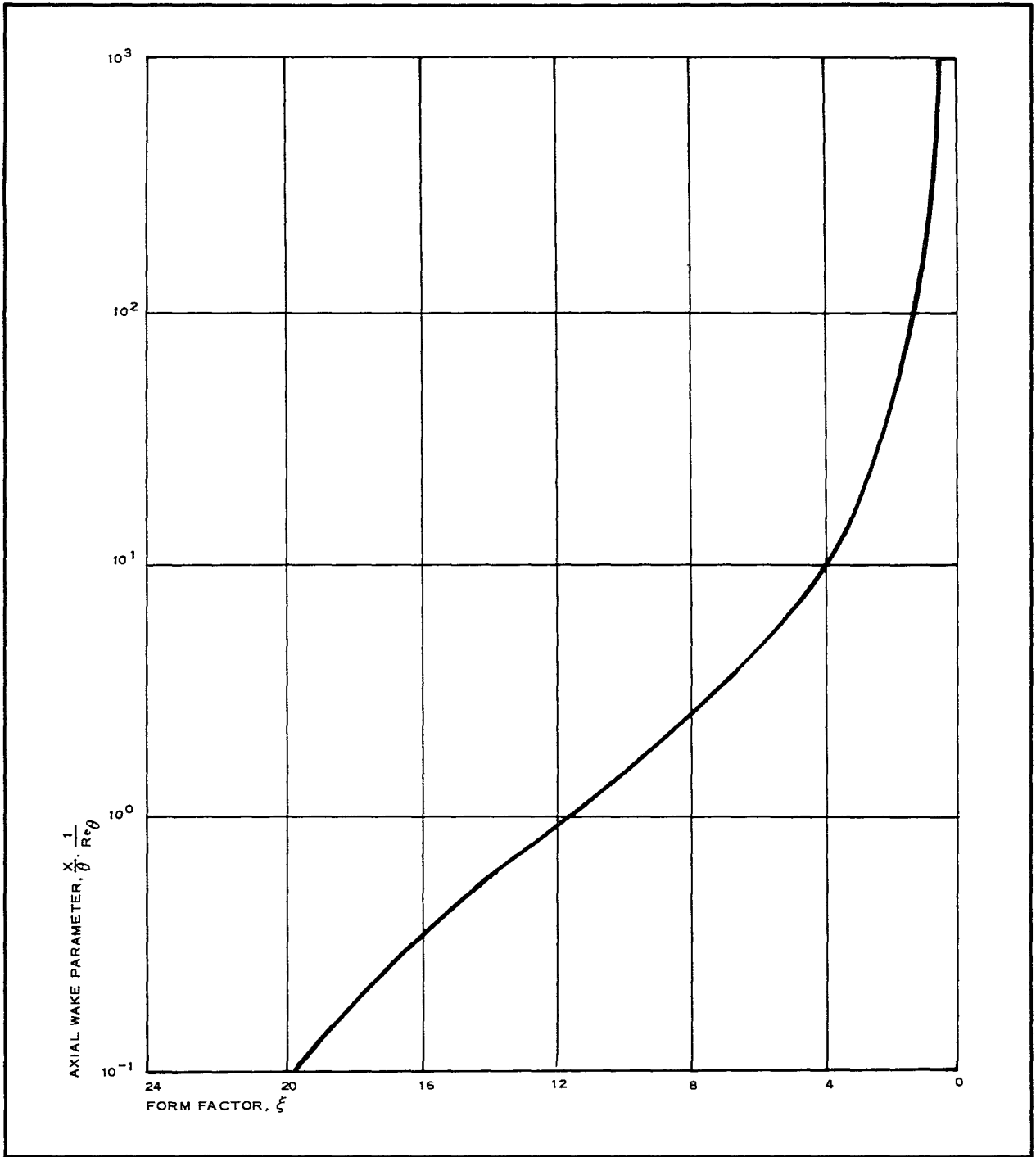


Figure 15 - Laminar Wake Shape Factor as a Function of Form Factor for Two-Dimensional Compressible Wake

(3) Cylindrical Laminar Wake

An approximate solution corresponding to this special case may be obtained from the previous results by noting that u_0/u_1 equal to zero is equivalent to ξ equal to 24. Thus, the properties of a cylindrical wake may be obtained by setting ξ equal to 24 in the previously derived equations. Form factor, ξ , will not depend on x for this simplified case because there will be complete similarity between the transverse profiles at all axial wake stations.

For this case, the wake velocity profile then is given by

$$\frac{u}{u_1} = 6\eta^2 - 8\eta^3 + 3\eta^4; \quad (38)$$

and the transformed wake thickness, by

$$\frac{\Delta}{\theta} = 8.75, \quad (39)$$

where θ_1 is determined from equating the wake momentum defect to the momentum defect of the forebody boundary layer, as mentioned previously. For a slender body with a zero axial pressure gradient in the wake region, θ_1 is constant and thus Δ is also a constant. The wake thus has a constant thickness.

For such a wake, the solution to the energy equation ($Pr = 1$) is similar to that given in Item 3, b, above, and may be written as

$$\frac{H}{H_1} = 1 - \frac{h_w}{H_1} \frac{u}{u_1} + \frac{h_w}{H_1}, \quad (40)$$

where h_w is the enthalpy of the gas at a temperature equal to that of the tow cable or riser line. With the velocity and enthalpy profiles known, the wake characteristics can be completely determined. The transformed and physical coordinates then can be related using Equation (32) for $\xi = 24$ with the result that

$$\begin{aligned} \frac{r}{\Delta} = & \frac{H_1}{h_1} \eta + \frac{H_1}{h_1} \left(1 - \frac{h_w}{H_1} \right) \left(2\eta^3 - 2\eta^4 + \right. \\ & \left. \frac{3}{5}\eta^5 - \eta \right) - \frac{(\gamma - 1)}{2} M_1^2 \left(\frac{36}{5}\eta^5 - 16\eta^6 + \right. \\ & \left. \frac{100}{7}\eta^7 - 6\eta^8 + \eta^9 \right). \end{aligned} \quad (41)$$

When the above equation is applied at $\eta = 1$, the actual wake radius or thickness can be related to the transformed thickness; i. e.,

$$\frac{\delta}{\Delta} = - 0.09 + (0.69) \frac{H_1}{h_1} + (0.40) \frac{h_w}{h_1}. \quad (42)$$

With Equations (38) through (42), the solution is complete with the properties being clearly specified in terms of the forebody boundary layer characteristics and the inviscid properties at the edge of the viscous wake. It should be noted that in this solution the variation in properties with x is controlled by the change in the inviscid flow field with x since the solution is effectively a constant ξ solution and there is no meaningful relationship between ξ and x (except for the statement that ξ is constant).

As previously mentioned, the applicability of this model to the axisymmetric wake is well founded and the concept of a cylindrical wake is supported both from the viewpoint of theory (e. g., in the limit of a riser line or tow cable of infinitesimal diameter) as well as by limited experiments (References 5 and 9). For the two-dimensional case, however, the basic argument no longer holds. Now the tow cable is a plane lying along the axis of the two-dimensional viscous wake; and even if this plane is infinitesimal in thickness, there will still be skin friction work done on the wake and the viscous wake will in fact just be an extension of the boundary layer on the body. On the other hand, if there is no tow cable and thus no corresponding plane on the wake axis, then the viscous wake will just be a conventional wake. This is true even if a decelerator is placed in this wake as long as there is a sufficient separation between the forebody and decelerator so that the wake is not "blown."

It is actually this latter case which is more realistic in terms of any two-dimensional testing that might be done in the development of a deceleration system. Thus, the question becomes whether the two-dimensional cylindrical laminar wake model, which corresponds to a constant-area viscous wake, is a reasonable approximation of this latter type of wake. Unfortunately, the answer to this question is not completely clear. It is known that laminar wakes initially grow more slowly than turbulent ones and that the two-dimensional laminar wake grows more slowly than the axisymmetric laminar wake, at least for the cold wall case. The flat plate data of Batt and Kubota,¹⁰ for example, indicate a laminar growth rate such that the wake thickness increased by fifty percent over a distance of 10 body lengths. For a slender body, this could correspond to a distance on the order of a 100 base diameters; and this in fact would represent a slow growth rate - slow enough that over a distance of 10 base diameters the wake might be considered as approximately constant in thickness. It appears, however, that it is not possible to generalize on the applicability of the two-dimensional cylindrical laminar wake model. For some cases it may be quite good. For other cases, however, it may not be adequate and the conventional two-dimensional laminar wake calculation procedure should be used where ξ and x are related as shown in Figure 15.

(4) Turbulent Wake

For turbulent flow, a different form for the viscosity relationship must be chosen than that used for the laminar case. In a turbulent flow, the viscosity coefficient is only an effective one (artificially introduced due to the manner in which the governing equations are expressed) and is related to the momentum transfer caused by the fluctuating, mixing type motion. Four different mathematical forms for the turbulent viscosity coefficient are discussed in References 5 and 11. All of these equations may be expressed using the following general form:

$$\mu_o = K \Delta \rho_1 u_1 \left(\frac{\rho_o}{\rho_1} \right)^m \left[1 - n - (-1)^n \left(\frac{\rho_o}{\rho_1} \right)^\ell \frac{u_o}{u_1} \right] \quad (43)$$

The results of Reference 5 and of this study indicate that the best correlation is obtained using values $m = 1$, $n = 0$ and $\ell = 0$, i. e.:

$$\mu_o = K \Delta \rho_o (u_1 - u_o). \quad (44)$$

As discussed in Reference 5, the value of K must be determined experimentally. In this study (see Section IV) the best results were obtained using $K = 0.02$.

Substituting Equation (43) into Equation (23) results in

$$\xi = 2 \frac{u_o}{u_1} \Delta \frac{1}{K \left(\frac{\rho_o}{\rho_1} \right)^{m+1} \left[1 - n - (-1)^n \left(\frac{\rho_o}{\rho_1} \right)^\ell \frac{u_o}{u_1} \right]} \frac{d \left(\frac{u_o}{u_1} \right)}{dx}. \quad (45)$$

Substituting for u_o/u_1 from Equation (22), where $\eta = 0$, and Equation (25) and rearranging yields the following integrable form:

$$\frac{K}{\theta} dx = - \frac{1 - \frac{\xi}{24}}{\frac{\xi}{5} - \frac{\xi^2}{168}} \left\{ \frac{\left(\frac{\rho_1}{\rho_o} \right)^{m+1+\ell}}{\left[(1-n) \left(\frac{\rho_1}{\rho_o} \right)^\ell - (-1)^n \left(1 - \frac{\xi}{24} \right) \right] \xi} \frac{d\xi}{\xi} \right\}. \quad (46)$$

To solve Equation (46), it is first necessary to express ρ_o as a function of ξ . Equation (46) can be rewritten as

$$\frac{\rho_1}{\rho_0} = 1 + \frac{\gamma-1}{2} M_1^2 - \left(1 + \frac{\gamma-1}{2} M_1^2\right) \left(\frac{\theta_{T1}}{\theta_1}\right) \frac{\xi}{24} - \frac{(\gamma-1)}{2} M_1^2 \left(1 - \frac{\xi}{24}\right)^2. \quad (47)$$

Equation (47) now can be substituted back into Equation (46) and the resulting integration can be carried out numerically. In this integration, the lower limit on ξ is ξ_0 which occurs at x equal x_0 and is the effective starting point of the wake with ξ_0 and x_0 defined as before. Calculations have been carried out for the two-dimensional case as part of this effort and are presented in Figures 16 and 17.

In Figure 18 the variation in the parameter (K/θ) ($x - x_0$) with ξ is compared for two-dimensional and axisymmetric wake flow at a Mach number of 3. As may be seen, large differences exist, not only between the cold wall and adiabatic wall cases for each of the two types of wake geometry, but more importantly between the two-dimensional and axisymmetric cases at the same wall condition.

d. Asymptotic Wake Behavior

One measure of the suitability of any approximate method of analysis is to check on the asymptotic behavior of the wake solutions obtained for large x corresponding to the far wake. Taking the laminar case first, it may be shown from Equation (37) that in the limit of large x or small ξ , then x is proportional to ξ^{-2} , i. e., :

$$x \propto \xi^{-2}. \quad (48)$$

Because $\delta \propto \Delta$ for ξ small and $\Delta \propto \xi^{-1}$, then

$$\delta \propto x^{\frac{1}{2}} \quad (49)$$

Also,

$$1 - \frac{u_0}{u_1} \propto x^{-\frac{1}{2}}$$

and

$$1 - \frac{H_0}{H_1} \propto x^{-\frac{1}{2}}. \quad (50)$$

For the turbulent wake case, it may be seen from Equation (46) that, for

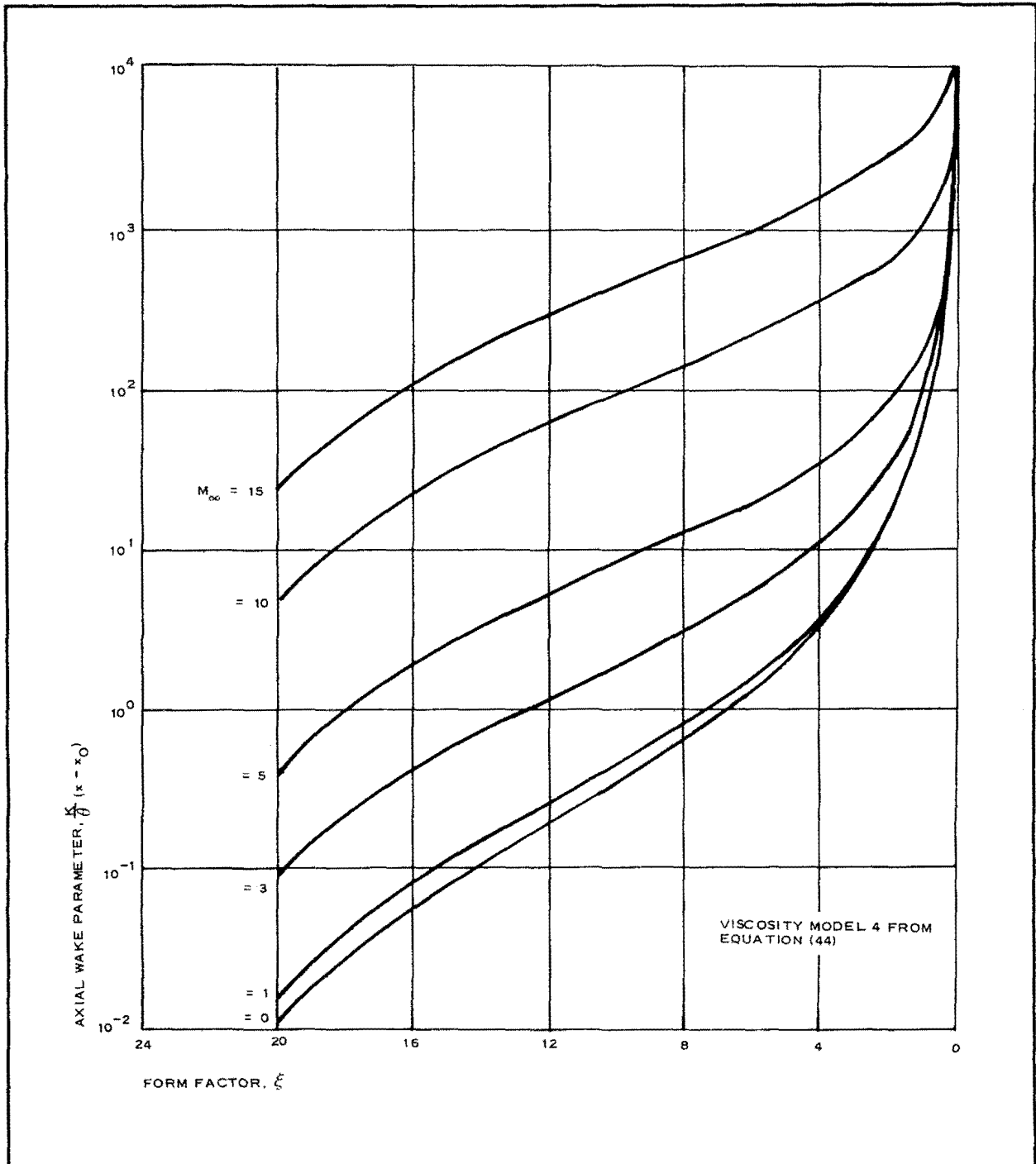


Figure 16 - Axial Wake Parameter versus Form Factor for a Two-Dimensional Turbulent Wake (Adiabatic Wall Case)

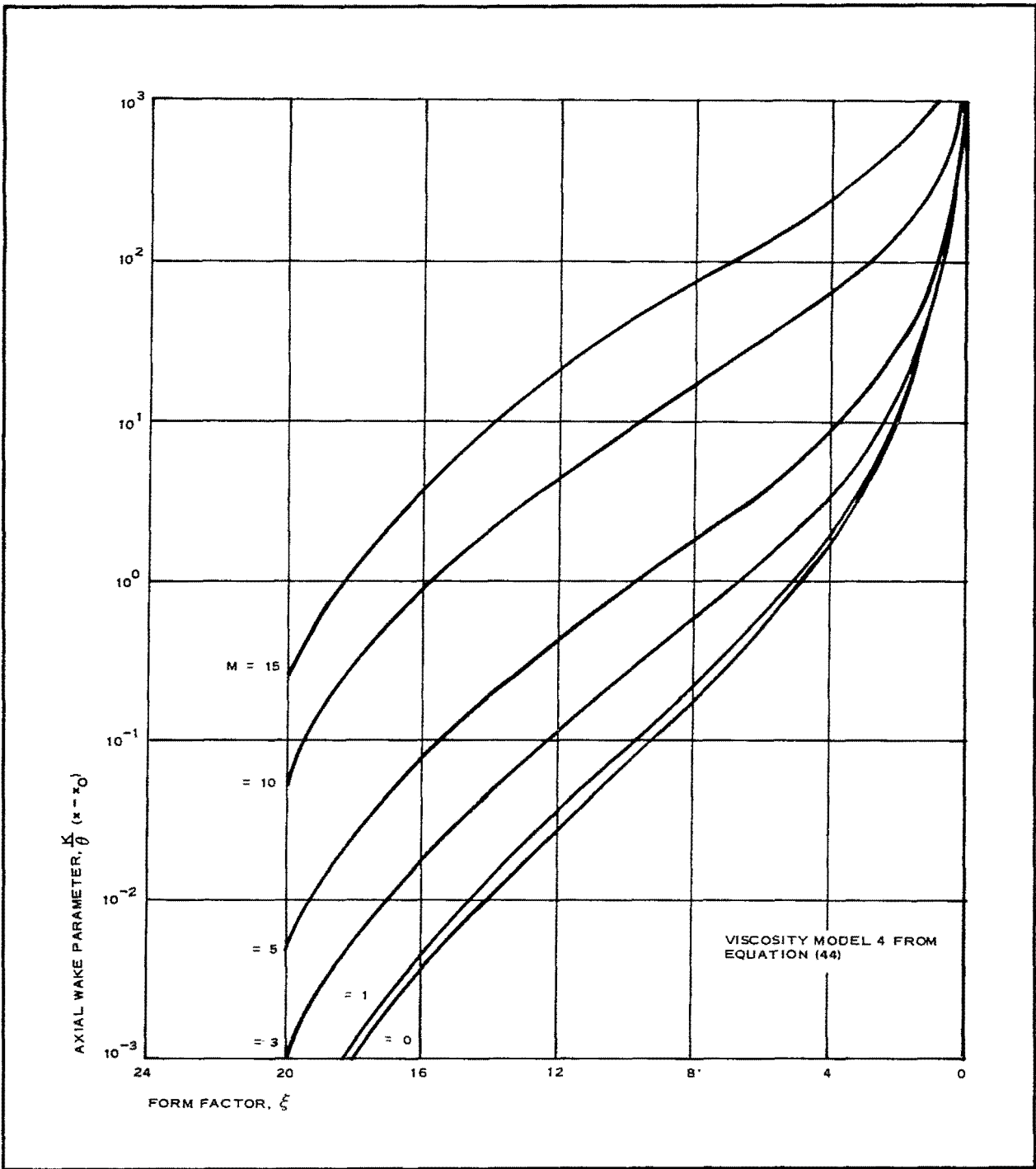


Figure 17 - Axial Wake Parameter versus Form Factor for a Two-Dimensional Turbulent Wake (Cold Wall Case)

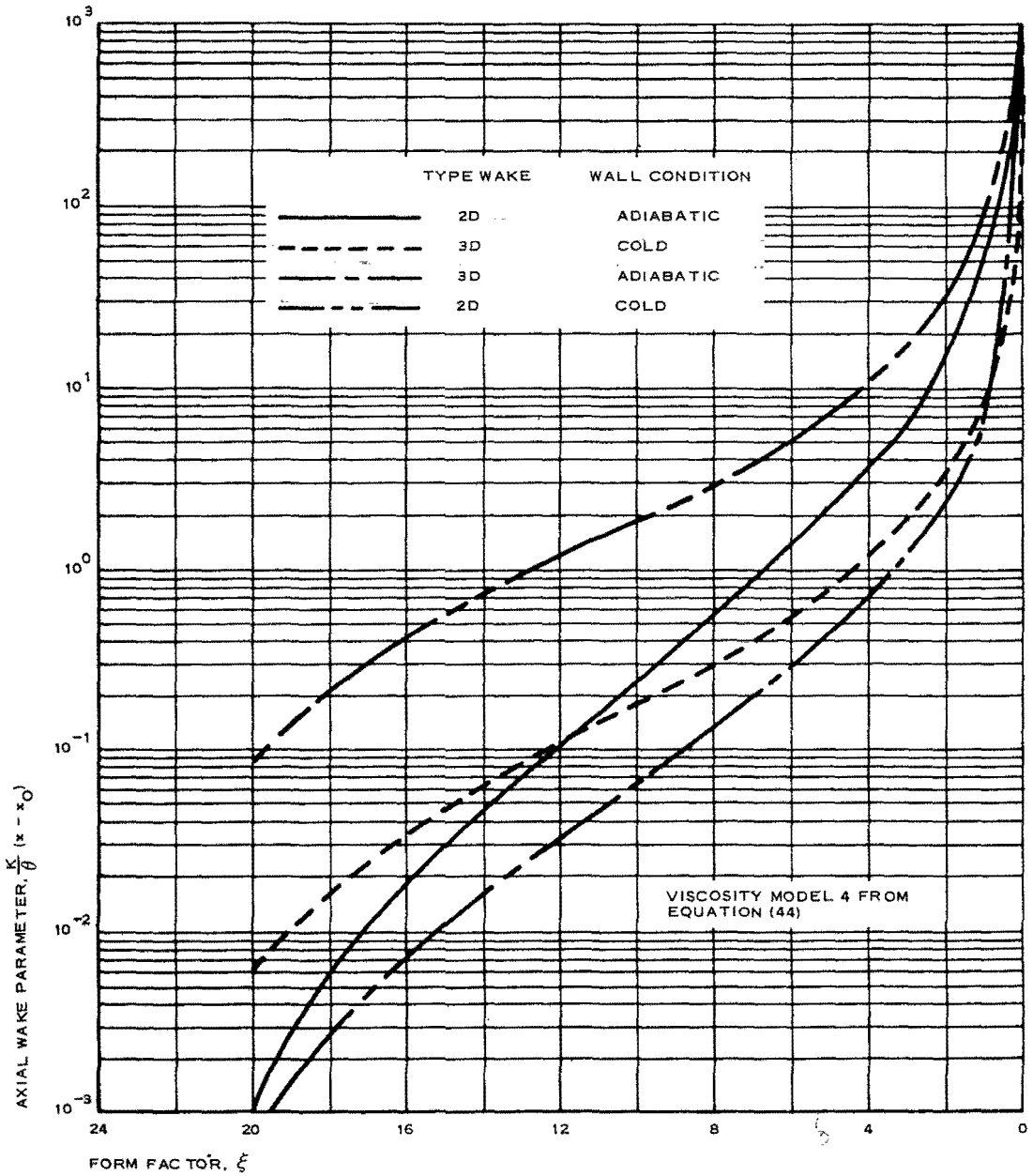


Figure 18 - Axial Wake Parameter Versus Form Factor for Two-Dimensional and Axisymmetric Wakes at $M = 3.0$

Viscosity Model 4 (Equation 44), the asymptotic behavior will be such that for large x

$$x \propto \xi^{-2}. \quad (51)$$

Here again, for small ξ , $\delta \propto \Delta$ and $\Delta \propto \xi^{-1}$. Thus, for the turbulent case

$$\delta \propto x^{\frac{1}{2}}. \quad (52)$$

It, furthermore, follows that

$$1 - \frac{u_0}{u_1} \propto x^{-\frac{1}{2}}$$

and

$$1 - \frac{H_0}{H_1} \propto x^{-\frac{1}{2}} \quad (53)$$

Thus, for the two-dimensional case

$$\delta \propto x^{\frac{1}{2}}$$

and

$$1 - \frac{u_0}{u_1} \propto 1 - \frac{H_0}{H_1} \propto x^{-\frac{1}{2}}. \quad (54)$$

$$(\delta \propto x^{-\frac{2}{3}} \text{ for axisymmetric case})$$

These equations are all in agreement with the results in Reference 8.

4. TWO-DIMENSIONAL INVISCID WAKE SOLUTION

To describe completely the trailing wake behind a supersonic body, both the viscous inner wake and inviscid outer wake characteristics, e.g., velocity, density, and temperature profiles, must be known. The calculation of the viscous inner wake depends on the forebody boundary layer. An analysis of the two-dimensional case has been discussed in the preceding pages. The inviscid wake characteristics, on the other hand,

depend on the forebody bow shock wave strength and shape, and the subsequent expansion over the body. Approximate calculations of this portion of the wake flow may be carried out using a mass flow balance and certain assumptions concerning the physical nature of the flow.

Consider a supersonic vehicle where it is assumed that the vehicle bow shock wave shape and the pressure distribution along the wake axis are both known, from either experiment or theory. For blunt bodies at hypersonic speeds, blast wave theory may be used to approximate both the bow shock shape and the pressure distribution on the wake axis. For supersonic speeds, on the other hand, the pressure in the wake may be approximated as being equal to p_∞ , the free stream pressure, and the shock wave shape, though not as critical, would in general be obtained from either numerical flow field calculations or experiment.

By maintaining conservation of mass, a mass balance may be written which relates the mass flow in the free stream at the shock through an element of area in the free stream of unit width and a distance r_s in height and a similar area in the wake region a distance r in height. This relation is

$$\rho_\infty V_\infty r_s = \int_{\delta^*}^r \rho u \, dr \quad (55)$$

Note that the integration of the right hand side of Equation (55) starts at δ^* , instead of zero to account for the displacing of streamlines by the viscous wake phenomena. The wake displacement thickness, δ^* , is defined by the relation

$$\rho_1 u_1 \delta^* = \int_0^\delta (\rho_1 u_1 - \rho u) \, dr \quad (56)$$

and may be determined from Equation (33).

Equation (55) may be considered to be a relation between properties on a streamline passing through a point on the bow shock at a shock height r_s and properties on the same streamline downstream of the body at a point A, a distance r from the axis of the wake. With the bow shock shape known, then a specific value of r_s corresponds to specific properties immediately behind the bow shock for the streamline passing through that point. If it is assumed that the flow is isentropic in expanding from the shock wave on downstream to point A, Equation (55) is a relation between two points with the same entropy, or, in other words, the same total pressure. The assumption of isentropic flow behind the bow shock means that any secondary shocks (e. g., the recompression shock where the wake necks down) produce negligible changes in entropy.

Equation (55) thus provides a means for calculating the total pressure or entropy at point A, a distance r from the wake axis. Furthermore, the total enthalpy is known since the inviscid flow may be considered adiabatic. Finally, with the pressure distribution along the axis of the wake known, an estimate of the static pressure in the inviscid wake can be made by assuming that there are no pressure gradients radially in the wake region, *i. e.*, $dp/dr = 0$. The complete state of the gas at a point A in the inviscid wake is thus completely specified in terms of the total pressure, the total enthalpy, and the static pressure.

To facilitate calculations using the above analysis, the following transformation is introduced:

$$\begin{aligned} \rho u dr &= \rho_{\infty} V_{\infty} dm. \\ x_1 &= x. \end{aligned} \quad (57)$$

Equation (55) may then be rewritten as

$$\rho_{\infty} V_{\infty} R_s = \int_{\delta_m^*}^m \rho_{\infty} V_{\infty} m dm \quad (58)$$

or

$$r_s = m_{k+1} - \delta_m^* \quad (59)$$

where δ_m^* is the transformed displacement thickness, and

$$\rho_1 u_1 \delta_m^* = \rho_{\infty} V_{\infty} \delta_m^*. \quad (60)$$

Thus, from Equations (59) and (60), and assuming δ_m^* known from an analysis of the viscous wake, the entropy and total pressure at a point A, lying a distance m from the axis in the transformed plane, may be determined as being equal to that immediately behind the bow shock wave at a height r_s . With the total pressure or entropy known for a streamline, and with an estimate of the static pressure, the local Mach number at point A may be determined. This, together with the total enthalpy, gives the static enthalpy or temperature. The complete state of the gas, including the velocity and density, at such a point is thus specified; and the variation in fluid properties in the transformed (m, x_1) plane may thus be determined. To transfer the results back into the (x, r) plane, Equation (57) may be used with the result that r and m are related by the equation

$$\int_{\delta^*}^r dr = \int_{\delta_m^*}^m \frac{\rho_{\infty} V_{\infty}}{\rho u} dm \quad (61)$$

Since $\rho_{\infty} V_{\infty} / \rho u$ is known as a function of m , this calculation may be readily carried out using numerical techniques for the integration. The variation of such fluid properties as velocity, Mach number, and temperature may thus be calculated as a function of r , the radial distance from the axis of symmetry. Previous results of such calculation are reported in References 12 and 13.

5. UNIFICATION OF VISCOUS AND INVISCID WAKE RESULTS

a. General

To provide a generalized wake calculation procedure applicable to both two-dimensional and axisymmetric flow, the results of the present analysis as described in Items 3 and 4 have been combined with those of the previous axisymmetric analysis.⁵ These unified results are summarized in Tables II and III where the equations actually used in wake calculations are presented.

b. Unified Viscous Wake Results

For the viscous wake case, the important equations are those in Table IIA which includes (1) equations for matching the wake and boundary layer momentum defects; (2) velocity profile items of the transformed radial coordinate, η ; (3) definition of the viscous wake form factor; (4) transformed wake thickness, Δ ; (5) viscous wake displacement thickness, δ^* ; (6) total enthalpy profile as related to the velocity profile; and (7) the relationship between the actual physical radial coordinate, r , and the transformed variable, η . In these equations, the convention used is that $j = 0$ for two-dimensional flow and $j = 1$ for axisymmetric flow.

These equations, together with such standard relations as the thermal equation of state,

$$\begin{aligned} \rho &= \frac{p}{R_1 T} \\ &= \frac{\gamma}{\gamma - 1} \frac{p}{h}, \end{aligned}$$

the total enthalpy equation

$$h = H - \frac{u^2}{2},$$

TABLE II - UNIFIED VISCOUS WAKE RESULTS

	Equation number		Unified result *
	Text counterpart	Unified	
A - Viscous wake profiles and thickness			
Matching of boundary layer and wake momentum defects	17	62	$\rho_B u_B^2 \theta_B (\pi D)^j = \rho_1 u_1^2 \pi^j \theta^j + 1$
Velocity profile	22	63	$\frac{u}{u_1} = \left(6\eta^2 - 8\eta^3 + 3\eta^4 - 1 \right) \frac{\xi}{24} + 1$
Form factor	23	64	$\xi = \left(\frac{\rho_1}{\rho_0} \right)^{1-j} \left(\frac{u_0}{u_1} \right) \Delta^2 \left(\frac{\rho_1}{\mu_0} \right) \frac{du_0}{dx}$
Momentum thickness	25	65	$\left(\frac{\theta}{\Delta} \right)^{j+1} = \frac{\xi}{(j+1)60} - \left(\frac{11}{30} \right)^j \frac{\xi^2}{2016}$
Displacement thickness	33	66	$\delta^* = \Delta \left\{ \frac{H_1}{h_1} - \frac{\xi}{(j+1)60} \cdot \frac{H_1}{h_1} \left(\frac{\theta_{T1}}{\theta_1} \right)^{j+1} - \left(\frac{\rho-1}{2} \right) M_1^2 \right.$ $\left. \left[1 - \frac{\xi}{(j+1)30} + \left(\frac{11}{30} \right)^j + \frac{\xi^2}{2016} \right] - 1 + \frac{\xi}{(j+1)60} \right\}^{1/(j+1)}$

* In these equations, j = 1 for axisymmetric flow, and j = 0 for two-dimensional flow.

TABLE II - UNIFIED VISCOUS WAKE RESULTS (Continued)

	Equation number		Unified result*
	Text counterpart	Unified	
Total enthalpy profile	28 - 29	67	$\frac{H_o}{H_1} = 1 - \left(1 - \frac{h_w}{H_1}\right) \frac{u_1}{u_B} \left(1 - \frac{u_o}{u_1}\right)$
Radial coordinate	32	68	$\left(\frac{r}{\Delta}\right)^{j+1} = (j+1)\eta^j \left\{ \frac{H_1}{h_1} \cdot \frac{\eta}{j+1} + \left(\frac{\theta_{T1}}{\theta_1}\right)^{j+1} \cdot \frac{H_1}{h_1} \cdot \frac{\xi}{24} \left(\frac{6}{3+j}\eta^3 - \frac{8}{4+j}\eta^4 + \frac{3}{5+j}\eta^5 - \frac{1}{j+1}\eta \right) - \frac{(\nu-1)M_1^2}{2} \right.$ $\left. \left[\frac{\eta}{j+1} + \frac{\xi}{12} \left(\frac{6}{3+j}\eta^3 - \frac{8}{4+j}\eta^4 + \frac{3}{5+j}\eta^5 - \frac{1}{j+1}\eta \right) + \frac{\xi^2}{576} \left(\frac{\eta}{j+1} - \frac{12}{3+j}\eta^3 + \frac{16}{4+j}\eta^4 + \frac{30}{5+j}\eta^5 - \frac{96}{6+j}\eta^6 + \frac{100}{7+j}\eta^7 - \frac{48}{8+j}\eta^8 + \frac{9}{9+j}\eta^9 \right) \right] \right\}$

*In these equations, j = 1 for axisymmetric flow, and j = 0 for two-dimensional flow.

TABLE II - UNIFIED VISCOUS WAKE RESULTS (Continued)

	Equation number		Unified result*
	Text counterpart	Unified	
B - Form factor equations for described viscous wake cases			
Laminar conventional wake	37	69	$\frac{x}{\theta} \cdot \frac{1}{Re_{\theta}} = \frac{Re_x}{Re_{\theta}^2} = - \int_{24}^{\xi} \frac{\left(1 - \frac{\xi}{24}\right)}{12(1+j)\left(\frac{\theta}{\Delta}\right)^2} \cdot \frac{d\xi}{\xi}$
Laminar cylindrical wake	-	70	$\left[\left(1 + \frac{\nu-1}{2} M_1^2\right) \left(1 - \frac{\theta_T^2}{\theta_1^2} \cdot \frac{\xi}{24}\right) - \frac{\nu-1}{2} M_1^2 \left(1 - \frac{\xi}{24}\right)^2 \right]^j \cdot \frac{d\xi}{\xi}$ <p>$\xi = 24$</p>

*In these equations, $j = 1$ for axisymmetric flow, and $j = 0$ for two-dimensional flow.

TABLE II - UNIFIED VISCOUS WAKE RESULTS (Continued)

	Equation number		Unified results *
	Text counterpart	Unified	
Turbulent wake	46	71	$\frac{K}{\theta} dx = - \frac{1}{12(j+1)} \cdot \frac{1 - \frac{\xi}{24}}{\left[\frac{\xi}{(j+1)60} - \left(\frac{11}{30}\right)^j \frac{\xi^2}{2016} \right]^{1/j+1}} \cdot \frac{(\rho_1/\rho_0)^{m+1-j+p}}{\left[(1-\gamma)(\rho_1/\rho_0)^p - (-1)^n \left(1 - \frac{\xi}{24}\right) \right]} \cdot \frac{d\xi}{\xi}$
	47	72	<p>where</p> $\frac{\rho_1}{\rho_0} = 1 + \frac{\gamma-1}{2} M_1^2 - \left(1 + \frac{\gamma-1}{2} M_1^2 \right) \left(\frac{\theta_{T1}}{\theta_1} \right)^{j+1}$ $\frac{\xi}{24} - \left(\frac{\gamma-1}{2} \right) M_1^2 \left(1 - \frac{\xi}{24} \right)^2$

* In these equations, j = 1 for axisymmetric flow, and j = 0 for two-dimensional flow.

TABLE III - UNIFIED INVISCID WAKE RESULTS

Description	Equation number		Unified result*
	Text counterpart	Unified	
Radial streamline coordinate at the shock	59	73	$r_s^{j+1} = m_{K+1}^{j+1} \delta_m^{*j+1}$
Transformed displacement thickness	60	74	$\rho_1 u_1 (\delta^*)^{j+1} = \rho_\infty u_\infty \delta_m^{*j+1}$
Radial streamline coordinate in the inviscid wake	61	75	$\int_{\delta^*}^r r^j dr = \int_{\delta_m^*}^m \frac{\rho_\infty v_\infty}{\rho u} m^j dm$

*In these equations, $j = 1$ for axisymmetric flow; $j = 0$ for two-dimensional flow.

and those that relate static and total flow properties are, with one exception, sufficient for the calculation of the viscous wake properties.

The one exception is the equation relating the form factor with the axial, x/d , position in the wake. The required equations for this are presented in Table IIB. For two of the three cases presented - the conventional laminar and turbulent wake cases - the equations are of an integral form and their evaluation must be carried out numerically. Only for the "cylindrical" wake is the form factor equation relatively simple.

Knowing the properties at the edge of the viscous wake, e.g., the pressure, velocity, and total enthalpy, and knowing the wake momentum thickness based on the matching of the wake and boundary layer momentum defects, a complete viscous wake solution can be carried out for both two-dimensional and axisymmetric flow.

c. Unified Inviscid Wake Results

With regard to the inviscid wake, the necessary equations for carrying out calculations have been unified and summarized in Table III. The same j -convention is used here, and the equations presented include those required for calculating (1) the point where the streamline crosses the bow shock wave, (2) the transformed viscous wake displacement thickness, and (3) the radial location of the streamline in the inviscid wake region. These equations, together with the previously mentioned standard relationships, complete the inviscid wake analysis and allow for the calculation of two-dimensional and axisymmetric inviscid wake flows.

6. PROGRAM MODIFICATIONS FOR SUBSONIC OR INCOMPRESSIBLE WAKES

If calculations are to be carried out for subsonic or transonic free stream conditions, or for the limiting case of incompressible flow, there are some minor modifications that need to be made. In discussing these, consider first the case of subsonic, but not incompressible, flow. This case is presently handled with virtually the only changes being in terms of the inputs to the calculation. For example, the forebody static pressure distribution is inputted in terms of body position and the local total pressure is inputted as equal to the free stream total pressure for all points on the forebody. Best results are achieved when the forebody boundary layer transition criteria is inputted by the user (instead of relying on the internal transition Reynolds number correlation) and the wake transition Reynolds number, $Re_{\delta_{tr}}$, is inputted since the correla-

tion for it is particularly poor for M_1 less than unity. Finally, for the subsonic case, no bow shock wave shape is used and no inviscid wake calculations are carried out. It should be noted here that the last sentence really contains the definition of what is meant in the preceding by subsonic flow. Thus, any flow without a bow or leading edge shock wave, whether it be purely subsonic or transonic, is taken care of in this manner.

If the flow is incompressible, then there are further changes to be made in the calculation procedure. The first change is based on the recognition that an incompressible flow is a special flow in which the Mach number is zero, but the flow velocity is finite. Thus, one must a priori set M_∞ , M_e , and M_1 all equal to zero and input the free stream velocity V_∞ . It follows that $T_o = T_\infty$, $T_w = T_\infty$, and $p_t = p_\infty + 1/2 \rho_\infty V_\infty^2$ are also inputted. Furthermore, everything which is inputted for the subsonic flow case must necessarily be an input for this case also.

In calculating the flow properties over the forebody, the local velocity is calculated from the equation

$$u_e = V_\infty \left(\frac{p_t - p_e}{\frac{1}{2} \rho_\infty V_\infty^2} \right)^{\frac{1}{2}} \quad (76)$$

and the density and viscosity are set equal to free stream values ρ_∞ and μ_∞ which also must be input (this allows for fluids other than air, e.g., water). The laminar boundary layer equations as outlined in Appendix A are then used in their original form. However, for the turbulent boundary layer case two changes are made in the equations to be used. Thus, the equation

$$\xi_T^* = \frac{1}{\left(\frac{r}{R}\right)^{1.2155j}} \int_{\frac{s_1}{R}}^{\frac{s}{R}} \left(\frac{r}{R}\right)^{1.2155j} d\left(\frac{s}{R}\right) \quad (77)$$

replaces Equation (106) of Appendix A, and the equation

$$\left(\frac{\theta_{tr}}{R}\right)^{1.2155} = \left[\frac{\theta_{tr}(TR)}{R}\right]^{1.2155} \frac{\left[\frac{r(TR)}{R}\right]^{1.2155j}}{\left(\frac{r}{R}\right)^{1.2155j}} + 0.01173 \xi_T^* \left(\frac{\mu_\infty}{\rho_\infty u_e R}\right)^{0.2155} \quad (78)$$

replaces Equation (107) of Appendix A.

Once the boundary layer properties have been correctly calculated with the above modifications, then the calculation of the viscous wake profiles

may be accomplished. It should be noted that for a local wake Mach number of $M < 1$,

$$\frac{p_{Tm}}{p_{\infty}} = \frac{p_T}{p_{\infty}}; \quad (79)$$

and for $M_1 = 0$,

$$\frac{p_T}{p_{\infty}} = 1 + \frac{\rho_{\infty} V_{\infty}^2}{p_{\infty}} \left(\frac{u}{u_1} \right)^2. \quad (80)$$

Here u_1 is equal to V_{∞} for the incompressible viscous wake.

7. MATCHING VISCOUS AND INVISCID WAKES

In calculating the wake profiles, the viscous and inviscid portions of the wake are calculated separately and it is necessary to properly match these two regions. The viscous wake is a boundary layer type calculation based on properties of the zero streamline, while the inviscid wake is displaced by a distance equal to the displacement thickness and in the present analysis is calculated using a mass balance approach. In the limit layer of an infinite Reynolds number (the only case for which boundary layer theory is mathematically exact) these two flow regions will be automatically matched. For the finite Reynolds number cases of practical interest, however, there is a mismatch in the calculated profiles. The procedure employed in this document was to connect the results of the two wake portions by simply fairing them together. Although reasonable results are obtained in this manner, it is justifiable only from an experimental standpoint. In Reference 5, an iterative procedure was used to match the two wake portions. The major criticism of such a method is that it implies a logical solution, but is actually not theoretically justifiable because it fails to account for the matching of the viscous wake profiles with inviscid profiles of finite gradients.

The method of this document apparently offers a reasonably satisfactory approach; although it appears desirable to eventually account for the finite gradients at the edge of the viscous wake by a more theoretically satisfactory method.

SECTION IV - CORRELATION STUDY

GENERAL

In this section, results and developments of previous sections are analyzed to determine their utility to the analysis of two- and three-dimensional wake flows. Specifically, this includes (1) a correlation analysis of the tow-channel wake results with comparable results in a gas and (2) the investigation and correlation of two- and three-dimensional theoretical and experimental wind-tunnel wake results.

Data in this section is compared for three basic axisymmetric configurations (and their two-dimensional counterparts):

1. Cone-cylinder
2. 120 deg cone
3. Blunted cone-cylinder-flare

These shapes were chosen because applicable wind-tunnel and tow-channel data were generally available and because they are basically representative of a wide variety of different body geometries.

Tow channel data are obtained in various combinations, with approximately 50 different forebody geometries and 12 different decelerator configurations (see Volume II).

CORRELATION OF TOW-CHANNEL RESULTS

Correlation Methods

In an attempt to quantitatively relate wake characteristics in water with "analogous" compressible wake characteristics in air, correlation between forebody inviscid flow fields and boundary layers first must be established. Two potential flow-field correlation methods were investigated: (1) the so-called first modification of the gas-hydraulic analogy and (2) a direct correlation between theoretical water and air results. The first method is suitable for predicting two-dimensional gas flow fields about slender bodies with attached shock waves. The second method is not limited to slender bodies but provides for an accurate prediction of the flow field only in the vicinity of the bow shock. Basic differences in the structure of the boundary layer between incompressible and compressible fluid flows also indicate that a general correlation of the viscous wake is not possible. Under certain conditions, however, these differences may not be too severe and a degree of correlation may be achieved.

As part of this correlation effort, a somewhat independent study was made to determine if detached bow waves in free-stream water could be used

to predict the shape of detached bow shocks in air for corresponding bodies. Such a capability would be useful in and of itself since shock shape coordinates are a necessary input to the theoretical wake computer program to construct complete wake profiles. In all cases considered, very good results were achieved by comparatively simple means. Because shock shape geometry is of interest to many high speed flow problems, these results, subject to further substantiation, are considered to be one of the most significant aspects of the tow channel utility. A complete discussion of the method used will be given later in this subsection.

b. Investigation of the Inviscid Flow Fields

(1) Flow Characteristics Across Shock Waves and Hydraulic Jumps

As mentioned in Section II, the basic gas-hydraulic analogy (see Volume II) is strictly applicable only to the so-called "hydraulic" gas which among other things is isentropic. Consequently, the basic analogy itself is not valid for gas flows in which shock waves are present even if all conditions are satisfied (i. e., $\gamma = 2$, flow irrotational, etc.). The magnitude of the discrepancy can be readily determined, however, as follows:

From the analogy,

$$\frac{p_2}{p_1} = \left(\frac{\rho_2}{\rho_1} \right)^2$$

$$= \left(\frac{d_2}{d_1} \right)^2;$$

therefore,

$$\frac{p_2}{p_1} \left(\frac{\rho_1}{\rho_2} \right)^2 = 1. \tag{81}$$

From gas dynamics,

$$\frac{p_2}{\rho_2^\gamma} = \frac{p_1}{\rho_1^\gamma} e^{\frac{(s - s_1)}{c_v}};$$

therefore,

$$\frac{p_2}{p_1} \left(\frac{\rho_1}{\rho_2} \right)^\gamma = e^{\frac{(s - s_1)}{c_v}} \tag{82}$$

The exact analogy, therefore, requires that the entropy increase (Δs) be zero. The error incurred in using the exact analogy can be indicated by

plotting Equations (81) and (82). This is done in Figure 19 where, for comparison, results for both a $\gamma = 2$ and $\gamma = 1.4$ gas have been presented. It can be observed that the exact analogy is relatively more accurate for air than for a $\gamma = 2$ gas, although large errors are incurred for both at $M_1 \sin \theta$ values greater than approximately 2. These results suggest, however, that comparatively good results can be obtained using the exact analogy for $M_1 \sin \theta$ values less than approximately 2. At $M_1 \sin \theta = 2$, the relative errors for air and for a $\gamma = 2$ gas are 2.91 percent and 5.66 percent respectively. With the use of the oblique shock theory (i.e., Equation (1) from Section II), it can also be shown that, for small deflection angles, the wave angle produced is nearly independent of the specific heat ratio, γ . This is illustrated in Figure 20 where wave angle, θ , has been plotted as a function of deflection angle, δ for the conditions indicated. Figures 19 and 20 indicate that the exact analogy may be a reasonably good approximation to the inviscid two-dimensional air flow field about slender bodies.

(2) First Modification Method

The first modification of the direct analogy was proposed by Harleman in Reference 14. In that reference, it was demonstrated that the properties behind an attached shock from a slender wedge ($\delta = 9$ deg) could be obtained with good accuracy by equating the density ratio across the shock in air with the depth ratio across a hydraulic jump. It was shown there

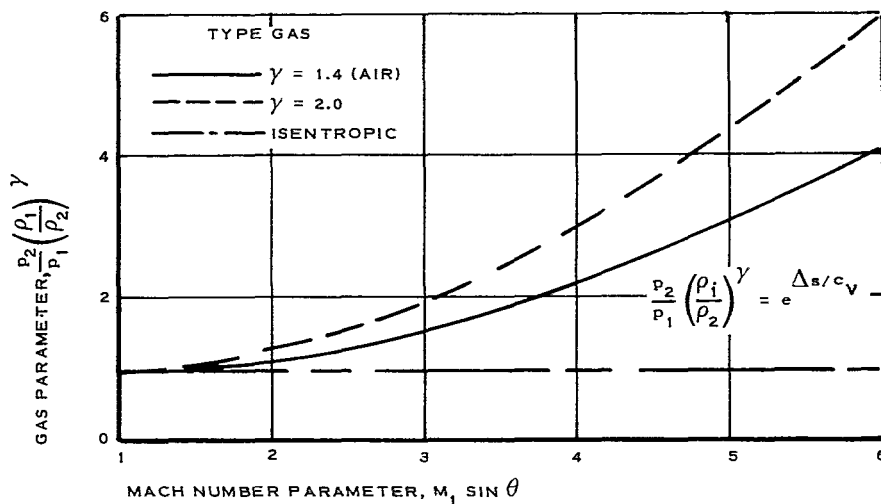


Figure 19 - Isentropic Gas and Actual Gas Results Across a Shock Wave

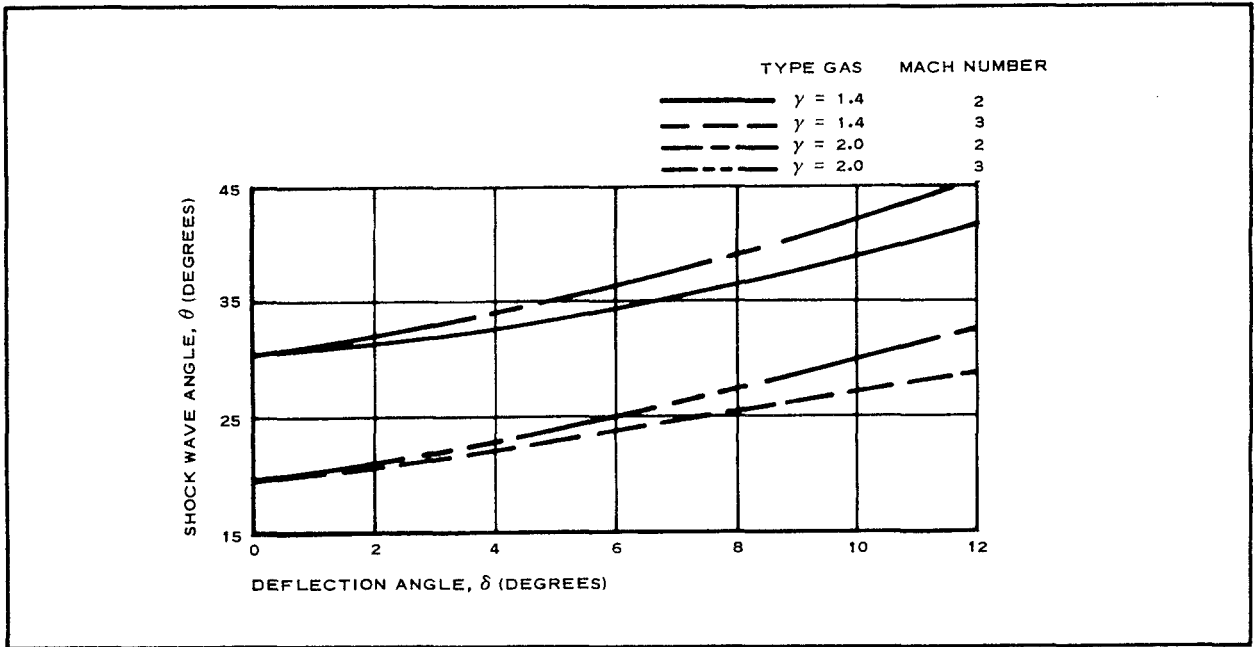


Figure 20 - Attached Bow Shock Angles at Small Deflection Angles

that the depth ratio corresponds more closely with the density ratio than it does with either the temperature ratio or the square root of the pressure ratio. Hence, this technique used depth ratio to determine density ratios, which in turn were used to predict other properties through conventional gas dynamic relationships. The results presented under Item 2, b, (1), above, and the agreement achieved between attached hydraulic jumps and oblique shock theory (Figure 9, Section II), tend to support the validity of this method. It is again emphasized, however, that the utility of this method is confined to slender bodies that basically satisfied the indicated requirements of Figures 19 and 20.

(3) Direct Correlation Between Theoretical Air and Water Results

The question now arises as to the general case when small deflection angle assumptions are not necessarily valid and $M_1 \sin \theta$ may be large. This general case presents problems that are not readily amenable to a simple analysis. In the first place, the bow wave shape in water may be substantially different from that obtained for a geometrically similar body in two-dimensional air. Secondly, the air shock may exhibit a high rate of local curvature, especially if it is detached, producing a large entropy gradient on the downstream side. This in turn makes the inviscid flow region highly rotational and, thus, theoretically invalidates the hydraulic analogy.

In spite of these limitations, it is believed instructive to consider results obtained immediately behind a detached bow wave in water and air. For purposes of this discussion, it will be assumed that the two shock shapes are the same.

From the gas-hydraulic analogy, the total-to-static water depth ratio is analogous to the total-to-static density ratio, i. e.,

$$\frac{d_t}{d} = \frac{\rho_t}{\rho}$$

for an isentropic, $\gamma = 2$ gas.

Across a hydraulic jump, this relationship is no longer valid; i. e.,

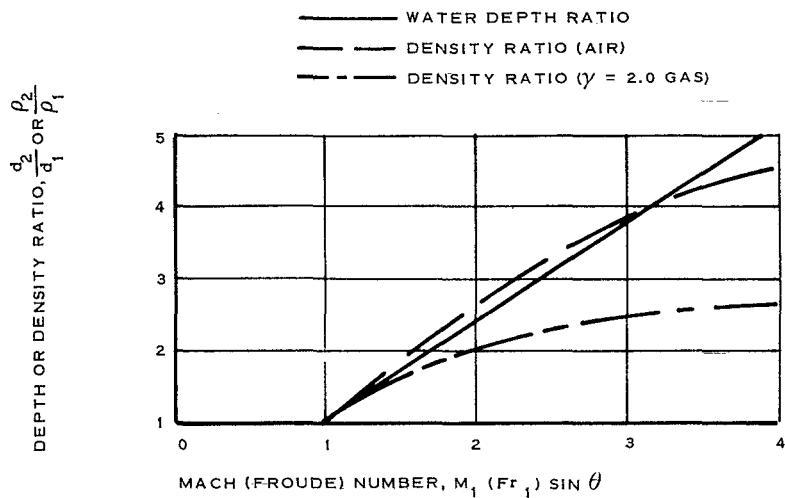
$$\frac{d_2}{d_1} \neq \frac{\rho_2}{\rho_1}.$$

The discrepancy between the two ratios in the above inequality can be determined, however. Across a slant hydraulic jump, the ratio d_2/d_1 is given as a function of the reference Froude number, Fr_1 , by Equation (6). Across an oblique shock, the ratio ρ_2/ρ_1 is given as a function of Mach number by the following expression from gas dynamics.

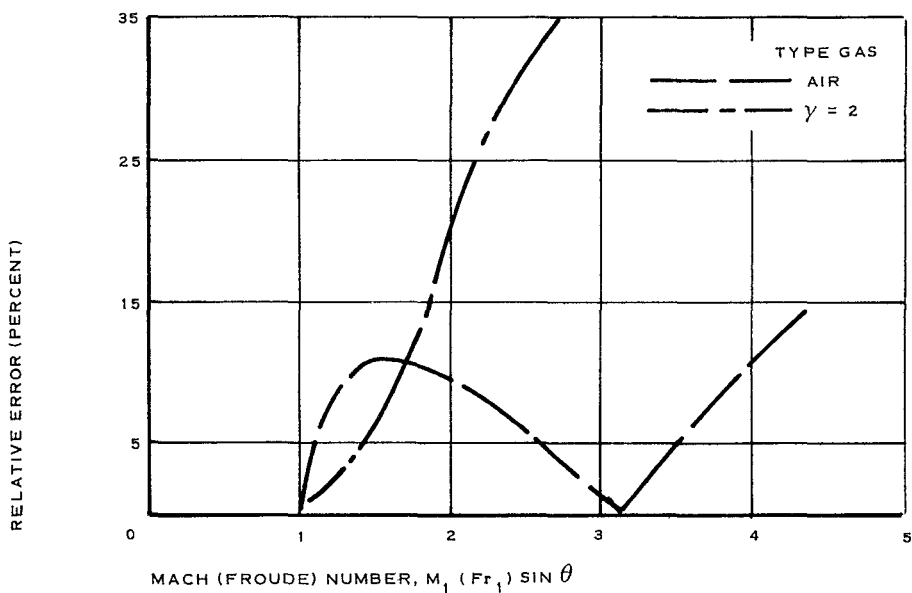
$$\frac{\rho_2}{\rho_1} = \frac{(\gamma + 1)M_1^2 \sin^2 \theta}{(\gamma - 1)M_1^2 \sin^2 \theta + 2} \quad (83)$$

Results are plotted in Figure 21 for the water depth ratio and for a $\gamma = 2$ and a $\gamma = 1.4$ gas. These curves indicate that the water depth ratio corresponds more closely with air results than with the $\gamma = 2$ gas. These results are closely related to those of Figure 19 and constitute a part of the justification for the first modified method previously discussed.

It is apparent from Figure 21B that reasonably good results are obtained using the depth ratios to approximate the density ratio behind the wave to a $M \sin \theta$ value of approximately 4 (generally less than 10 percent). This value, in a sense, is actually beyond the practical usable limit of the tow channel. This is because the theoretical water results are no longer valid once "cresting" of the hydraulic wave occurs. In the present experiments, no evidence of this condition was seen for the slender bodies tests, and other results (e. g., Reference 15) indicate that comparatively high simulated Mach (Froude) number values can be reliably used. For blunt bodies, however, "cresting" was observed between simulated Mach numbers of 2.5 and 3. This condition represents an analogous loss in the stagnation temperature and cannot be accounted for in the water-air correlation.



A - WATER DEPTH RATIOS AND GAS DENSITY RATIOS ACROSS BOW WAVE



B - RELATIVE ERROR INCURRED

Figure 21 - Static Depth and Density Ratios Across Oblique Wave as Function of Upstream Mach (Froude) Number

Boundary Layer Considerations

One obvious deficiency of tow channel test data and the mathematical correlation relationships available is that it is not believed possible to generally relate the results to a compressible boundary layer. Since it is an extension of the boundary layer which forms the viscous wake, this is tantamount to saying that the viscous wake profiles cannot generally be predicted from water results. This lack of correlation results from considerations other than the normal similarity parameters that must be taken into account. Certainly, it is expected that, at the very least, the basic similarity laws for the forebodies (*i. e.*, similar body geometry, gas Mach number equal to water Froude number, and equivalent Reynolds numbers) would have to be satisfied. The relative initial size of the viscous wake, however, is also determined by the nondimensionalized boundary layer momentum thickness at the base of the forebody. In general, this is not the same for a compressible gas and incompressible water. This can be shown by considering the nondimensionalized boundary layer thickness for a flat plate.

For incompressible flow,

$$\frac{\delta_B}{L} = \frac{5}{(\text{Re}_L)^{\frac{1}{2}}};$$

for compressible flow,

$$\frac{\delta_B}{L} = \frac{5}{(\text{Re}_L)^{\frac{1}{2}}} f(M),$$

where L is some characteristic length. From these equations, it is apparent that the dimensions of the viscous wake cannot, in general, be equal. An indication of the discrepancy incurred in the wake is shown graphically in Figure 22. These results were obtained using the wake calculation procedure described in Section III. In one case, the program was modified for incompressible flow calculations using the properties of water and a free-stream velocity value corresponding to a Froude number value of 2.2 at a water depth of 0.2-in. To provide the desired comparison, a compressible gas case was also calculated. For this case the free-stream Mach number is 2.2 and the model size and free-stream Reynolds number conditions are equivalent to those of the incompressible case. The computer results were used in both cases in order that control over all other conditions could be maintained and thus provide for an equal reference base. It is also noted that the stereo model of the water wake did not enable differentiation between the viscous and inviscid portions.

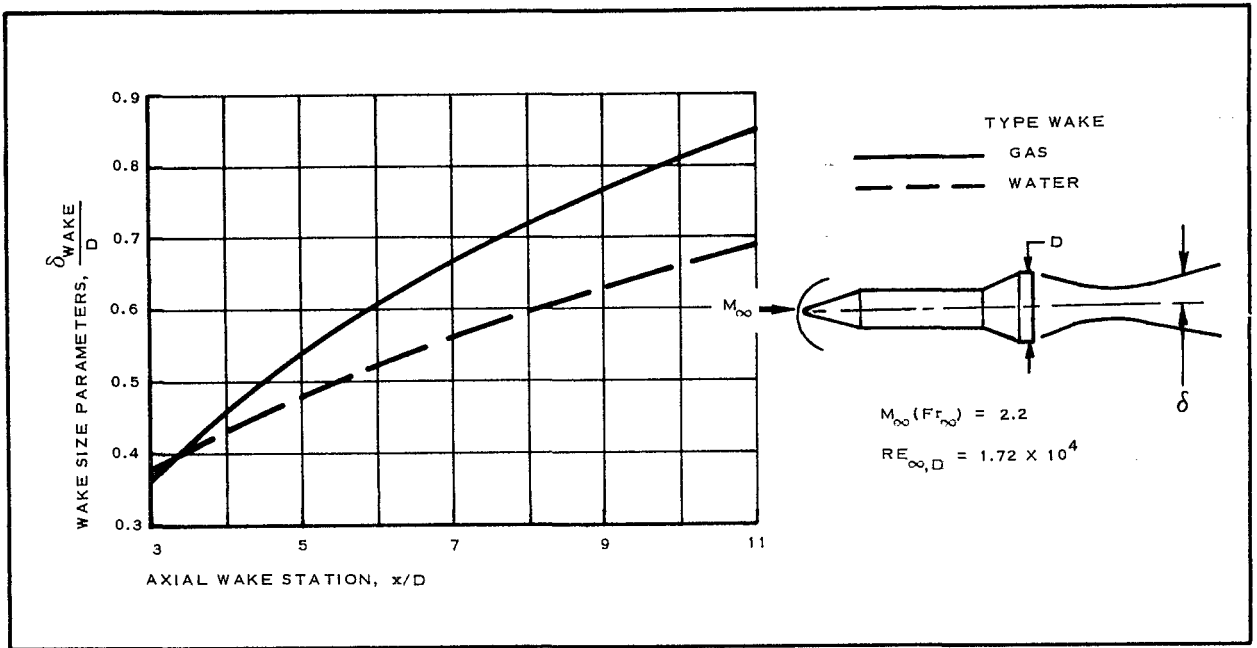


Figure 22 - Comparison of Theoretical Compressible Wake and Water Wake Size for Blunted Wedge-Block-Flare Forebody

From the results of Figure 22, it is apparent that the viscous wakes are not the same size and that water results, no matter how accurately obtained, will not provide completely valid quantitative compressible wake results for all x/D cases. It could presumably be argued that certain boundary layer characteristics between a compressible gas and water could be matched by altering body coordinates or Reynolds number conditions. Such techniques then would violate the basic assumed similarity requirements, however, and it appears doubtful that generally good agreement could be attained by this method.

Although the results of Figure 22, for the reason just discussed, indicate different wake dimensions, it should be pointed out that at the lower x/D -values the discrepancy is not too severe. This suggests then that, under certain conditions, the tow channel water profiles might still provide a reasonably good approximation to compressible viscous wake results. Intuitively, one might expect that the best relative correlation of the viscous wake profiles would be achieved when the inviscid flows are the same since the viscous and inviscid wake flows are dependent upon one another.

d. Comparison of Tow-Channel and Two-Dimensional Wind-Tunnel and Theoretical Wake Results

In view of the previous discussion, it is of interest now to make an actual comparison between wake results for two-dimensional air and water. The body used for comparison due to the availability of both tow channel and wind-tunnel data was a slender wedge-block (two-dimensional cone-cylinder) having a semiapex angle of 12.66 deg. Since the apex angle is reasonably small and no strong secondary forebody embedded shocks are present, the inviscid region, to a good approximation, should be predicted by the first modification approach. Hence, this type of body should offer the best conditions for possible wake correlation. The results are presented in Figure 23. It is apparent that the tow channel results (obtained using the stereo method of Section II) slightly underpredict the Mach number recovery in the viscous region. The worst correlation, however, is seen to exist in the vicinity of the recompression shock where the expanded flow has attained Mach number values in excess of freestream. The wind-tunnel results in this region exhibit a rapid Mach number increase with increasing lateral distance followed by a more gradual decline to the free-stream value. The tow channel results, on the other hand, exhibit a far more gradual increase in the same region with a subsequent decline toward the free stream value. The difference between the two in this region is primarily attributed to the physical difference between a shock wave and

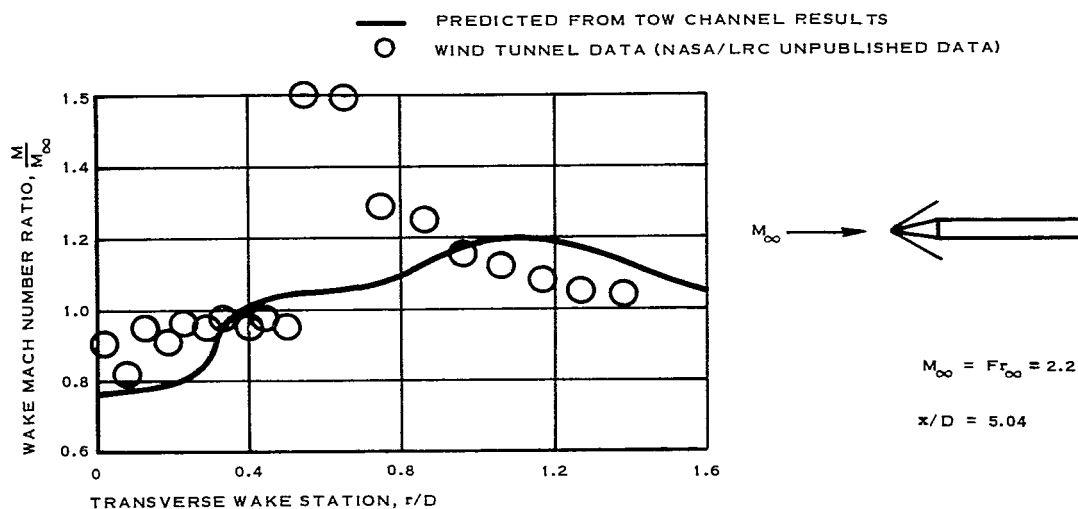


Figure 23 - Comparison of Experimental Two-Dimensional Wind-Tunnel and Tow-Channel Predicted Wake Results for Wedge-Block Forebody

a hydraulic jump. A shock wave is, of course, a near-discontinuity while the hydraulic jump, as stated in Section II, is a more gradual process.

In connection with the results of Figure 23, it is important to point out that the Reynolds numbers were not equal, although, in both the water and air, it is believed that the viscous wakes were turbulent.

Comparable wind-tunnel data for the 120-deg wedge and the blunted wedge-cylinder-flare was not available and, to indicate the degree of correlation with these bodies, it was necessary to resort to the use of the wake solution of Section III. The comparative data is provided in Figure 24 where a wake axial station of 5 was arbitrarily selected for both cases. To obtain theoretical wake profiles, corresponding shock shapes from the tow channel were used.

In general, it can be observed that the profile forms between the theoretical and water results are not in good agreement. In the vicinity of the viscous wake, the theory is regarded to be more indicative of the actual case since the two-dimensional viscous wake is comparatively thin (as compared to the axisymmetric case).

In the vicinity of the recompression shock, the water results again reflect a gradual flow expansion process which is not typical of a gas. In this region, the theory is also currently inadequate.

As pointed out in Item 3, below, this is not considered particularly restrictive to the theory's application in the prediction of decelerator flow fields.

e. Correlation of Detached Air and Water Bow-Wave Shapes

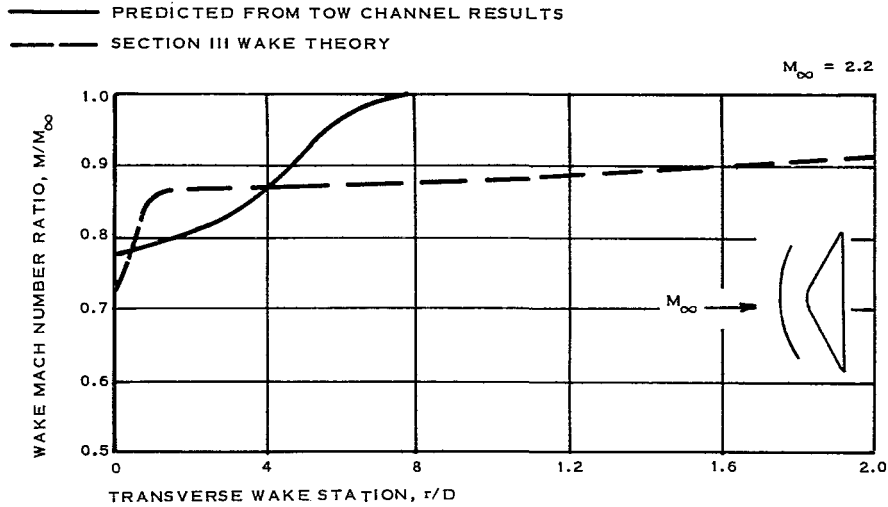
(1) General

As indicated earlier, a study was made to determine if three-dimensional air shock shapes could be predicted from tow channel results for analogous two- and three-dimensional bodies. The results of this study are encouraging in that extremely good results were obtained for a limited number of cases by a relatively simple method. In addition, the method can apparently be extended to predict shock shapes for two-dimensional bodies at angle-of-attack values or for bodies of a more complex geometry.

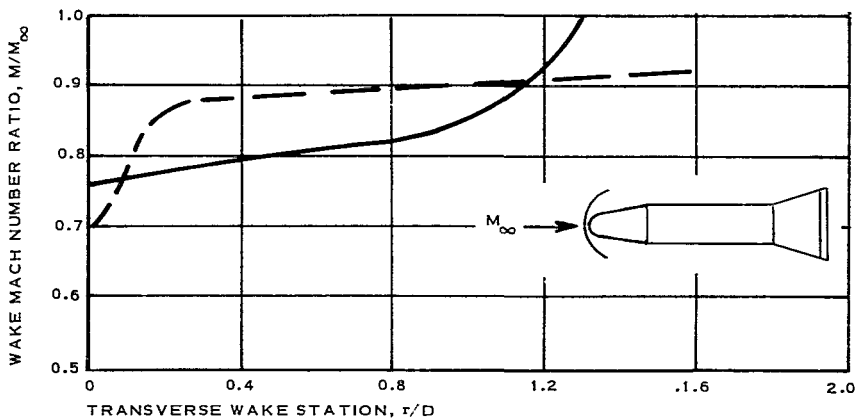
A simple approximate theory for predicting both standoff distance and shock wave shape in two-dimensional or axisymmetric flow was used to provide a means of correlating the water data with three-dimensional air results. Consequently, while the theory provided a means of correlation, the data from the tow channel was in turn used to help empirically correct some of the deficiencies of the theory.

(2) Development of Correlation Method

A method for predicting shock shapes about supersonic bodies of various



A - BLUNTED 120-DEG WEDGE FOREBODY ($X/D = 5$)



B - BLUNTED WEDGE-BLOCK-FLARE FOREBODY ($X/D = 5$)

Figure 24 - Comparison of Theoretical and Tow-Channel-Predicted Wake Results

geometrical shapes was developed by W. E. Moeckel several years ago (Moeckel's continuity method). This method is discussed in detail in Reference 2 and some experimental wind tunnel data supporting this method is found in Reference 15. Moeckel's method is an approximate solution, based on a simplified form of continuity equation, which was developed to predict the form and location of shock waves ahead of two-dimensional and axisymmetric bodies. The two basic assumptions used to obtain this solution are that:

1. The form of the shock between its foremost point and its sonic point is adequately represented by a hyperbola which asymptotically approaches a free-stream Mach line
2. The sonic line between the shock and the body is straight and inclined at an angle that depends only on freestream Mach numbers

Under these assumptions, the location and shape of the shock wave become independent of the geometrical portion of the body ahead of the sonic point. The solution is thus a function only of Mach number and the location of the body sonic point. Mach number is a well defined parameter and, thus, only the body sonic point needs to be defined. Moeckel suggests two approximate techniques for locating the body sonic point.

1. For bodies having sharp or well defined shoulders, the sonic point is located at the shoulder.
2. For more gradually curved bodies, such as ogives, the shoulder is assumed to exist at the point where the contour of the body is inclined at the wedge angle or cone angle corresponding to shock detachment.

With the application of the above assumptions, the general form of a detached shock is given, in Reference 2, as

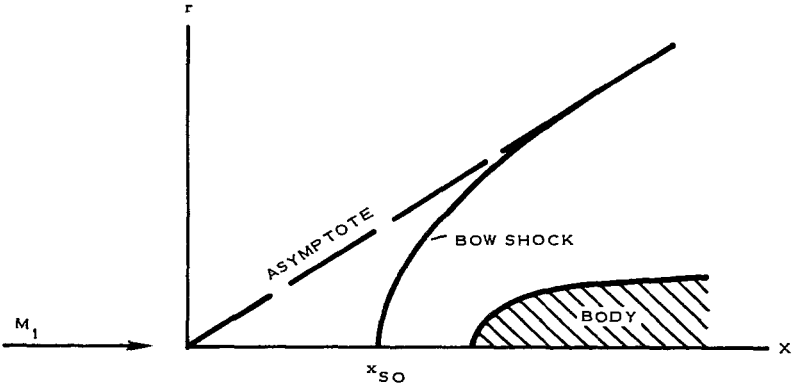
$$r_s = \frac{1}{\beta}(x_s - x_{s0})^{\frac{1}{2}} \quad (84)$$

where

$$\beta = (M_1^2 - 1)^{\frac{1}{2}}$$

The parameters r_s and x_s are, respectively, defined as the bow shock radial (or transverse) and axial coordinates. The parameter x_{s0} is distance

along the centerline ($r = 0$) between the asymptote and the foremost point on the bow shock (see sketch below).



The necessary relationships then are developed in Reference 15 to obtain bow shock shape and location satisfying the general form of Equation (84).

For comparing water flow shocks with predicted two-dimension gas results, no further correlation relationships are required. To facilitate the correlation with three-dimensional results, however, the following form equation for detached shocks also is used:

$$\frac{r_s}{L} = A \left(\frac{x_s}{L} \right)^n \tag{85}$$

where L is a characteristic body diameter and A and n are generally unknown constants, which must be determined.

For convenience, the maximum body diameter, D , is used as the characteristic length value. Therefore, Equation (85) becomes

$$\frac{r_s}{D} = A \left(\frac{x_s}{D} \right)^n \tag{86}$$

With the use of Moeckel's technique and Equation (86), the correlation is carried out as follows:

1. From water hydraulic jump shapes, appropriate values of constants A and n are determined for which agreement of results is achieved.
2. From Moeckel's theory predicted shock shape equations are obtained for the Step-1 bodies in a $\gamma = 2$ gas and a $\gamma = 1.4$ gas (air) and appropriate values of A and n are determined.

3. With the results of Steps 1 and 2 the modified values of A and n are predicted for two-dimensional air.
4. A similar procedure is applied to convert to three-dimension air results, using Moeckel's three-dimensional air prediction theory and the results of Step 3.

Steps 1 through 4 can be clarified and summarized by the following expressions:

$$\frac{z_1}{z_2} = \frac{z_3}{z_4} \quad (87)$$

and

$$\frac{z_5}{z_1} = \frac{z_6}{z_2} \quad (88)$$

where z denotes values of A or n, and the subscripts denote conditions as follows:

- 1 - two-dimensional air, modified results
- 2 - two-dimensional air, Moeckel's theory
- 3 - experimental water values
- 4 - two-dimensional gas ($\gamma = 2$), Moeckel's theory
- 5 - three-dimensional air, modified results
- 6 - three-dimensional air, Moeckel's theory

For axisymmetric bodies corresponding to the water test bodies, the appropriate shock shape relation now becomes

$$\frac{r_s}{D} = A_5 \left(\frac{x}{D} \right)^{n_5}, \quad (89)$$

where the dummy constant, z_5 , of Equation (89), is replaced by the actual denoted values of A and n.

The relationship, represented by Equation (89), is now completely defined.

(3) Comparison and Correlation Results

(a) Comparison of Water-Gas Two-Dimensional Bow Waves

Comparisons between Moeckel's predicted theory and actual tow channel results were carried out for a number of configurations. Some representative ones are summarized in Table IV. Table IV also contains the "A" and "n" values obtained from the tow channel hydraulic jump results. These values are given since the shocks from some of these configurations will be later used in the prediction of the three-dimensional shapes.

TABLE IV - TOW CHANNEL CONFIGURATIONS AND
ASSOCIATED HYDRAULIC JUMP PARAMETERS

Configuration	Fr_{∞}	Number of tests used	A	n
Circular cylinders	1.5	3	3.30	0.639
			3.40	0.555
			3.40	0.601
Circular cylinders	2.0	3	2.25	0.524
			2.35	0.484
			2.30	0.644
120-deg blunted wedge	2.0	3	2.76	0.481
			2.67	0.640
120-deg blunted wedge	2.2	3	2.51	0.476
			2.49	0.553
			2.50	0.509
Circular cylinder	2.5	3	2.17	0.557
			2.10	0.566
			2.04	0.598
120-deg blunted cones	2.5	2	2.30	0.546
			2.25	0.612

Figures 25 through 30 indicate the results of comparing the water jump shapes with predicted two-dimensional gas results. In general, the experimental water values define profiles which lie between the two predicted gas results and do not match either predicted shape. It must be

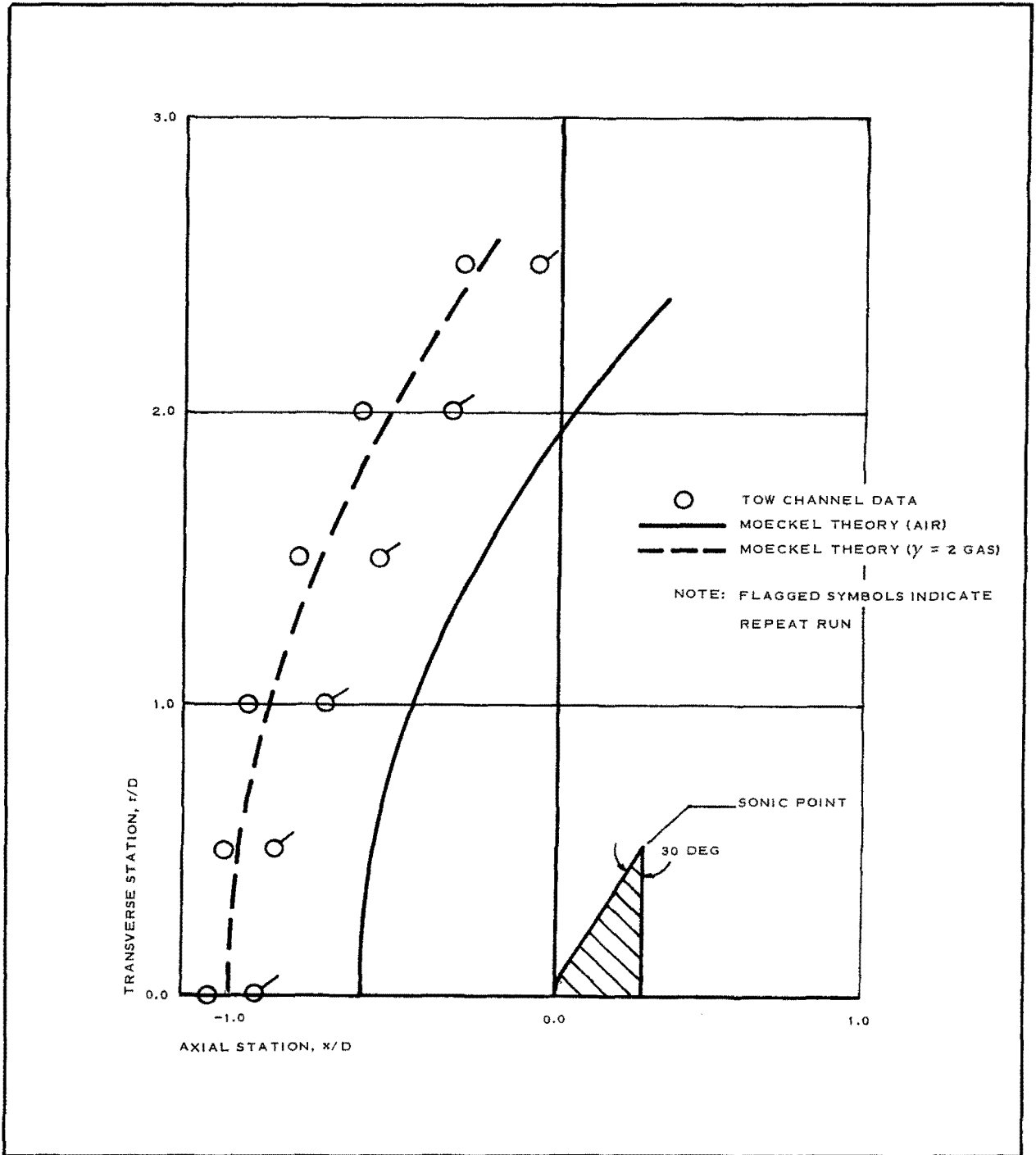


Figure 25 - Tow-Channel Shock Shapes for 120-Deg Blunted Wedge at $M_\infty = 2.0$

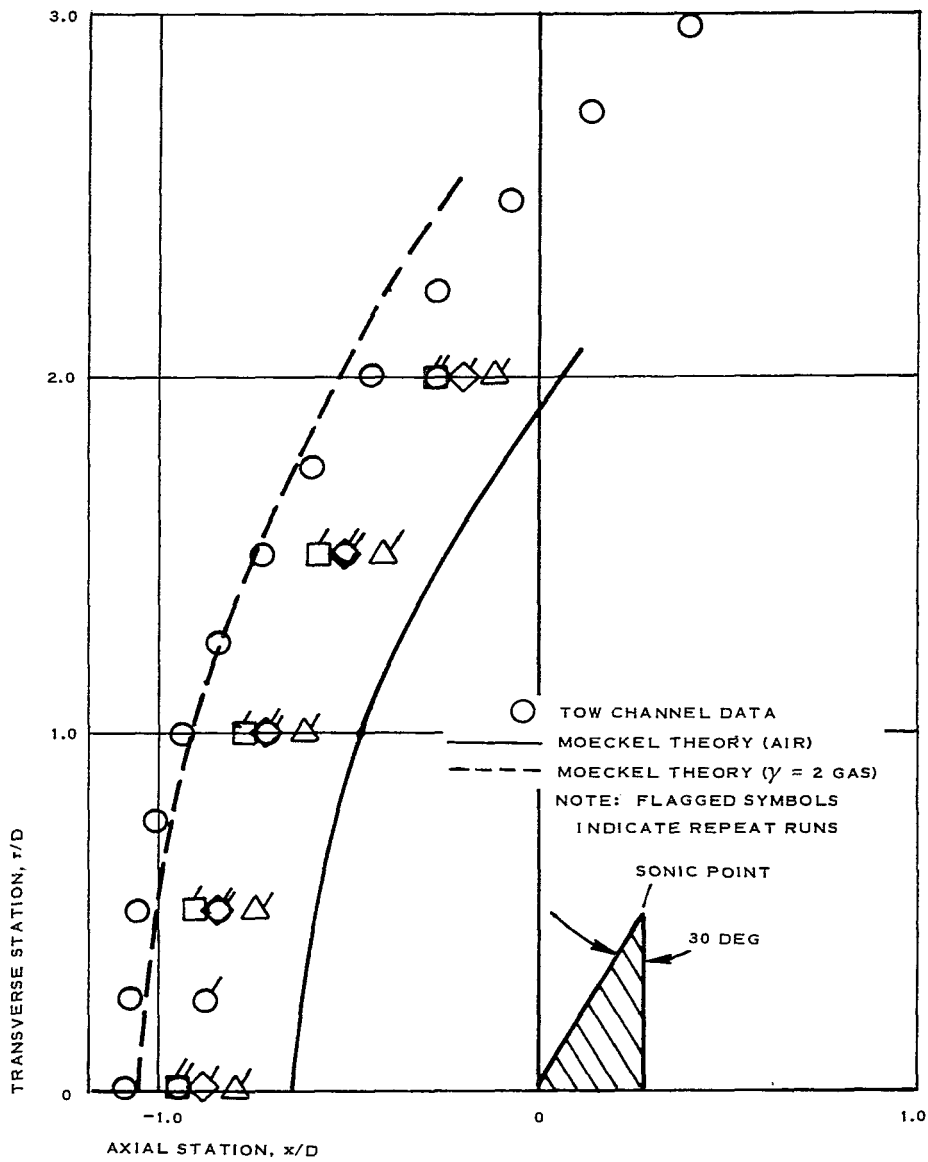


Figure 26 - Tow-Channel Shock Shapes for 120-Deg Blunted Wedge at $M_\infty = 2.2$

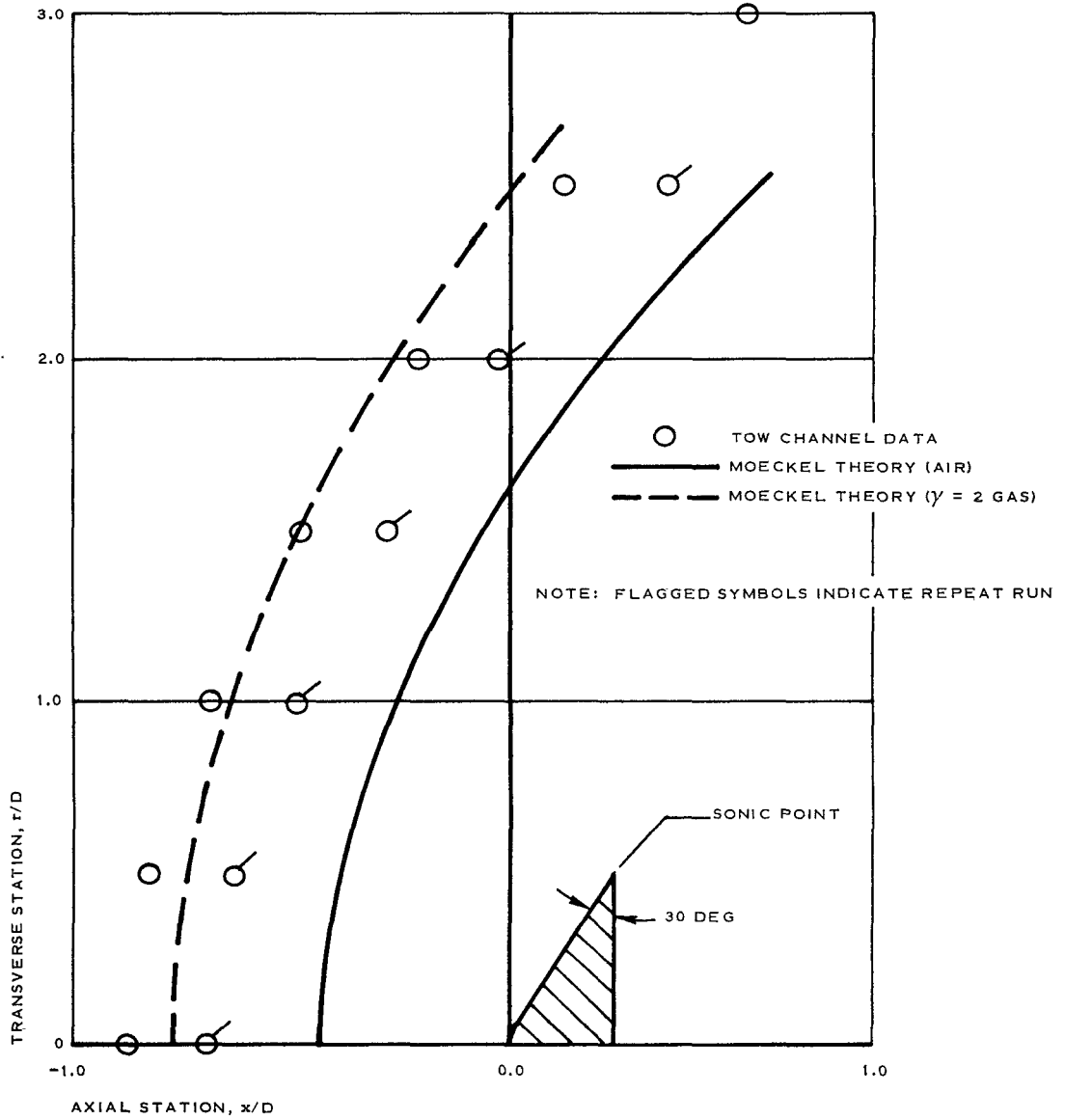


Figure 27 - Tow-Channel Shock Shapes for 120-Deg Blunted Wedge at $M_\infty = 2.5$

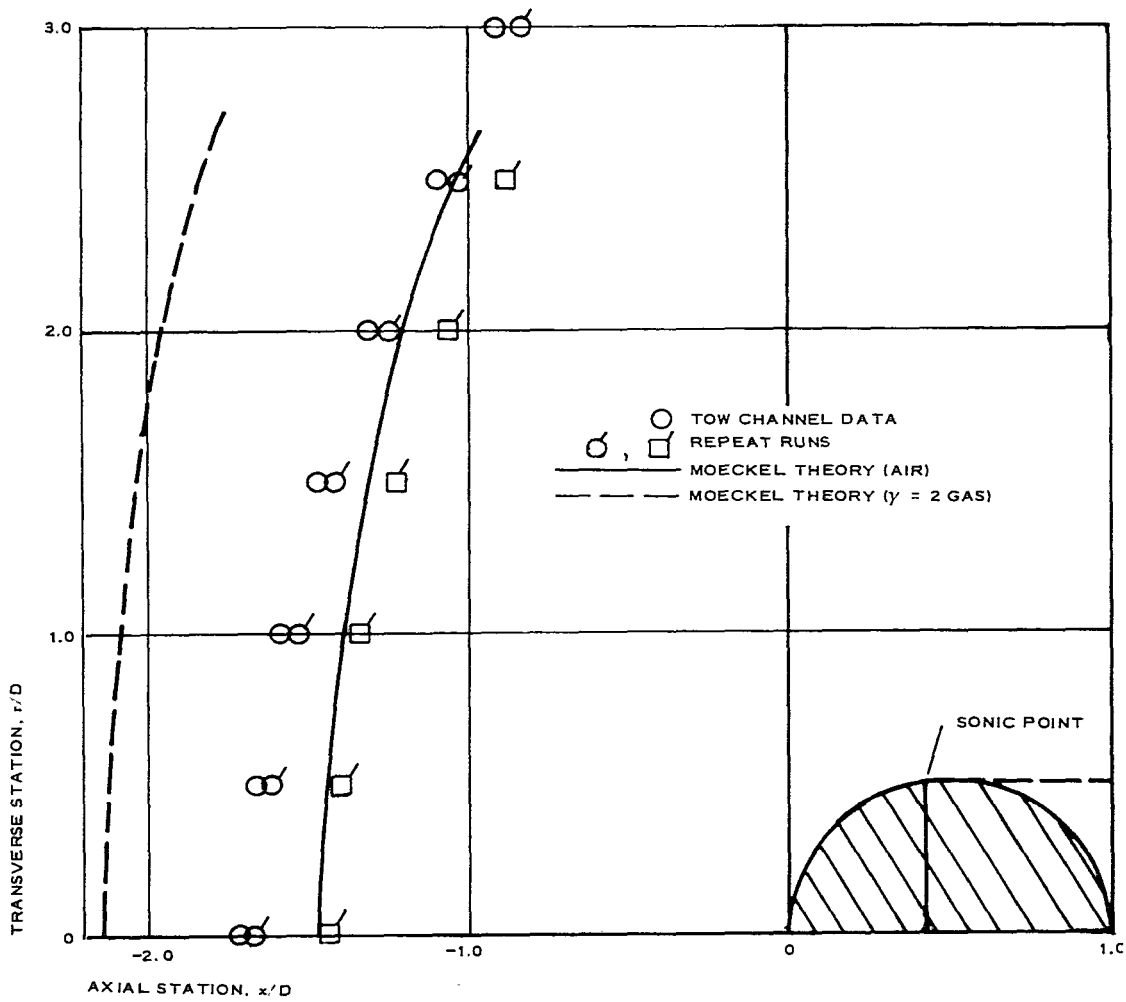


Figure 28 - Tow-Channel Shock Shapes for Circular Cylinders at $M_\infty = 1.5$

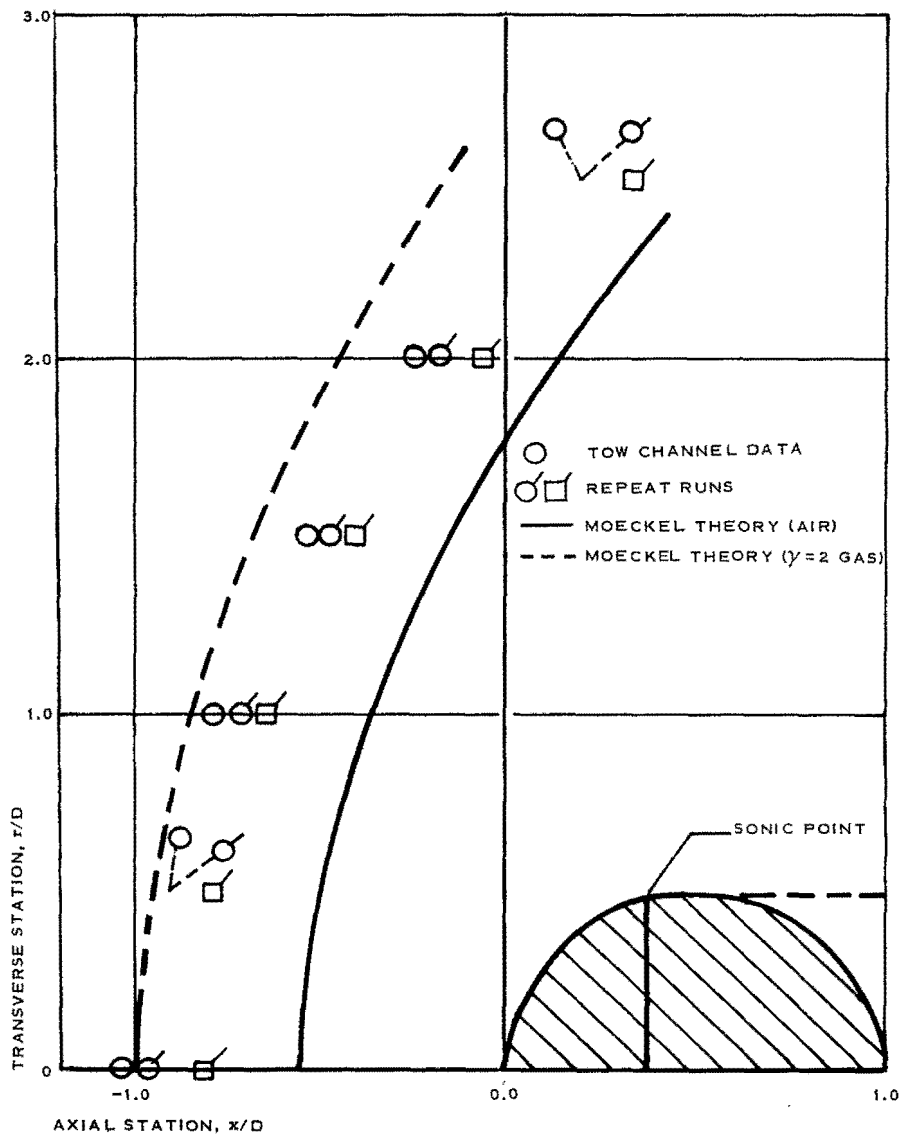


Figure 29 - Tow-Channel Shock Shapes for Circular Cylinders at $M_{\infty} = 2.0$

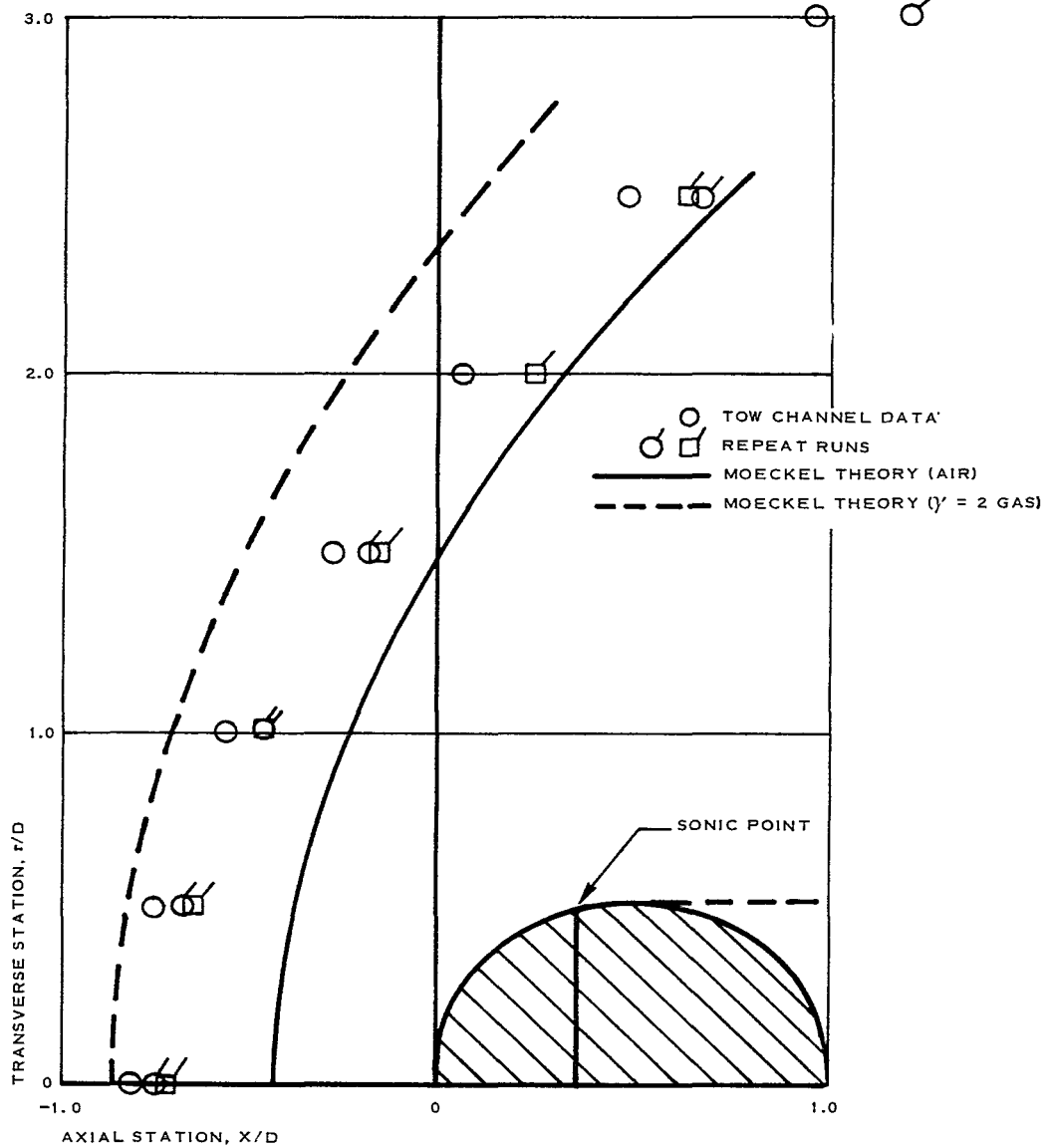


Figure 30 - Tow-Channel Shock Shapes for Circular Cylinders at $M_\infty = 2.5$

remembered here, however, that Moeckel's method is only an approximate one and the differences do not necessarily indicate the water results to be in error. The inconsistent trend in standoff distance, as well as the often rather large discrepancies in the predicted and observed values, does, however, suggest that the hydraulic jump location may not be truly representative of the shock wave location in a $\gamma = 2$ gas.

(b) Correlation with Three-Dimensional Results

Results obtained for the three-dimensional case are presented in Tables V and VI and Figures 28 through 32 for the test bodies indicated. The data presented in Tables V and VI are those required to predict the three-dimensional shock shapes as outlined in Item 2, e, (2), above.

TABLE V - EXPERIMENTAL WATER
VALUES OF A AND n FOR SHOCK
SHAPE RELATIONS

Configuration	M_{∞}	A (average)	n (average)
120-deg cone	2.2	2.5	0.512
Sphere	2.0	2.3	0.504
Flat plate	2.2	2.2	0.505

Results of Figures 31 through 33 show the agreement with actual schlieren shock shapes to be very good. It is noted that the actual and predicted results for the 120-deg cone and the flat plate are at slightly different Mach numbers. The difference of $\Delta M = 0.01$ is not considered significant, however.

The results of Figures 31 through 33 should not be interpreted as implying any correlation with respect to standoff distance. In fact, as mentioned in Item 2, e, (3), the standoff distances between the predicted and actual results might be expected to differ. This, however, does not impose limitations on the wake calculation procedure presented in Section III, and, for many other problems of practical interest, is not significant. A common origin was selected to show the good agreement with respect to the shape itself.

For the two-dimensional case, the results can be extended to enable the prediction of bow shock geometry when the body is at a given angle of attack. Moeckel's method for the angle-of-attack case is outlined in Reference 1. Basically, it involves separating the entire flow field into two separate regions with the zero streamline (i. e., the streamline that

TABLE VI - THEORETICAL VALUES OF A AND
n FOR SHOCK SHAPE RELATIONS

Gas results	M_∞	Two-dimensional values		Three-dimensional values	
		A	n	A	n
$\gamma = 1.4$ (air)	1.5	3.83	0.521	2.39	0.548
	2.0	2.58	0.519	1.95	0.528
	2.2	2.41	0.515	1.89	0.535
	2.5	2.27	0.515	1.85	0.518
$\gamma = 2.0$	1.5	4.44	0.515	NR*	NR
	2.0	2.98	0.512	NR	NR
	2.2	2.77	0.512	NR	NR
	2.5	2.58	0.514	NR	NR

*Not required

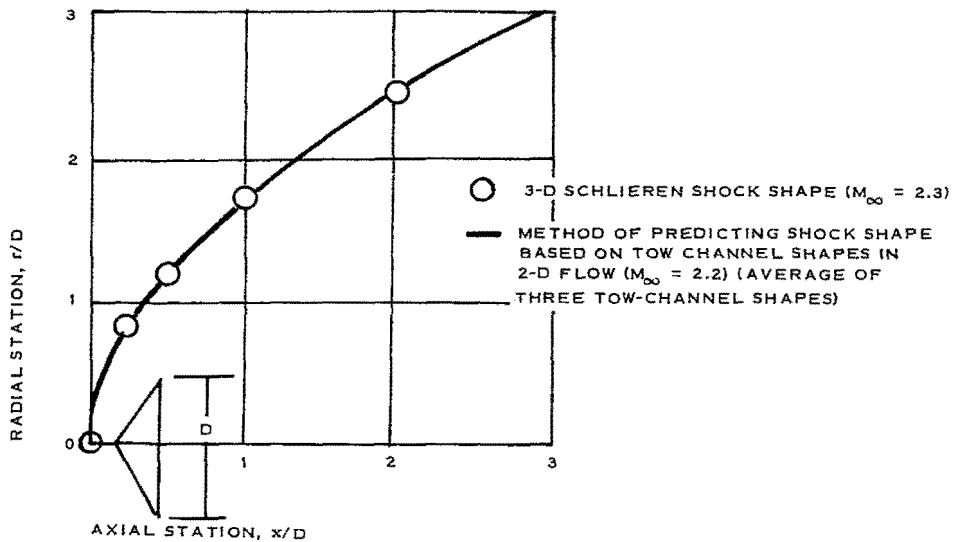


Figure 31 - Actual and Predicted Three-Dimensional Air Shock Shapes for a 120-Deg Blunted Cone

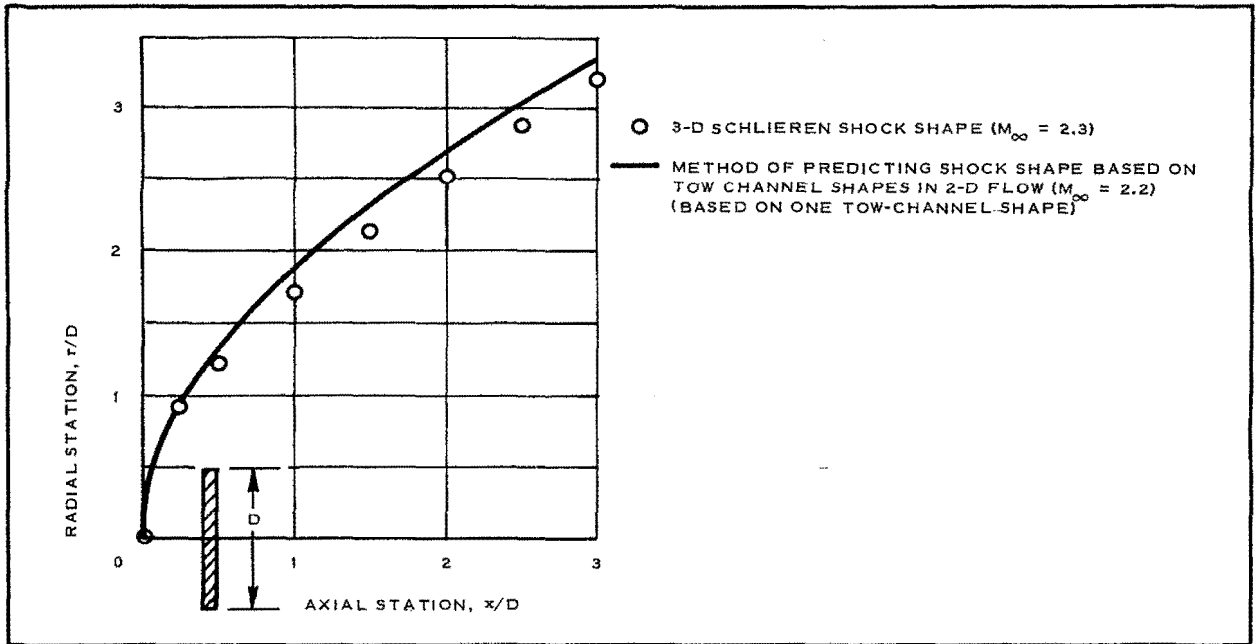


Figure 32 - Actual and Predicted Three-Dimensional Air Shock Shapes for a Flat Plate

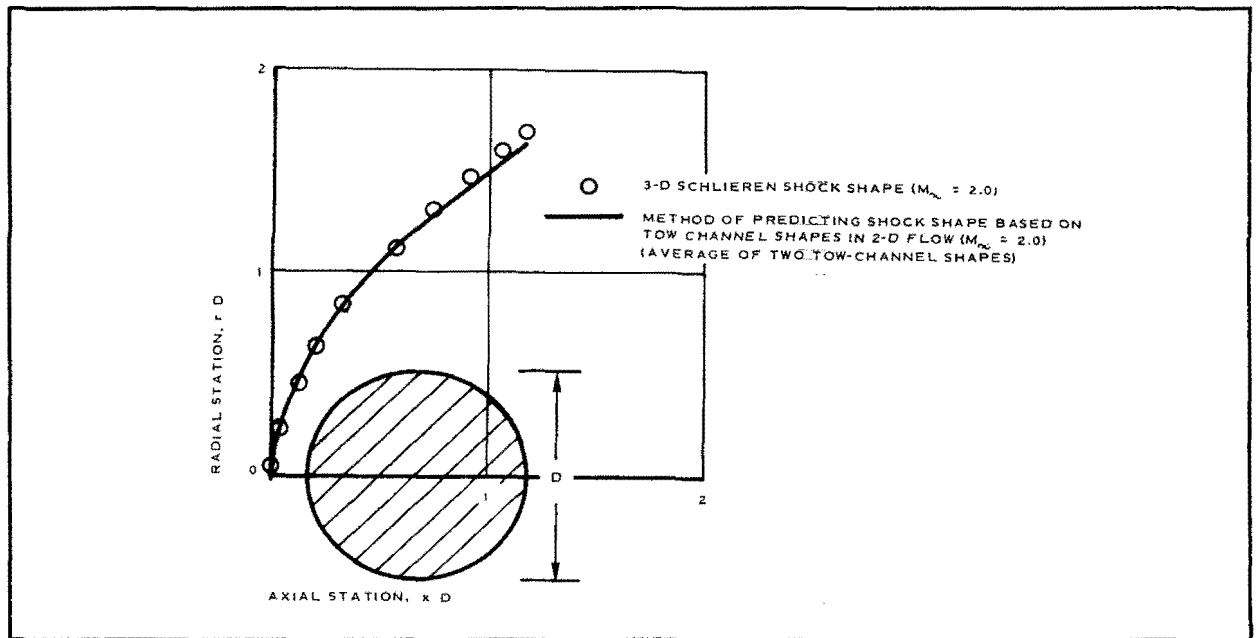


Figure 33 - Actual and Predicted Three-Dimensional Air Shock Shapes for a Sphere

reaches stagnation) being the dividing line between the two regions. The shock shape in each region then can be predicted independently. These results then would be used to modify appropriate tow channel data.

3. COMPARISON OF EXPERIMENTAL AND THEORETICAL WAKE RESULTS

a. General

Viscous and inviscid high-speed compressible wake profiles are compared in the following discussion for both two-dimensional and three-dimensional (axisymmetric) flow. The theoretical method used is based on the developments and results of Section III. Experimental values were calculated from NASA wind-tunnel data, 16, 17, 18 and from two-dimensional test data obtained by NASA for this program. Three basic body configurations are considered because applicable wind-tunnel data was available and because they are considered representative of a broad class of body configurations.

b. Comparison of Two- and Three-Dimensional Profiles

Reasonable agreement has been obtained in comparing cone-cylinder wind-tunnel data with viscous wake calculations using viscosity Model 4, a turbulent viscosity constant, K of 0.02, and a neck location of $x/D = 2$. This is shown in Figures 34 through 38 which compare pitot pressure profiles for x/D 's of 2.52, 5.04, and 7.56. As may be seen, the center-line value and the general form of the profile are both predicted quite well. However, there is a discrepancy in the actual width of the viscous wake for the case of the lower free-stream Mach number ($M_\infty = 2.3$). This possibly is due to the assumption of $Pr = 1$ in the viscous wake solution which affects not only the temperature profile but also the density profile and to some extent the predicted wake growth.

The wedge-block data shown in Figures 39 through 41 were obtained for the two-dimensional counterpart of the cone-cylinder discussed above. Non-dimensional two- and three-dimensional Mach number profiles are shown at x/D 's of 2.52 and 5.04 and at an x/D of 7.56 for the axisymmetric cases (two-dimensional data not available). Also shown are the corresponding calculated wake profiles for the same wake viscosity model as in Figure 33. Again, reasonable agreement is seen to exist with the two-dimensional data and viscous wake calculations being in better agreement than the data and calculations for the three-dimensional cone cylinder. This is believed to be due to a greater sensitivity of the three-dimensional calculations to any assumptions concerning the flow Prandtl number. The two-dimensional viscous wake also is seen to be considerably thinner than that behind the cone cylinder.

The high Mach numbers observed outside of the viscous wake region for the two-dimensional case are due to the over-expansion of the flow in the near wake region of the body giving rise to pressures lower than and Mach

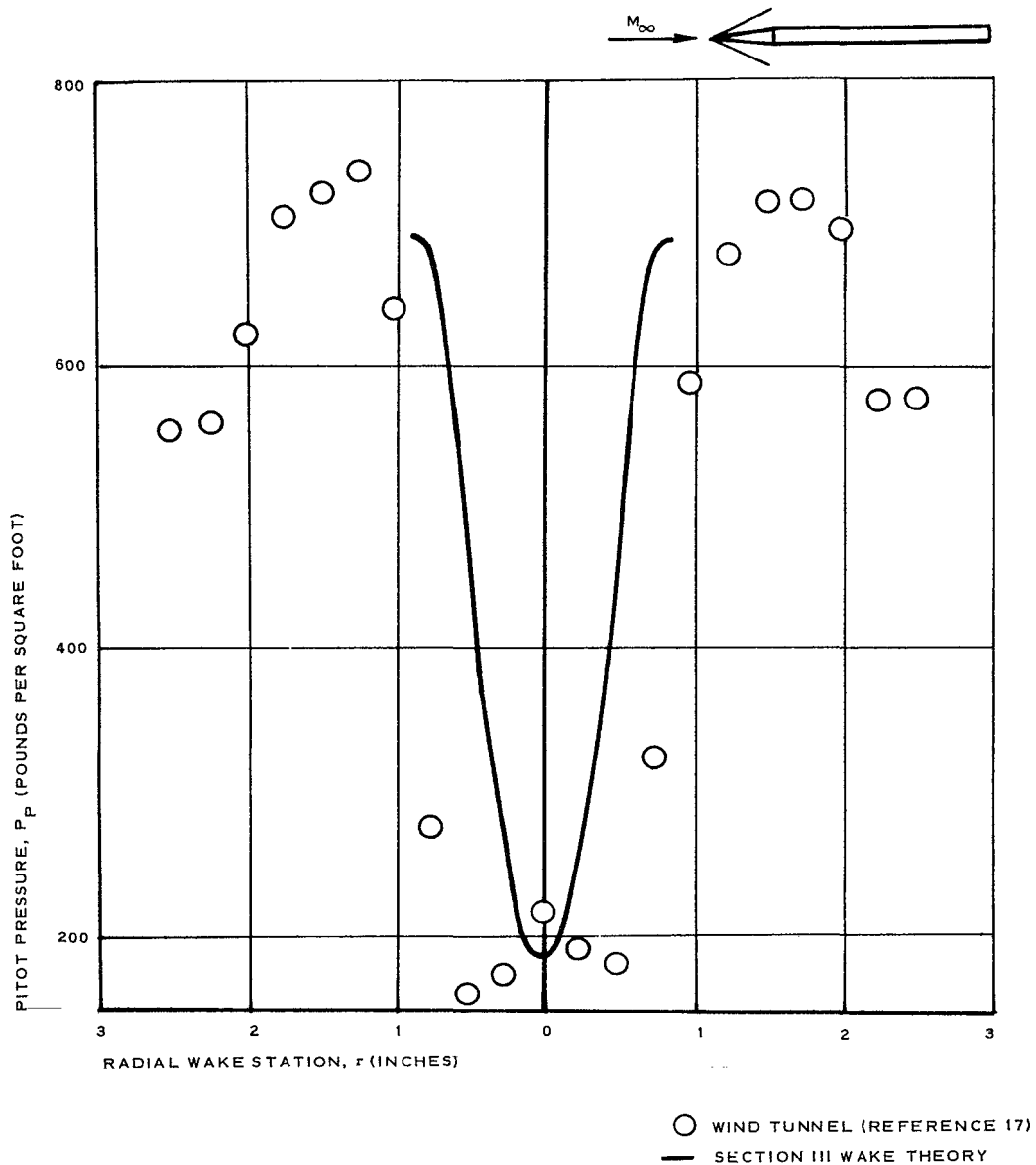


Figure 34 - Cone-Cylinder Wake Pitot Pressure Profiles at $x/D = 2.52$ ($M_\infty = 2.3$)

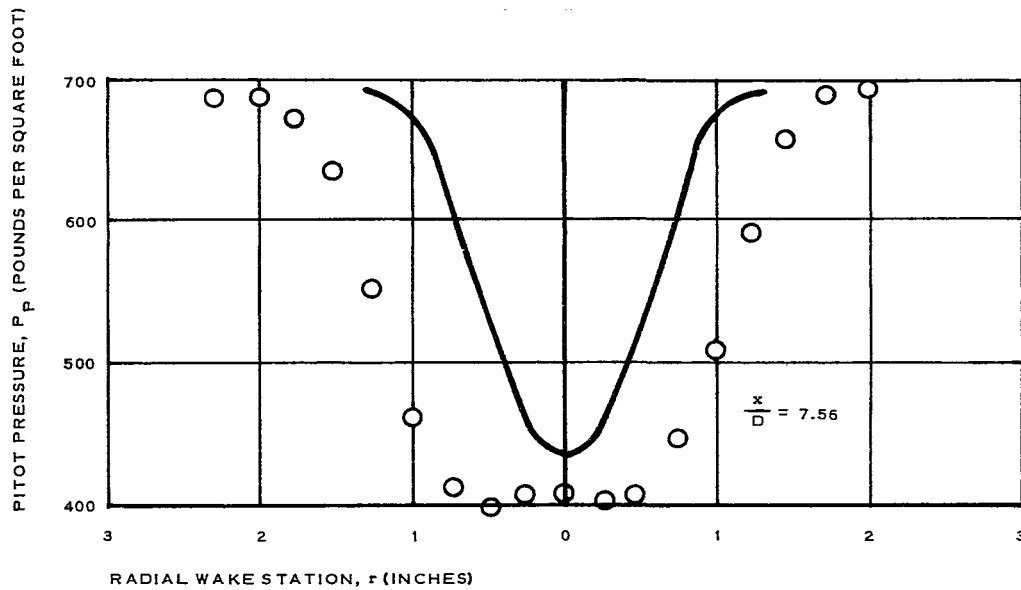
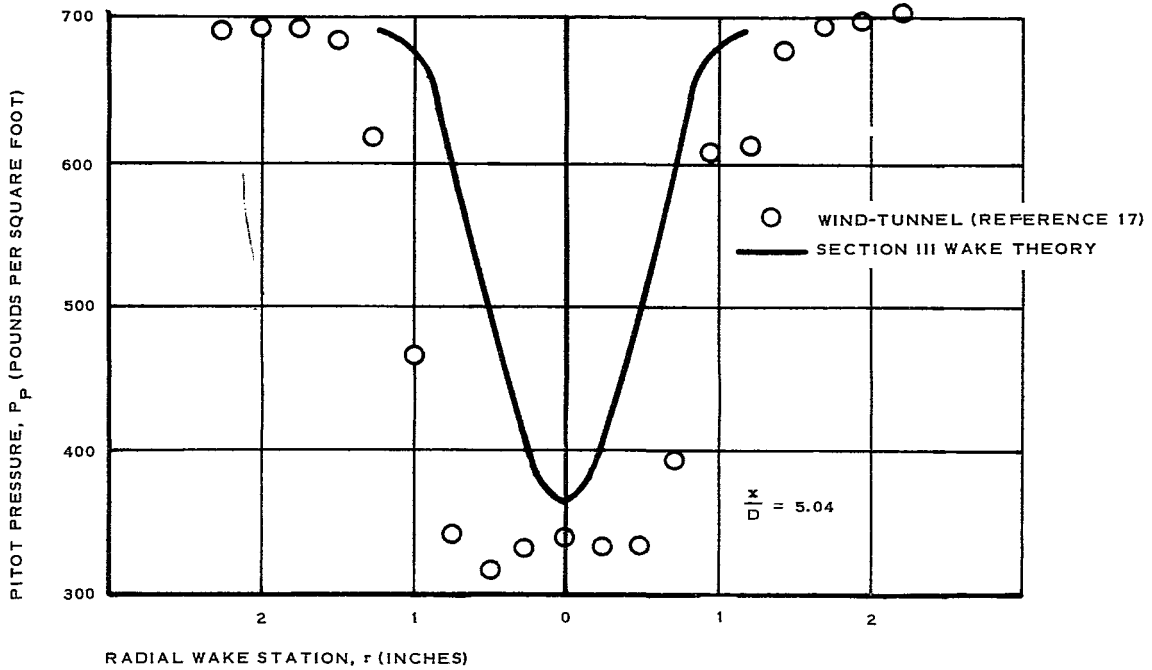
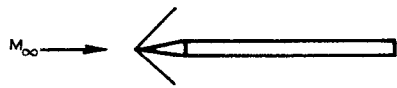


Figure 35 - Cone-Cylinder Wake Pitot Pressure Profiles at $x/D = 5.04$ and $x/D = 7.56$ ($M_\infty = 2.3$)



○ WIND-TUNNEL (REFERENCE 17)
 — WAKE THEORY (SECTION III)

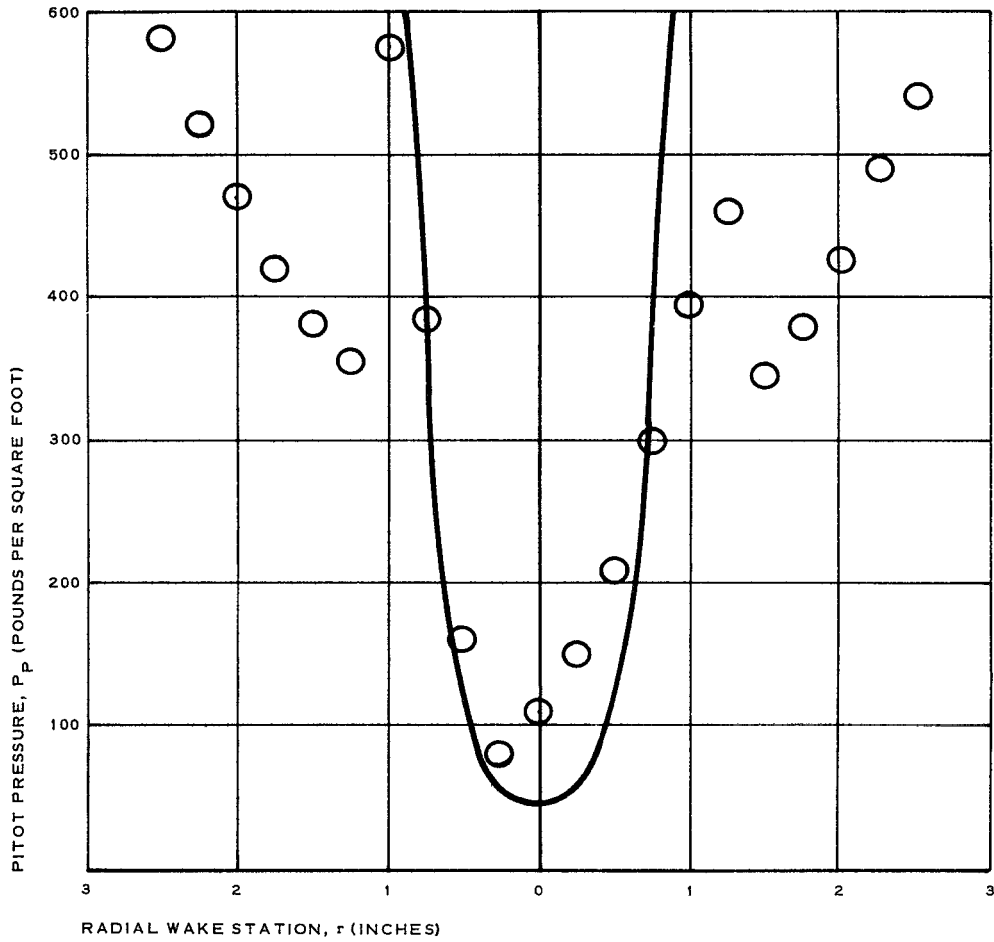


Figure 36 - Cone-Cylinder Wake Pitot Pressure Profiles at $x/D = 2.52$ ($M_\infty = 4.65$)

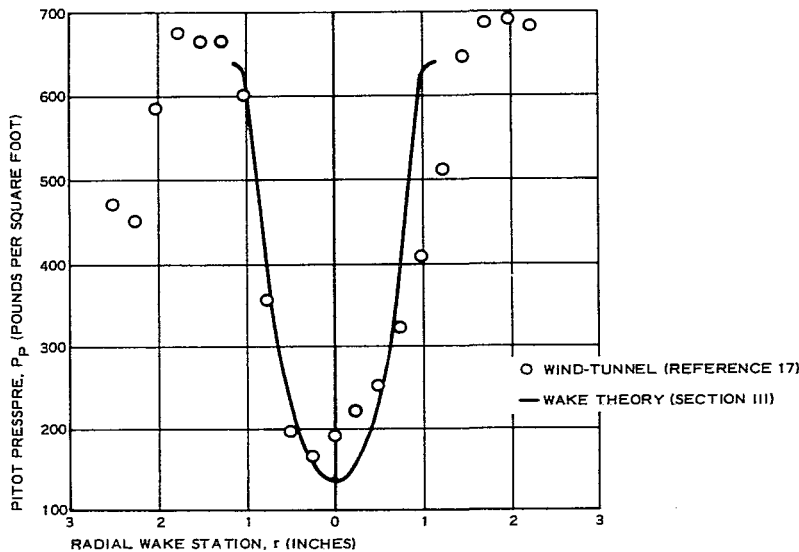


Figure 37 - Cone-Cylinder Wake Pitot Pressure Profiles at $x/D = 5.04$ ($M_{\infty} = 4.65$)

numbers higher than their corresponding free stream values. Across the recompression shock, the pressure increases and the Mach number decreases with both values approaching their free stream values. For example, at an x/D of 5.04, the recompression shock for the two-dimensional model is located at approximately $r/D = 0.5$. This is shown by the static pressure profiles in Figure 42. Thus, for $r/D < 0.5$ and outside of the viscous wake region, $M_L \cong M_{\infty}$; while for $r/D > 0.5$, $M_L \geq M_{\infty}$. In the cone-cylinder case, the viscous wake is thicker, the over-expansion is not as great, and the recompression shock wave, thus, should be weaker and pushed out further into the flow as may be seen in Figures 36, 37, and 38. This recompression shock is also apparent in the pitot pressure profiles shown in Figures 34 and 35. At larger x/D 's the recompression shock is not observable in the data and appears to reside outside of the region surveyed. The wake neck location need not be the same for the two- and three-dimensional cases; more information is needed on this feature of the flow. Also, the presence of a recompression shock wave is not currently accounted for in the wake calculation procedure.

As a practical matter, this last statement is not considered to imply any serious deficiency in the present inviscid wake solution. This is because the wake solution is considered to provide a means for calculating flow fields about trailing decelerators which, in general, operate behind

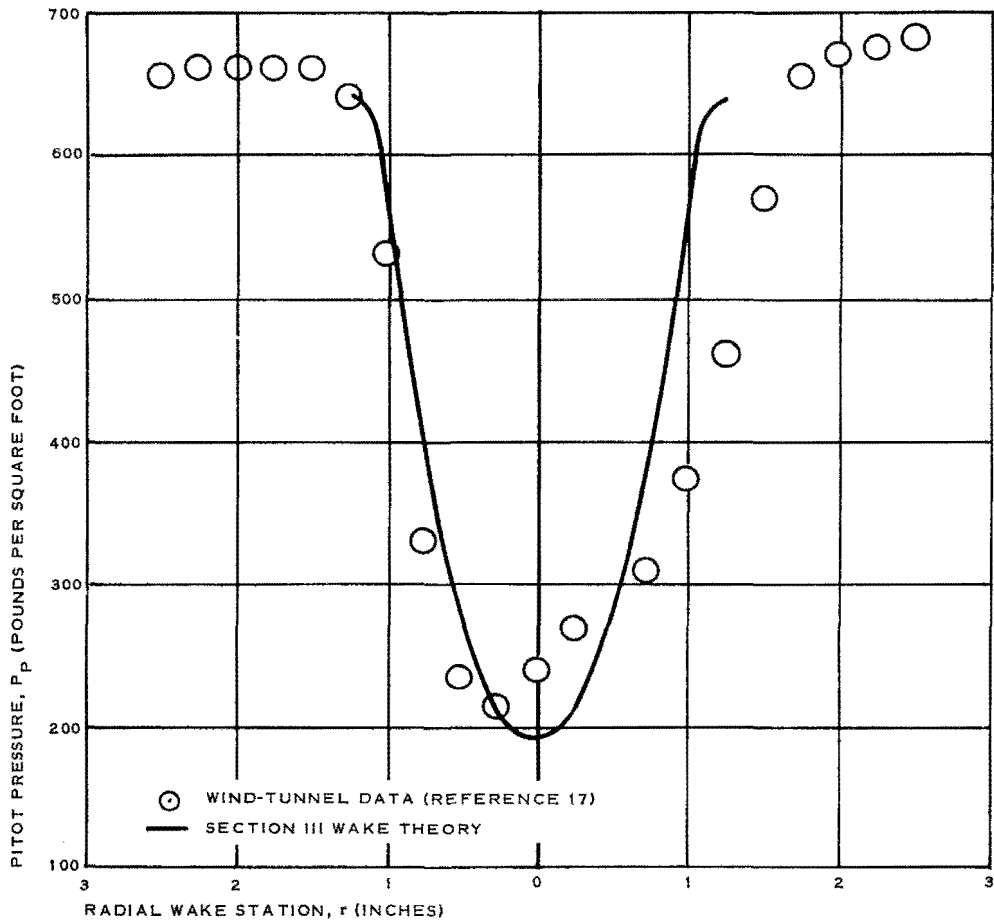


Figure 38 - Cone-Cylinder Wake Pitot Pressure Profiles at $x/D = 7.56$ ($M_\infty = 4.65$)

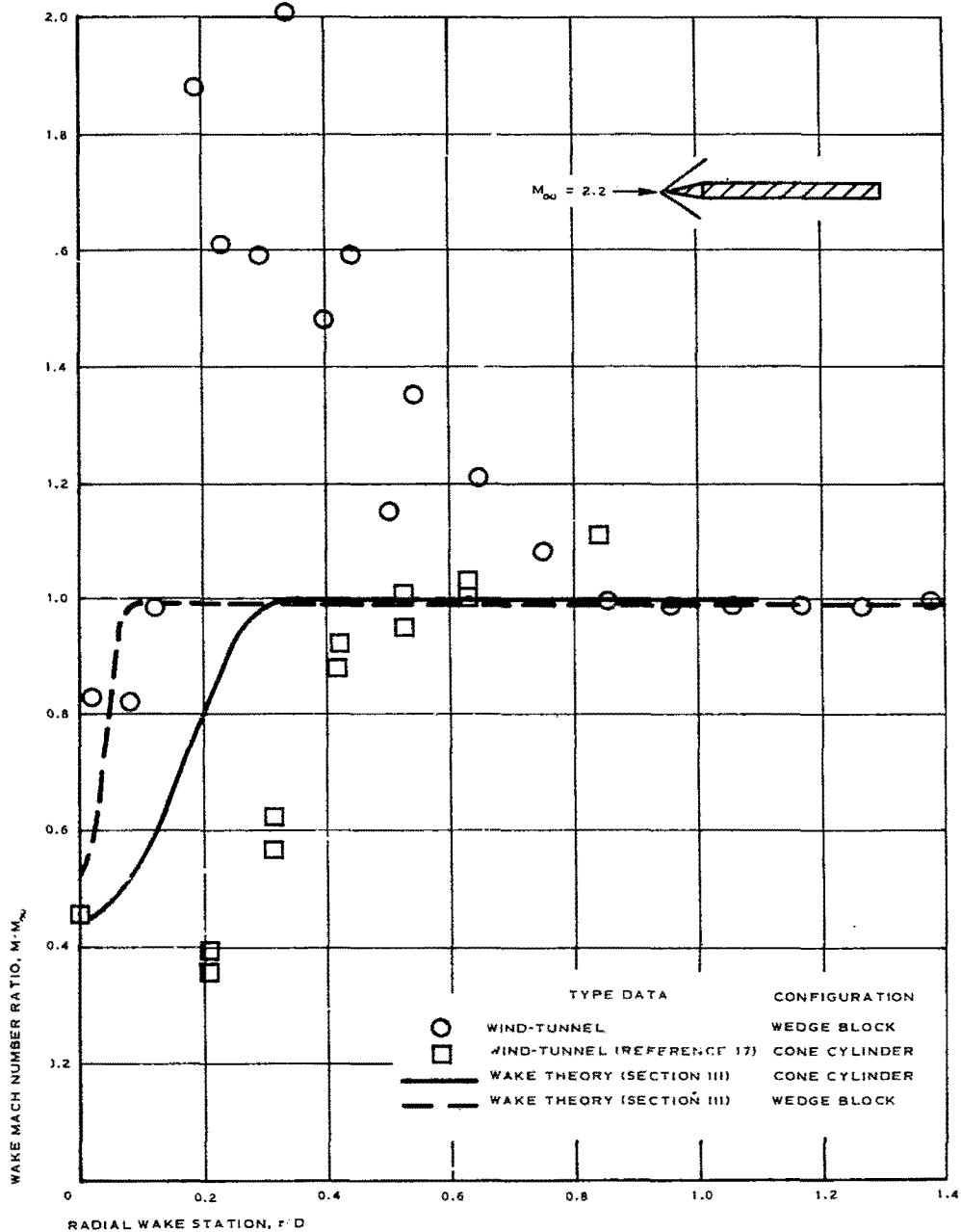


Figure 39 - Wake Mach Number Profiles for Cone Cylinder and Wedge Block at $x/D = 2.52$

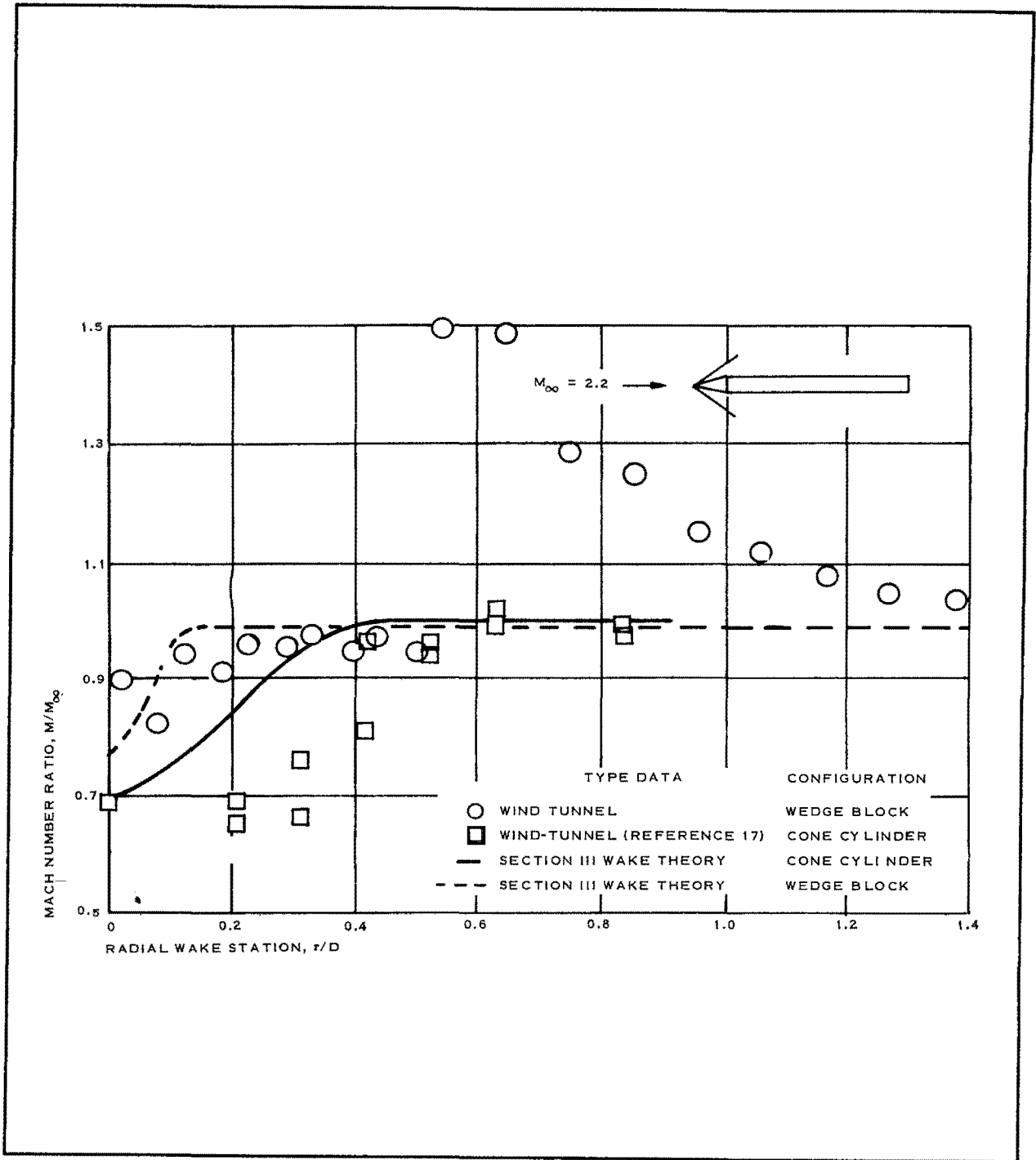


Figure 40 - Wake Mach Number Profiles for Cone Cylinder and Wedge Block at $x/D = 5.04$

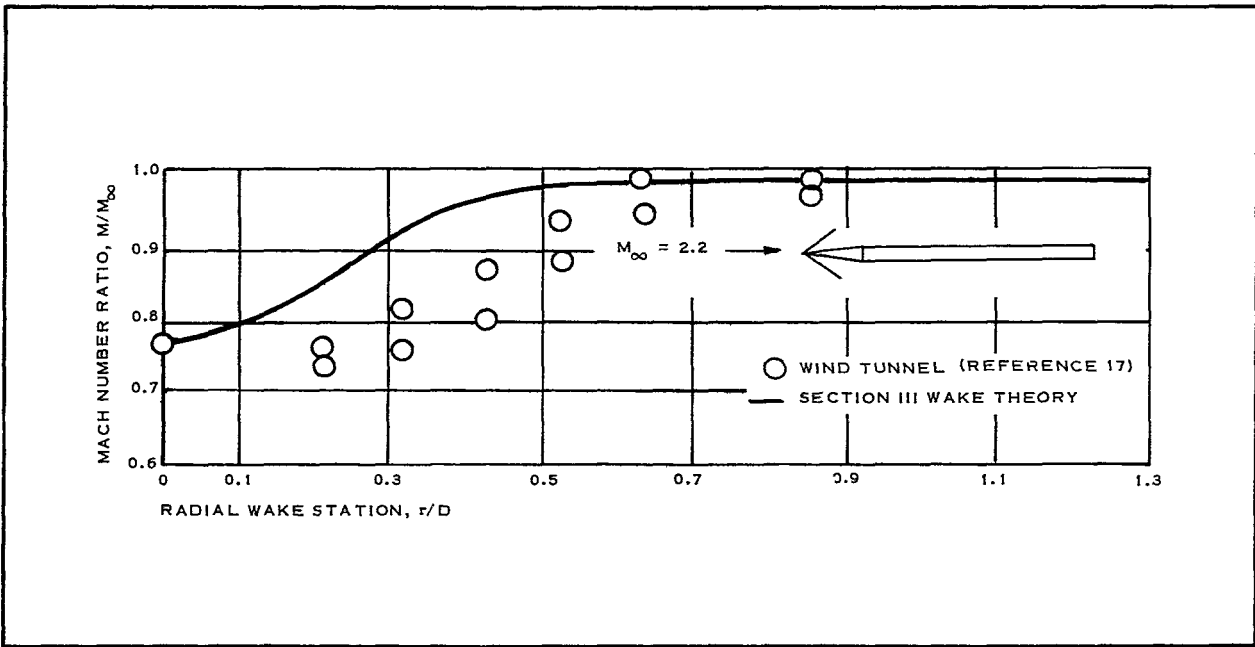


Figure 41 - Wake Mach Number Profiles for Cone Cylinder at $x/D = 7.52$

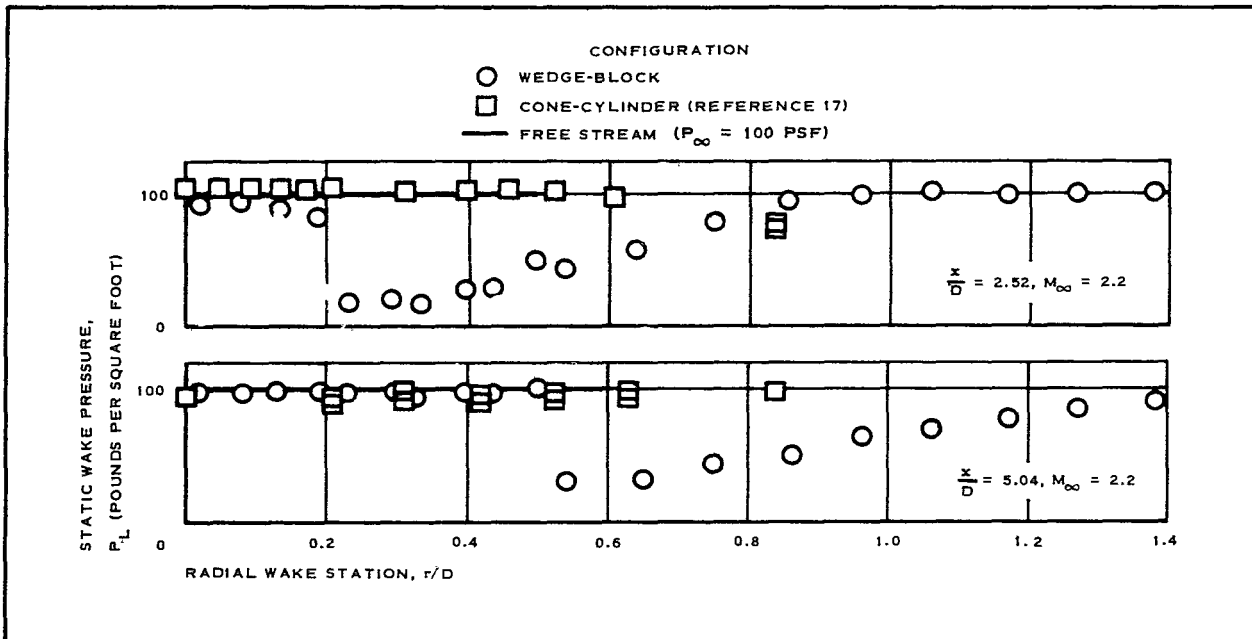
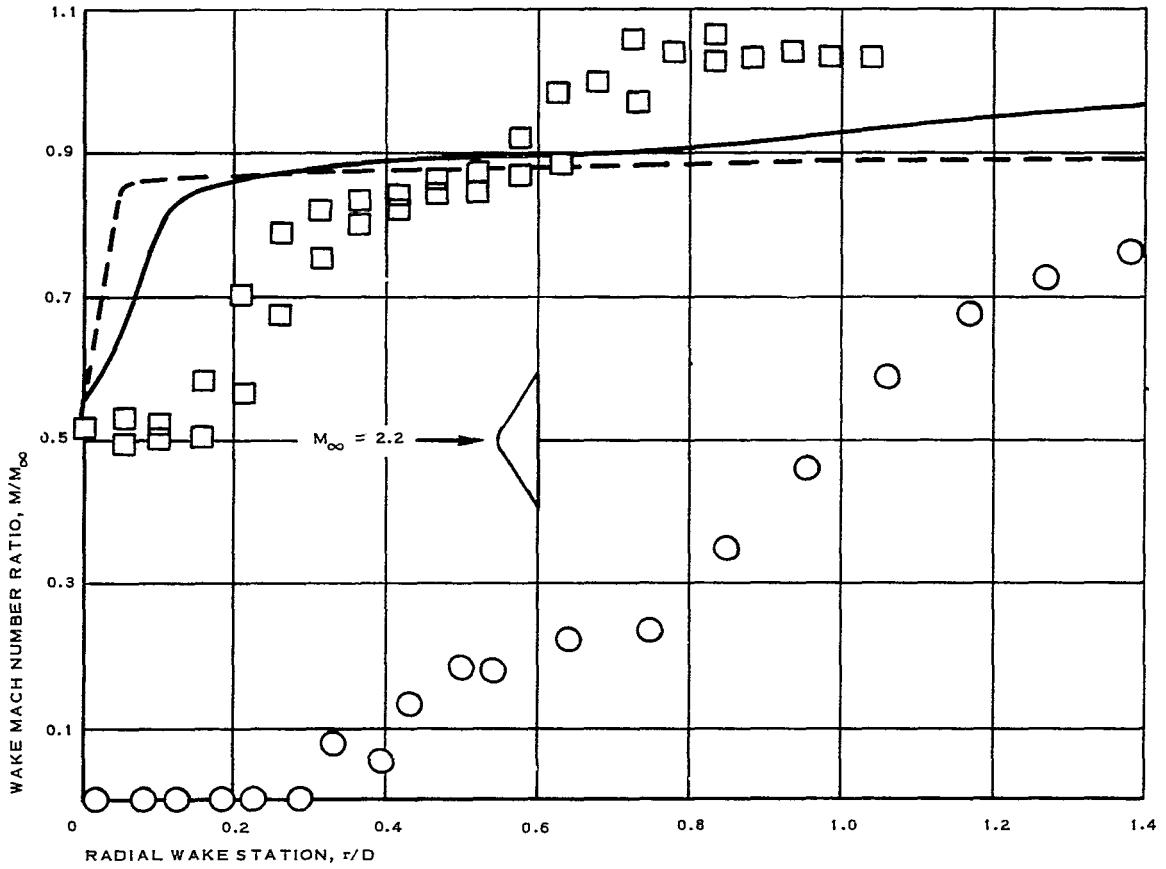


Figure 42 - Measured Local Wake Static Pressure for Cone Cylinder and Wedge Block

the recompression shock and, therefore, down stream of the over-expansion region. In situations where this is not the case, the decelerator itself would alter the wake so that, at least, the recompression shock would coalesce with the decelerator's bow shock and, thus, affect its shape. Consequently, considering the assumed application, the current inviscid wake theory is considered adequate in this respect.

Non-dimensional Mach number profiles for the wake of a 120-deg cone and 120-deg wedge are shown in Figures 43 through 45 for x/D 's of 2.5, 5.0, and 8.33. Also shown here are calculated profiles based on viscous wake model 4, a K of 0.02, and a wake neck location of $x/D = 2$. Here also, approximate agreement between the 120-deg cone data and the calculations exists. This agreement is particularly good at the x/D of 8.33; however, even at an x/D of 5.0 the agreement is quite satisfactory. Here, the major difference between the data and the calculations is due to the wake static pressures which in the calculation is assumed to be equal to the free stream pressure, but experimentally has been shown to be approximately 25 percent above free stream. This higher pressure would result in a lower Mach number. A spot check of this figure indicates that correcting for the static pressure in Figure 44 would bring the calculated curve in agreement with the data. Only at an x/D of 2.5 is the agreement somewhat unsatisfactory for the 120-deg cone. This is, however, understandable since the wake calculation procedure is less applicable to the near wake region. Furthermore, it is possible that for the near wake region in the proximity of the pressure rake to the wake neck may unduly influence the wake characteristics.

Measurements of wake characteristics behind a 120-deg wedge, the two-dimensional counterpart of the previously-discussed 120-deg cone, are also shown in Figures 43 and 44. These are for x/D 's of 2.5 and 5.0. As may be seen, the structure of the wake in this two-dimensional case is completely different than that for the corresponding three-dimensional case. This is also apparent in the static pressure data shown in Figure 45, where for the three-dimensional 120-deg cone the static pressure in the wake centerline region is on the order of the free stream pressure and falling slightly; while for the two-dimensional 120-deg wedge the static pressure is a factor of two higher than the free stream pressure and increasing with increasing x/D . The profiles shown in Figures 43 and 44 are typical of the wake recirculating region; and the results, thus, suggest that for the two-dimensional case the wake neck may be located considerably further downstream than in the three-dimensional case. Alternatively, the presence of the pressure rake could have "blown" the wake or otherwise altered it so as to not correspond to the conventional wake case. If the wake neck is located far downstream, this will, of course, add to the possibility of this latter effect. In any event, the 120-deg wedge data were not considered to be of any real value to this study of two- and three-dimensional wakes, except as an illustration of the differences that can exist.



CONFIGURATION	TYPE DATA
○ 120-DEG WEDGE	WIND-TUNNEL
□ 120-DEG CONE	WIND-TUNNEL (REFERENCE 16)
— 120-DEG CONE	} WAKE THEORY (SECTION III)
- - - 120-DEG WEDGE	

Figure 43 - Wake Mach Number Profiles for 120-Deg Cone and 120-Deg Wedge at $x/D = 2.5$

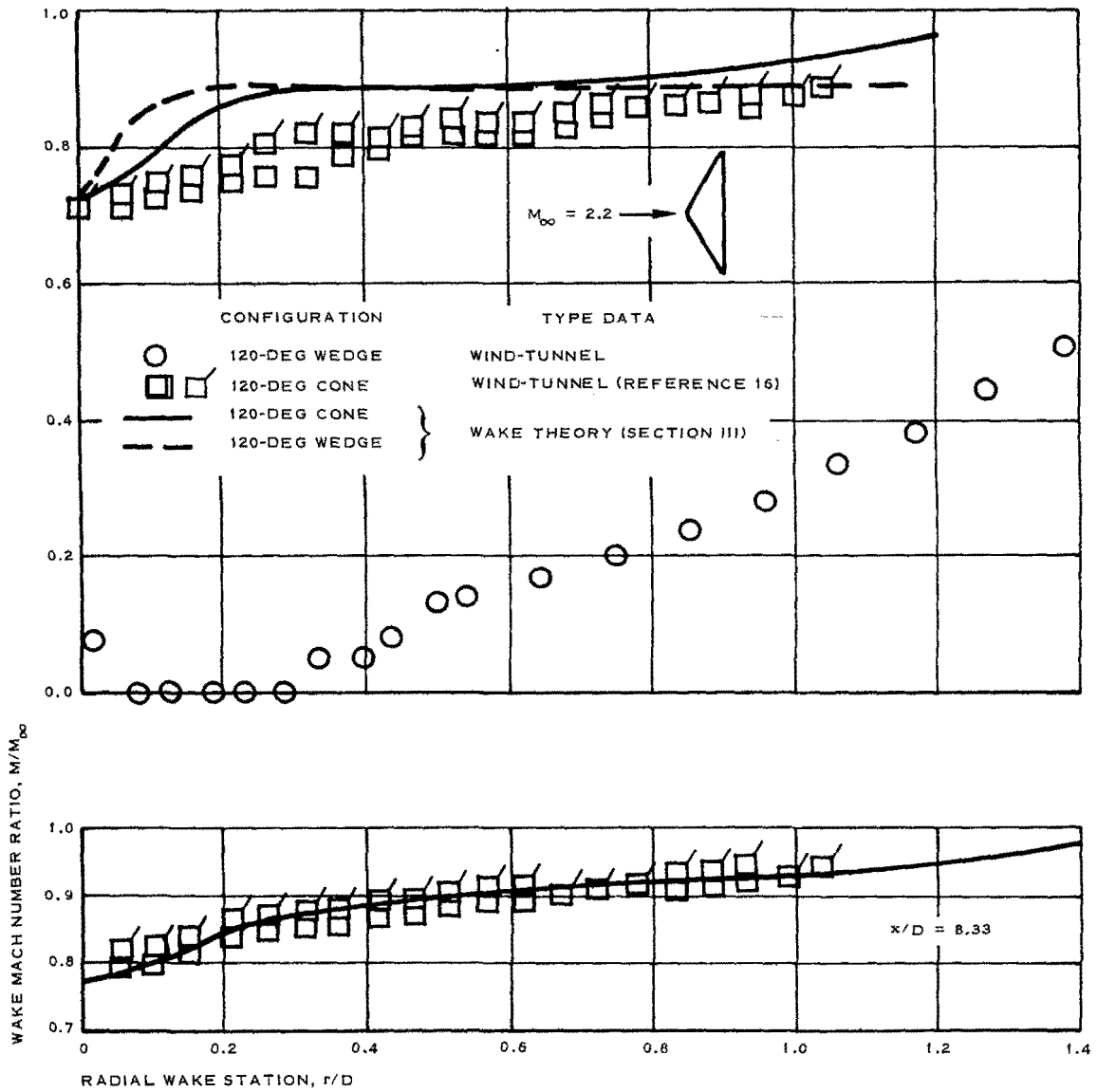


Figure 44 - Wake Mach Number Profiles for 120-Deg Cone and 120-Deg Wedge at $x/D = 5.04$ and $x/D = 8.33$

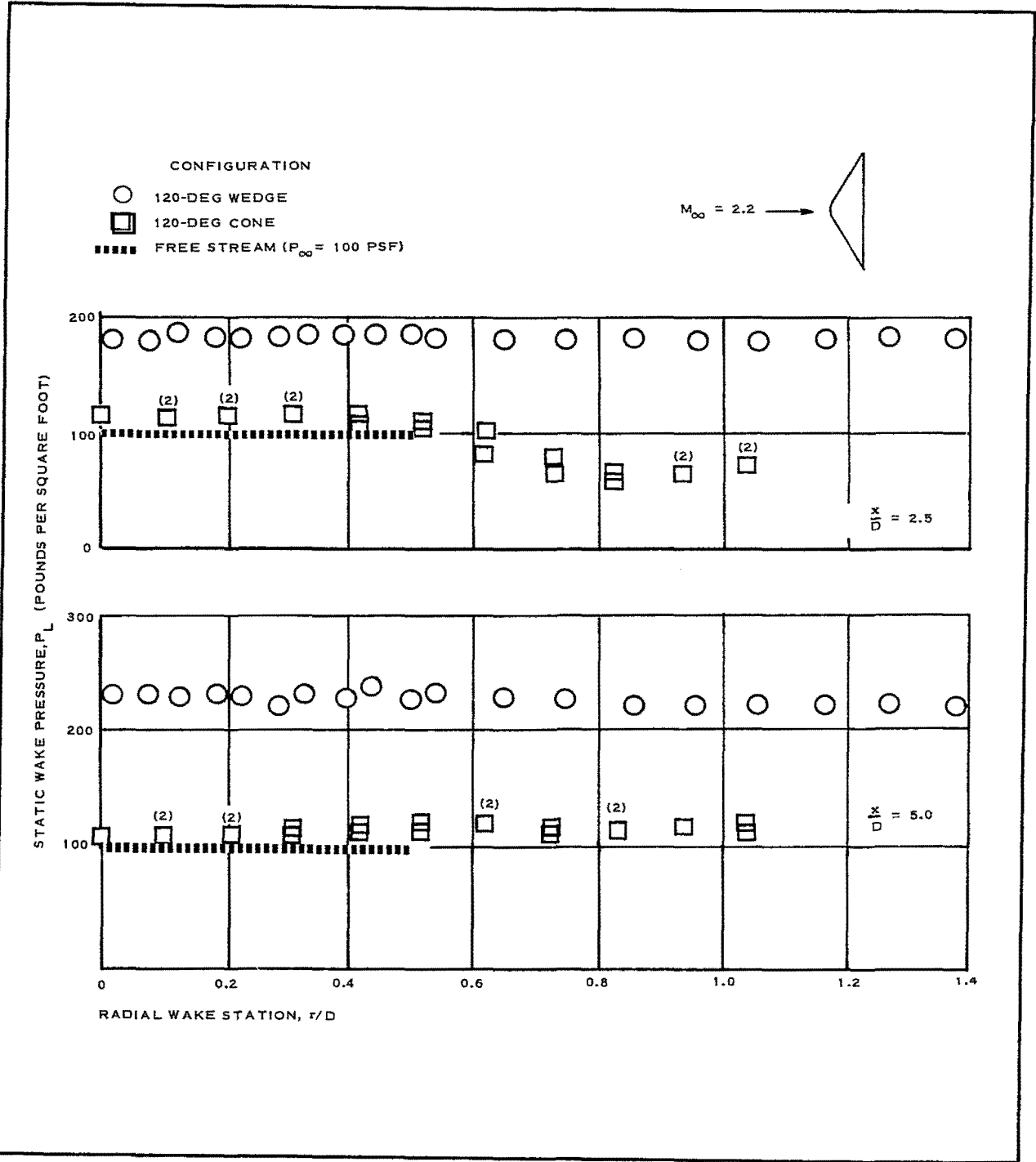


Figure 45 - Measured Local Wake Static Pressure for 120-Deg Cone and 120-Deg Wedge

Figures 46 through 48 present nondimensional Mach number profiles for the wake of a blunted cone-cylinder flare configuration. These data are for a free-stream Mach number value of 2.0, wake x/D -values of 5, 7, and 11, and viscosity model number 4. Here, again, the agreement between theory and experimental data is seen to be reasonably good. From these data, the recompression shock is not indicated and apparently resides outside the region shown. As indicated by the results, the viscous wake size is again slightly underpredicted by the theory, particularly at the lower x/D values.

The data and calculations shown in Figures 34 through 48 thus have been demonstrated to be in satisfactory agreement. Wake features omitted in the calculation procedure that contribute to differences which exist in these figures are as follows: (1) wake recompression shock wave, (2) near-wake flow characteristics, and (3) wake axial pressure gradients.

These omissions, while they could be corrected for, are not considered to impose any significant practical restrictions on the theory's assumed application to decelerator flow field calculations. One limiting feature is the assumption of Prandtl number equal to unity in the viscous wake theory. This affects the calculated wake profiles, and is, apparently, particularly important in the three-dimensional case. The removal of this restriction in the theory should lead to better agreement with the data with respect to the viscous wake width.

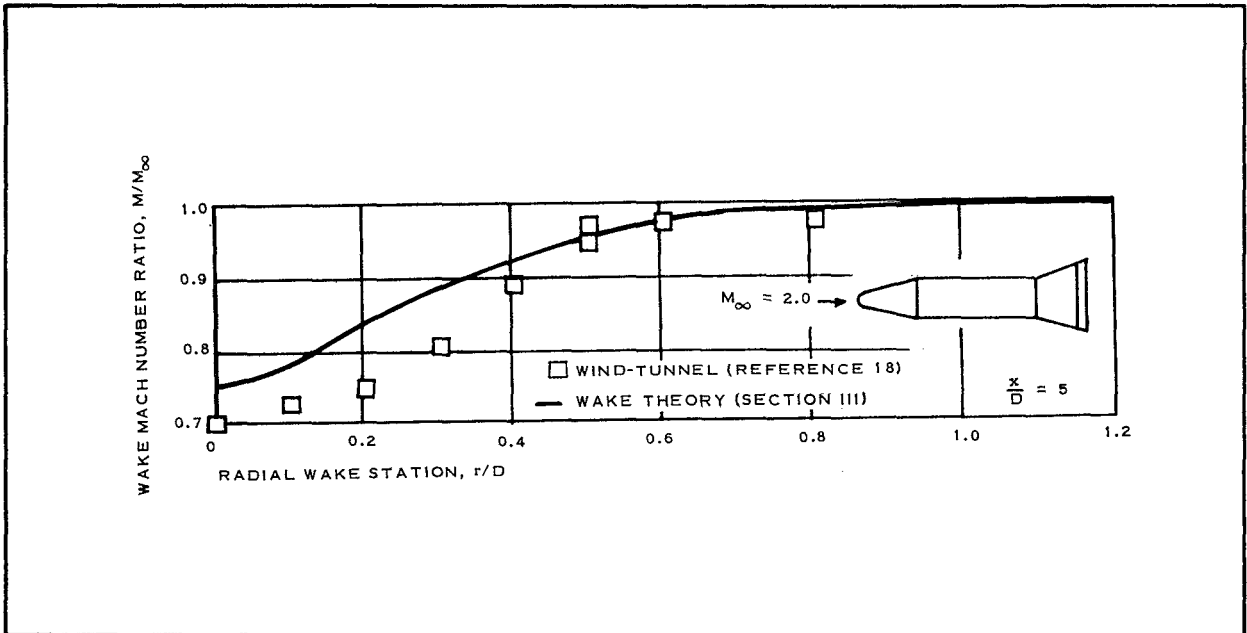


Figure 46 - Blunted Cone-Cylinder-Flare Wake Mach Number Profiles at $x/D = 5.0$

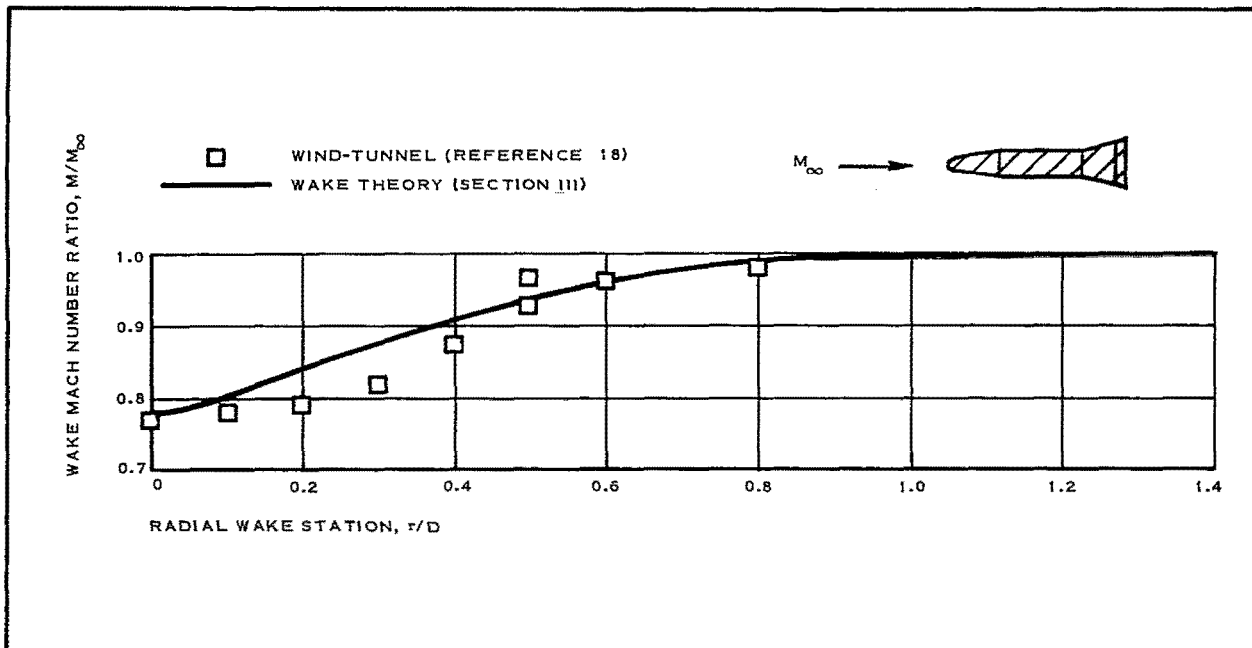


Figure 47 - Blunted Cone-Cylinder-Flare Wake Mach Number Profiles at $x/D = 7.0$

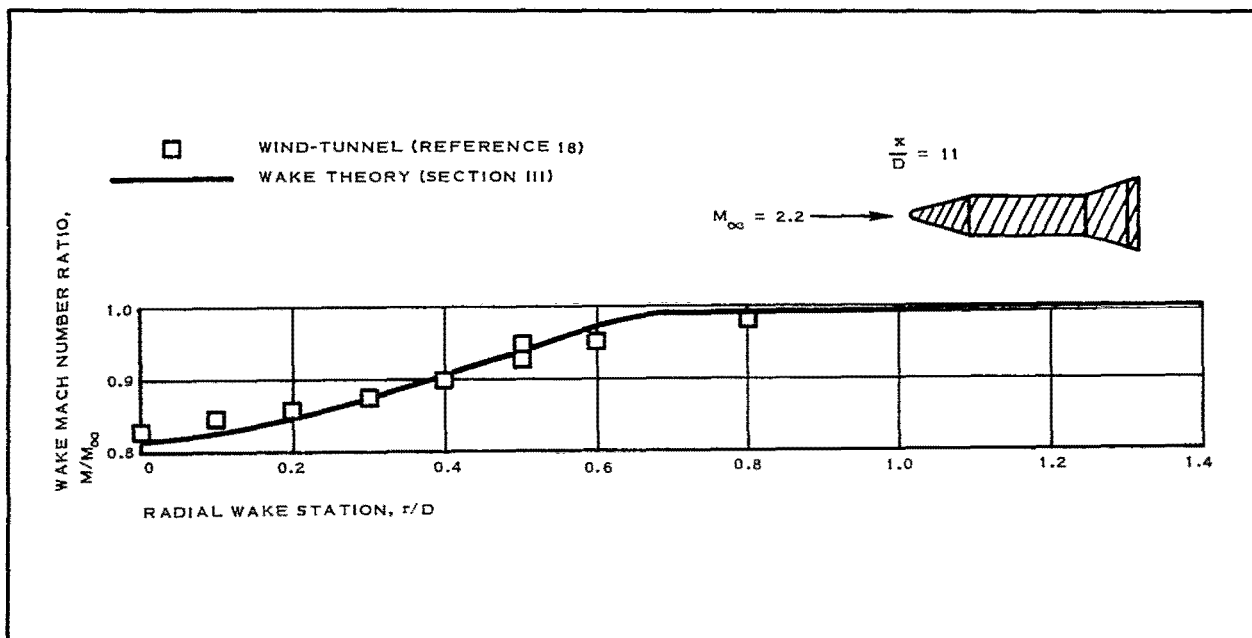


Figure 48 - Blunted Cone-Cylinder-Flare Wake Mach Number Profiles at $x/D = 11.0$

SECTION V - CONCLUSIONS AND RECOMMENDATIONS

1. CONCLUSIONS

Major conclusions of this study are:

1. Tow channel utility
 - a. Supercritical water flow patterns and data trends are similar to those in a supersonic compressible gas.
 - b. Due to basic differences in shock shape, inviscid flow field, and boundary layer characteristics, water wake results are generally not suitable for predicting compressible gas wake characteristics. Under certain conditions, however, a reasonable approximation of wake Mach number profiles may be obtained.
 - c. Detached hydraulic jumps in water theoretically can be modified to predict, with good accuracy, the shape of detached three-dimensional (axisymmetric) bow shocks in air. This predictive method can be extended to include two-dimensional angle of attack effects and, possibly, the effects of more complex axisymmetric body geometry.
2. Theoretical wake solution utility
 - a. Wake solution of Section III provides a reasonable first-order approximation to the two-dimensional and axisymmetric viscous and inviscid wake problem that should prove usable in engineering calculations of trailing decelerator flow fields.
 - b. The method of solution is generally applicable to both slender and blunt bodies having either attached or detached bow shocks.

2. RECOMMENDATIONS

Both tow channel data and the wake predictive method of Section III should be considered for use in calculating decelerator flow field characteristics. The theoretical solution enables the calculation of the decelerator's

effective free stream while tow channel data, with proper consideration of its limitations, may be useful in qualitatively studying the decelerator/wake interaction and in determining decelerator bow shock geometry. A combination of the two conceivably could offer a comparatively simple economical means of applying inverse methods to the problem of decelerator flow field calculations. To further improve the theoretical wake solution, certain improvements should be incorporated. The most desirable improvement, from a practical viewpoint, would appear to be the removal of the $Pr = 1$ restriction. This would provide for a broader viscous wake that would be more in agreement with that obtained from experimental results. Other important improvements would include providing for a better means of matching viscous and inviscid wake profiles and providing for the effects of embedded shock waves in the inviscid flow field and wake regions.

APPENDIX A - BOUNDARY LAYER THEORY^a

1. COMPRESSIBLE BOUNDARY LAYER MOMENTUM DEFECT CALCULATIONS

a. Laminary Boundary Layer Theory

For the methods developed by Kemp, Rose, and Detra (Reference 6) for calculating boundary layer properties and, in particular, calculating momentum thickness (θ), Stetson (Reference 19) has presented an empirical correlation of the results of the numerical solutions for θ , which is given by

$$\theta = \frac{\sqrt{2\xi}}{\rho_e u_e r^j} (0.491)(1 - 0.090\beta^{0.4})(\rho_e \mu_e / \rho_w \mu_w)^{0.386} \quad (90)$$

Here,

$$\xi = \int_0^s \rho_w \mu_w u_e r^{2j} ds$$

and s is the distance from the stagnation point as measured along the surface of the body: $j = 0$ for two-dimensional flow, and $j = 1$ for axisymmetric flow. For nonaxisymmetric flow, one of these two cases must be used as a suitable approximation. For example, a flat delta of small thickness ratio is best approximated as a two-dimensional body, while an elliptical body with its major and minor axes on the same order of magnitude is more suitably approximated as a quasiasymmetric body ($j = 1$).

In the above equations, the subscript e denotes local conditions at the edge of the boundary layer, while w denotes local gas conditions at the wall. The effect of β , the pressure gradient parameter, is small in Equation 90. This can be seen since β ranges from one at a two-dimensional stagnation point to zero in a zero pressure gradient region; thus, a typical value for β represents no more than a 10 percent correction.

In Equation 90, ξ represents an effective surface distance that considers the prior boundary layer history. For purposes of calculation, ξ can be rewritten as

^aThese results are reprinted from Reference 5 incorporating appropriate changes. They are entirely applicable to the development of Section III and are presented for completeness of this document.

$$\xi(s) = P_s V_\infty \frac{\mu_w}{R_1 T_w} R^{2j+1} \xi^* \quad (91)$$

where

$$\xi^* = \int_0^{s/R} \frac{P_e}{P_s} \frac{u_e}{V_\infty} \left(\frac{r}{R}\right)^{2j} d\left(\frac{s}{R}\right) \quad (92)$$

P_s is the forebody nose stagnation pressure, V_∞ the free-stream velocity, and R the base radius for an axisymmetric body or an effective base radius for a nonaxisymmetric body.

The boundary layer momentum thickness, θ , can be rewritten in terms of ξ^* . The result is

$$\frac{\theta}{R} = \frac{\sqrt{2} (0.491) (1 - 0.090\beta^{0.4}) \xi^{*1/2}}{\left(\frac{\rho_e u_e R}{\mu_e}\right)^{1/2} \left(\frac{u_e}{V_\infty}\right)^{1/2} \left(\frac{P_e}{P_s}\right)^{1/2} \left(\frac{r}{R}\right)^j \left(\frac{\rho_e \mu_e}{\rho_w \mu_w}\right)^{0.114}} \quad (93)$$

Here, β can be evaluated from

$$\beta = 2 \frac{\xi^*}{u_e} \left(\frac{\partial u_e}{\partial \xi^*}\right) \phi = \text{const.} \quad (94)$$

When the local boundary layer momentum is known, M can be evaluated from

$$M = \int_{\text{circumference}} \rho_e u_e^2 \theta ds \quad (95)$$

where ds is a circumferential increment of length. From Equation 93, $\rho_e u_e^2 \theta$ can be written as

$$\rho_e u_e^2 \theta = \frac{\rho_\infty V_\infty^2 R \sqrt{2} (0.491) (1 - 0.090\beta^{0.4}) \xi^{*1/2}}{\left(\frac{\rho_\infty V_\infty R}{\mu_\infty}\right)^{1/2} \left(\frac{\mu_\infty}{\mu_w}\right)^{1/2} \left(\frac{r}{R}\right)^j \left(\frac{\rho_w \mu_w}{\rho_e \mu_e}\right)^{0.386}} \left(\frac{u_e}{V_\infty} \frac{\rho_s}{\rho_\infty}\right)^{1/2} \left(\frac{T_w}{T_s}\right)^{1/2} \quad (96)$$

Thus, the integral in Equation 95 can be evaluated readily once the local flow properties have been used to evaluate ζ^* , θ/R , and $\rho_e u_e^2 \theta$. For a circular body and by evaluating the integral at the base,

$$M = \pi D \left(\rho_e u_e^2 \theta \right)_{\text{base}} . \quad (97)$$

For a body with an elliptical cross section, M can be expressed as

$$M = 4 \int_0^{\pi/2} \rho_e u_e^2 \frac{\theta}{R} G_1 R^2 d\phi , \quad (98)$$

where, because of the symmetry, it is only necessary to integrate over one quadrant, and where

$$G_1 = \frac{1}{R} \frac{ds}{d\phi} \frac{\left[1 + \frac{\sin^2 \phi \cos^2 \phi}{\left(\frac{\sin^2 \phi}{b^2} + \frac{\cos^2 \phi}{a^2} \right)^2} \left(\frac{1}{b^2} - \frac{1}{a^2} \right)^2 \right]^{1/2}}{\left[ab \left(\frac{\sin^2 \phi}{b^2} + \frac{\cos^2 \phi}{a^2} \right) \right]^{1/2}} . \quad (99)$$

Here, b and a are the semiaxes of the ellipse. G_1 is unity for a cylindrical body.

Once the inviscid flow properties along the edge of the body boundary layer are known, and assuming the wall temperature is known or can be estimated, then the boundary layer momentum thickness and integrated momentum defect can be evaluated using Equations 93 and 95.

Turbulent Boundary Layer Theory

Unfortunately, the state of knowledge regarding turbulent boundary layers is not so well developed as in the laminar case. Thus, although there have been many approximate treatments of turbulent flow, most of which can be supported to some extent by using existing experimental data, there are no "exact" theoretical solutions (such as those of Kemp, Rose, and Detra) for laminar flow.

One approximate solution, the results of which lend themselves to the present problem, is that of Reshotko and Tucker (Reference 7). This solution uses the momentum integral and moment-of-momentum equations as simplified using Stewartson's transformation. To solve these two equations, a skin friction relation must be used; Reshotko and Tucker chose the Ludwig-Tillman relation in a form suitable for compressible flow with heat transfer through applying the reference enthalpy concept.

The above equations were simplified further by using an approximate shear stress distribution and the power law velocity profile.

The moment-of-momentum equation is needed to account for pressure gradient effects on the boundary layer velocity profile. The method of Reshotko and Tucker, as applied to insulated surfaces, is quite well founded. However, for noninsulated or nonadiabatic wall cases the method, though qualitatively correct, is based on some speculative assumptions. It is still anticipated, however, that for such cases the method will yield reasonable quantitative results. The method certainly is representative of the best that can be done within the present status of turbulent flow theory.

Reshotko and Tucker in Reference 7 present their results for momentum thickness in terms of a transformed momentum thickness, θ_{tr} . The transformed momentum thickness, θ_{tr} , can be related to the actual momentum thickness, θ , by

$$\theta = \theta_{tr} \left(1 + \frac{\gamma - 1}{2} M_e^2 \right)^3 . \quad (100)$$

The solution for θ_{tr} is

$$\theta_{tr} = \left[\theta_{tr} \left(\frac{M_e a_o \theta_{tr}}{\nu_o} \right)^{0.2155} M_e^B R^{1.2155k} \right]_s - \left[\theta_{tr} \left(\frac{M_e a_o \theta_{tr}}{\nu_o} \right)^{0.2155} M_e^B R^{1.2155k} \right]_{s_1}$$

$$= 0.01173 \int_{s_1}^s \frac{M_e^B \left(\frac{T_e}{T_{ref}} \right)^{0.732} R^{1.2155k} ds}{\left(\frac{T_o}{T_e} \right)^{3.268}} . \quad (101)$$

Here, a_o and ν_o are the velocity of sound and the kinematic viscosity evaluated at the stagnation conditions of the local external stream, respectively. The exponent B can be expressed approximately as

$$B = 4.2 + 1.58 \left(\frac{T_w}{T_o} \right) - 1 , \quad (102)$$

where T_o is the inviscid stagnation temperature. The reference temperature, T_{ref} , is given as

$$T_{ref} = 0.50 (T_w + T_e) + 0.22 (T_{aw} - T_e) , \quad (103)$$

where T_{aw} is the adiabatic wall or recovery temperature

$$T_{aw} = T_e \left(1 + \frac{\gamma - 1}{2} M_e^2 \text{Pr}^{1/3} \right). \quad (104)$$

The distance, s_1 , in Equation 101 is the starting point of the calculation. If the boundary layer is turbulent over the entire body, then $s_1 = 0$, and the calculation starts at the forward stagnation point. However, if the boundary layer is initially laminar, then the calculation starts at $s = s_1$, the transition point. At that point,

$$\theta(\text{turbulent}) = \theta(\text{laminar}) \cdot \quad (105)$$

The previously noted equation for a compressible turbulent boundary layer (Equation 101), can be recast in terms of a turbulent distance parameter, ξ_T^* , where

$$\xi_T^* = \frac{1}{M_e^B \left(\frac{r}{R} \right)^{1.2155k}} \int_{\frac{s_1}{R}}^{s/R} \frac{M_e^B \left(\frac{r}{R} \right)^{1.2155k}}{\left(\frac{T_{ref}}{T_e} \right)^{0.732} \left(\frac{T_o}{T_e} \right)^{3.268}} d\frac{s}{R} \cdot \quad (106)$$

The transformed momentum thickness, θ_{tr} , then can be expressed as

$$\left(\frac{\theta_{tr}}{R} \right)^{1.2155} = \left[\frac{\theta_{tr}(TR)}{R} \right]^{1.2155} \left[\frac{P_o}{P_o(TR)} \right]^{0.2155} \left[\frac{M_e(TR)}{M_e} \right]^{0.2155 + B} \times \frac{\left[\frac{r(TR)}{R} \right]^{1.2155k}}{\left(\frac{r}{R} \right)^{1.2155k}} + \frac{0.01173 \xi_T^*}{\left(\frac{M_e Ra_o}{\mu_o / \rho_o} \right)^{0.2155}} \cdot \quad (107)$$

TR indicates that the property is to be evaluated at the transition point.

When θ_{tr} is known, the actual momentum thickness, θ , can be evaluated as can Re_θ , $\rho_e u_e^2 \theta$, and M . For this latter quantity, Equations 97 through 99 are applicable. Thus, calculations can be carried out for the important boundary layer properties once the properties at the edge of the boundary layer are known.

2. BOUNDARY LAYER TRANSITION PREDICTION

a. General

A criterion for boundary layer transition was established that could be incorporated into a general laminar-turbulent boundary layer calculation program. Any such criteria must, because of what is known regarding transition and turbulent flow, be considered as leading to only an approximate estimate.

In developing transition prediction criteria, recognition must first be made of the factors that influence transition, the parameters in terms of which transition correlations usually are made, and which of these factors are important and can be considered realistically. In general, boundary layer transition depends on the Reynolds number of the flow, surface roughness, free-stream turbulence, noise, compressibility effects and/or pressure gradient effects, and whether the boundary layer is being heated or cooled. Except for effects due to surface roughness and free-stream turbulence, one might think that the other effects are of such a nature that methods of predicting their associated influence on transition could be developed. However, the effects of roughness and turbulence each may couple with the other factors, thus making any attempt to separate one effect from another extremely difficult.

As an example, the effect of surface roughness depends on the thickness of the boundary layer, but the thickness of the boundary layer depends on the compressibility of the fluid (as manifested through the local Mach number) and whether the boundary layer is being heated or cooled, as well as many other factors. The free-stream turbulence also may vary with tunnel conditions. Thus, the individual factors do couple with one another.

In evaluating factors affecting transition (see Figure 49), Low, in Reference 20, presents a curve showing the effect of free-stream turbulence on transition.

Gazley (Reference 21) found that laminar boundary layer oscillations and their damping or amplification could be detected only when the free-stream turbulence was less than 0.001. For greater turbulence values, the boundary layer oscillations became difficult to identify because of the near coincidence of their appearance with the point of transition to turbulence. Gazley also reported that the effects of free-stream turbulence tend to mask out the effects of other variables. This may explain the disagreement between Stainback (Reference 22) and Gazley. Stainback's results tended to confirm the invariance of transition Reynolds number with Mach number up to Mach 8; Gazley's results indicated an increase of transition Reynolds number with increasing Mach number.

Both Deem (Reference 23) and Stewart (Reference 24) indicate an increase of transition Reynolds number with an increase of unit Reynolds number.

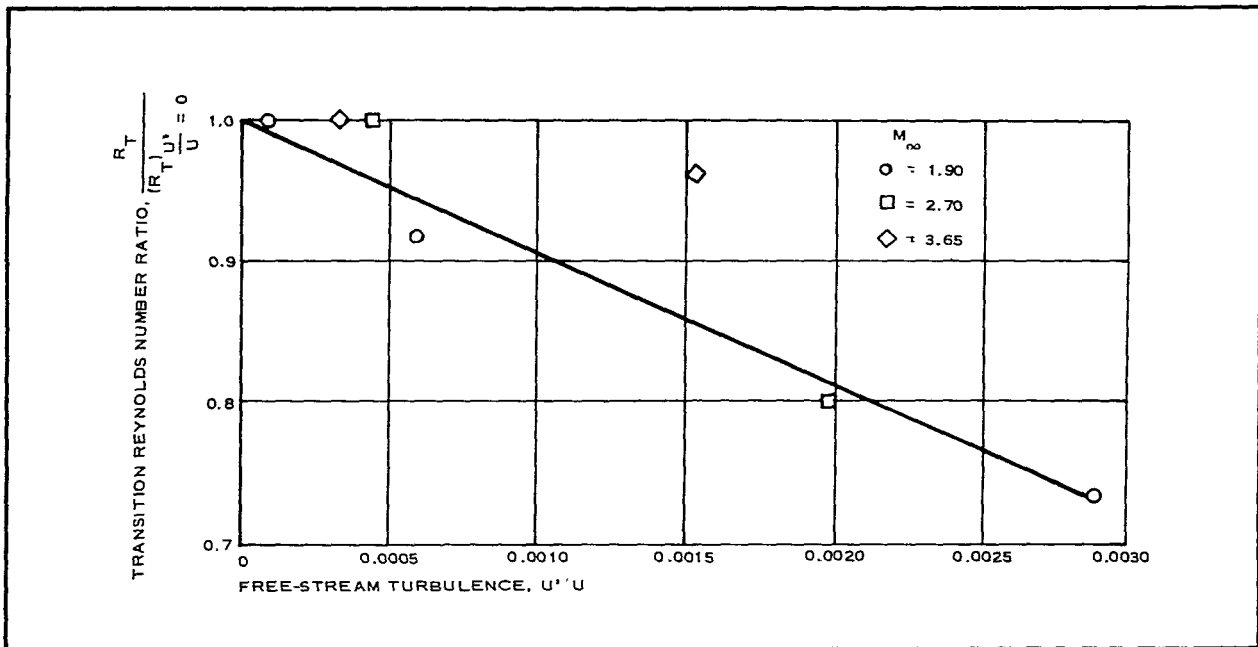


Figure 49 - Free Stream Turbulence, U'/U

Deem also observed a transition reversal phenomenon due to changes in wall to adiabatic wall temperature ratios.

Correlations of boundary layer transition usually are presented in the form of a transition Reynolds number as a function of other flow similarity parameters. Although experimental data frequently are presented using the free-stream Reynolds number based on X (Re_X), Reynolds numbers based on momentum thickness and displacement thickness also are used. If the transition process itself is viewed as originating through local boundary layer separation occurring because of a local momentum deficiency, then the local Reynolds number based on momentum thickness, Re_θ , would seem to be the appropriate dependent variable. For an incompressible, flat-plate boundary layer, the critical value of Re_θ corresponding to the boundary layer becoming unstable to small disturbances (e.g., Tollmien-Schlichting waves) is 163 (Reference 25). On the other hand, the transition value may range as high as 1300, depending on the exact surface roughness and free-stream turbulence, both of which tend to decrease the value of the transition Reynolds number. For compressible flows, the Mach number and the ratio of the wall enthalpy to the adiabatic wall enthalpy also become important.

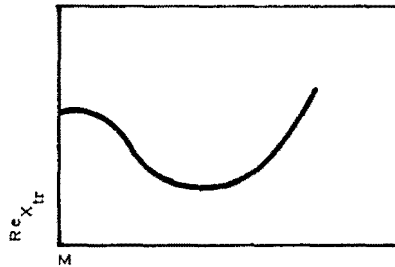
Pressure gradient effects (a favorable gradient stabilizes the boundary layer while an unfavorable gradient destabilizes it), although important, are much more difficult to consider. The unit Reynolds number also is

included in many correlations of transition data. Originally, this parameter may have been related to wind-tunnel produced disturbances. However, there is now some evidence that it also is an important effect in correlating ballistic range and flight data. Its role, however, is not understood from a physical viewpoint.

b. Analysis

In developing a rather simple correlation for the transition Reynolds number based on momentum thickness, only the effects of Mach number and h_w/h_{aw} are considered directly. Since the present boundary layer computer program calculated Re_θ , it is convenient to treat the transition problem in terms of this parameter. Furthermore, the free-stream Mach number range of interest in this study is from 1 to 5. For a blunt nose body, this means local Mach numbers of less than 3.5.

In general, the effect of the local Mach number on the transition Reynolds number in terms of X can be represented as shown in the following sketch (References 25 and 26).



A curve of this type can be represented by a power series of the form

$$Re_{X_{tr}} = (Re_{X_{TR}})_{inc} \sum_{n=0}^m a_n M^n \quad (108)$$

If only the first four terms in the power series are used, the following boundary conditions can be applied:

1. $M = 0, Re_{X_{tr}} = (Re_{X_{tr}})_{inc}$ (a value of 2.5×10^6 was chosen)

2. $M = 0, dRe_{X_{tr}}/dM = 0$
3. $M = M_1, dRe_{X_{tr}}/dM = 0$ (M_1 based on experimental data)
4. $M = M_1, Re_{X_{tr}} / (Re_{X_{tr}} / (Re_{X_{tr}})_{inc})$ (matched with experimental data)

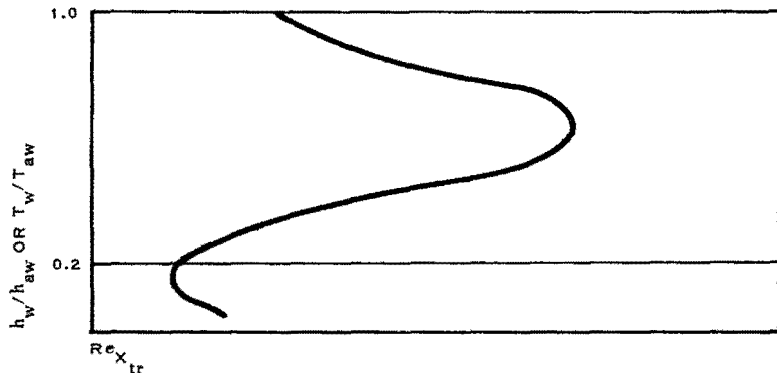
If boundary conditions 3 and 4 are selected based on References 26 and 27, Equation 108 then becomes:

$$Re_{X_{tr}} = 2.5 \times 10^6 (1 - 0.12 M^2 + 0.023 M^3) . \quad (109)$$

Since $Re_{\theta} \approx 0.664 Re_X^{1/2}$, (Reference 8), then

$$Re_{\theta_{tr}} \approx 1000 (1 - 0.12 M^2 + 0.023 M^3)^{1/2} . \quad (110)$$

The effect of h_w/h_{aw} is illustrated in the following sketch:



This curve can be represented by a power series of the form

$$Re_{X_{tr}} = (Re_{X_{tr}})_{T_w = T_{aw}} \sum_{n=0}^m b_n \left(\frac{h_w}{h_{aw}} \right)^n , \quad (111)$$

which can be fitted to available experimental data. When the range, $0.2 \leq h_w/h_{aw} \leq 1.0$, is considered, the boundary conditions become

1. $h_w/h_{aw} = 1, Re_{X_{tr}} = (Re_{X_{tr}})_{T_w = T_{aw}}$
2. $h_w/h_{aw} = \bar{h}_1, Re_{X_{tr}}$ (matched with experimental data)
3. $h_w/h_{aw} = \bar{h}_1, dRe_{X_{tr}}/dh_w = 0$
4. $h_w/h_{aw} = 0.2, Re_{X_{tr}}$ (matched with experimental data)

are used, and where $Re_\theta \propto Re_X^{1/2}$, the correlation of Equation 110 becomes

$$Re_{\theta_{tr}} \approx 1000 (1 - 0.12 M^2 + 0.023 M^3)^{1/2} \times (-2.29 + 17.38 \bar{h} - 18 \bar{h}^2 + 3.91 \bar{h}^3)^{1/2} \quad (112)$$

where $\bar{h} = h_w/h_{aw}$. Here, the effects due to h_w/h_{aw} are based on the experimental data of References 28 through 30.

The nature of this correlation is that transition reversal is included. However, the second transition reversal frequently found at values of h_w/h_{aw} of approximately 0.2 is not included. The correlation (Equation 112) thus is limited to $h_w/h_{aw} > 0.2$. Reshotko (Reference 31) has qualitatively explained both transition reversal phenomena. However, a general agreement among the available experimental data does not exist; the correlation, though qualitatively correct, is quantitatively only an approximation.

In representing the effects of Mach number and h_w/h_{aw} using power series, the coefficients in these series should be treated as functions of surface roughness and free-stream turbulence.

Pressure gradient effects, as noted before, also may be important. On this project, the primary bodies of interest are such that, excluding the nose region, the body is divided into regions of zero pressure gradient. This should be a reasonable approximation, even in the prediction of transition, with the one exception being at the junction of the cylindrical afterbody and the flare at the base of the body. The adverse pressure gradient there may produce transition if the Reynolds number is greater than the critical value. Thus, it was suggested that, in programming the boundary layer calculations, Re_θ at the initiation of the flare be checked against $(Re_\theta)_{CRIT}$ as given below:

$$(Re_{\theta})_{CRIT} \approx 163 (1 - 0.12 M^2 + 0.023 M^3)^{1/2} \times (-2.29 + 17.38 \bar{h} - 18 \bar{h}^2 + 3.91 \bar{h}^3)^{1/2} \quad (113)$$

This equation is merely Equation 112 with the incompressible transition value of a 1000 replaced by critical value 163). If, at the flare, $Re_{\theta} \geq (Re_{\theta})_{CRIT}$, then transition is assumed to occur. If $Re_{\theta} < (Re_{\theta})_{CRIT}$, then the boundary layer remains laminar. With the inclusion of this criterion in the program boundary layer transition should at least be accounted for in a quantitatively correct manner.

The present correlation, Equation 113, has been compared with experimental results from Reference 24 on the effect of T_w/T_{aw} obtained at $M_{\infty} = 3.1$. Approximate agreement has been found to exist. The results of Stetson and Rushton (Reference 32) also have been compared; these results were obtained on blunt cones at a free-stream Mach number of $M_{\infty} = 5.5$ (see Figure 50). Here, X_T is the transition distance, X_{sw} is the distance for the high entropy layer to be swallowed, and Re_{θ_T} is the transition Reynolds number based on momentum thickness. The prediction based on the present method is shown only for one condition; however, reasonable agreement exists.

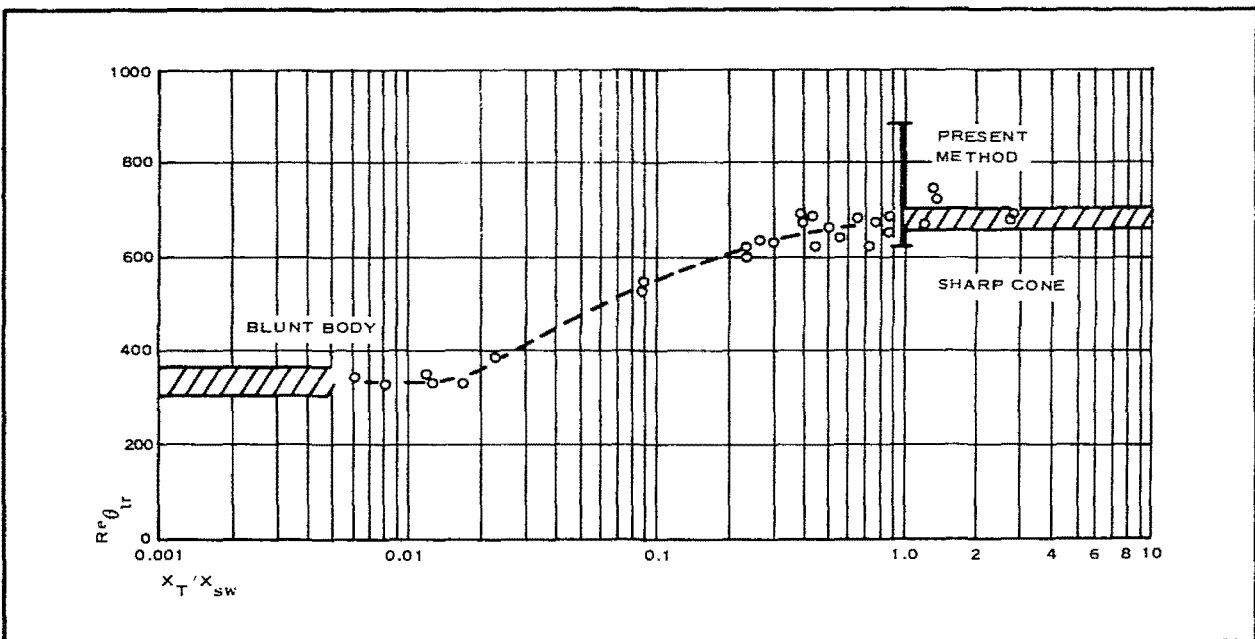


Figure 50 - Boundary Layer Transition on a Blunt Cone at $M_{\infty} = 5.5$

Equations 112 and 113 have been programmed as a part of the boundary layer program and are used to determine the approximate location of transition if the exact location of transition is not specified as an input.

APPENDIX B - FOREBODY FLOW FIELD PROGRAM^a

The forebody geometry is stored as a table to allow all necessary geometric properties to be determined by simple calculation from the geometric coordinates. The storage system defines the body profile as a series of points that are the values of the distance r from the forebody axis to its surface and as a function of the axial distance x from the nose of the body. Thirteen profiles are stored on 13 planes formed by rotating the vertical plane containing the forebody axis about this axis 90 deg in 7.5-deg increments. Mirror symmetry is assumed about the vertical and horizontal planes in the axisymmetric case. For two-dimensional bodies, only the $\phi = 0$ case is considered.

The one geometric input required by the boundary layer program is the value of r/R , where R is average base radius. The value, r , is found as a function of x along any one ϕ by linear interpolation between the points stored in the table.

For the pressure distribution subroutine, the angle of the forebody surface in each ϕ plane with the body axis must be known. To calculate this,

$$\theta_{i, \phi} = \arctan \frac{r_{i+1, \phi} - r_{i, \phi}}{x_{i+1, \phi} - x_{i, \phi}} . \quad (114)$$

The application of the modified Newtonian flow method and the tangent-wedge (2-D) or tangent-cone (3-D) method for estimating the static pressure distribution is governed by the following logic. The free-system Mach number and the static pressure (M_{∞} and p_{∞}) are inputs to the pressure distribution subroutine. For each ϕ profile, the following checks and decisions are made.

The nose angle is calculated from the stored geometry,

$$\theta_{0, \phi} = \arctan \frac{r_{1, \phi} - r_{0, \phi}}{x_{1, \phi} - x_{0, \phi}} . \quad (115)$$

This value then is compared with a stored curve of θ_c versus M_{∞} , where θ_c is the critical angle between conical or wedge flow with an attached shock and flow with a detached shock.

Case A

$$\theta_{0, \phi} \geq \theta_c .$$

^aThese results are reprinted in a modified form from Reference 5 to include appropriate two-dimensional calculation methods applicable to the development of Section III.

If $\theta_{0, \phi}$ is equal to or larger than θ_c , then the shock wave is detached from the nose, and static pressure is estimated by the Newtonian flow

$$p_e = p_\infty + (p_s - p_\infty) \sin^2 \theta_{0, \phi} ,$$

where p_s is the nose total pressure. Since there is a detached shock, p_s is the total pressure behind the normal shock.

$$p_s = p_\infty \left[\frac{(\gamma + 1)M_\infty^2}{2} \right]^{\frac{\gamma}{\gamma - 1}} \left[\frac{\gamma + 1}{2\gamma M_\infty^2 - (\gamma - 1)} \right]^{\frac{1}{\gamma - 1}} \quad (116)$$

Case B

$$\theta_{0, \phi} < \theta_c .$$

If $\theta_{0, \phi}$ is less than θ_c , then an attached shock exists, and both the static and nose total pressure are evaluated from either the conical flow subroutine (3-D) or from the oblique shock subroutine (2-D). For both cases, the local Mach number is given by

$$M_e = \sqrt{\frac{2}{\gamma - 1} \left[\left(\frac{p_o}{p_e} \right)^{\frac{\gamma - 1}{\gamma}} - 1 \right]} ,$$

where p_o is the local total pressure. In this region, $p_o = p_s$.

This solution is carried out at each point on the body profile. As long as $\theta_{i, \phi} > \theta_{i+1, \phi}$, the local total pressure is equal to the nose total pressure for both cases. If the shock wave is detached, the static pressure is obtained by the modified Newtonian method until $\theta_{i, \phi} < \theta_c$, after which the conical flow solution or oblique shock flow solution is used.

If, however, $\theta_{i, \phi} < \theta_{i+1, \phi}$, a corner shock forms, and the local total pressure changes. To evaluate this condition, the flow properties in the region x_{i-1} to x_i are used, and the angle $\bar{\theta} = \theta_{i+1, \phi} - \theta_{i, \phi}$ is the cone or wedge semiangle of interest. As before, there are two possible cases. For Case A where $\bar{\theta} \geq \theta_c$ for M_{e_i} ,

$$p_{e_{i+1}} = p_\infty + \left(p_{o_{i+1}} - p_\infty \right) \sin^2 \bar{\theta} ,$$

where $p_{o_{i+1}}$ = local total pressure behind a detached (normal) shock. This pressure is given by

$$P_{o_{i+1}} = P_s \left[\frac{(\gamma + 1)M_{e_i}^2}{(\gamma - 1)M_{e_i}^2 + 2} \right]^{\frac{\gamma}{\gamma - 1}} \left[\frac{\gamma + 1}{2\gamma M_{e_i}^2 - (\gamma - 1)} \right]^{\frac{1}{\gamma - 1}} .$$

For Case B where $\bar{\theta}$ is less than θ_c for $M_{e_{i-1}}$, the static and total pressures are taken from the conical flow routine or the oblique shock flow routine using the local properties at point i as inputs. Again the Mach number is given in either case by

$$M_e = \sqrt{\frac{2}{\gamma - 1} \left[\left(\frac{P_{o_{i+1}}}{P_e} \right)^{\frac{\gamma - 1}{\gamma}} - 1 \right]} . \quad (117)$$



APPENDIX C - BOUNDARY LAYER AND WAKE COMPUTER PROGRAM

1. FOREBODY BOUNDARY LAYER PROGRAM

Forebody boundary layer calculations may be performed for the following cases and conditions:

1. Two dimensional or axisymmetric bodies at 0-deg angle of attack
2. Laminar and/or turbulent flows - including transition
3. Incompressible, subsonic, transonic and supersonic flows

In all cases, the forebody pressure distribution must be known. For supersonic or hypersonic flow cases, the computer program will predict the pressure distribution using tangent cone theory, tangent wedge theory, modified Newtonian flow theory or a combination thereof. Alternatively, experimental data or the results of other pressure distribution calculations may be inputted into the program. In addition to the pressure distribution, the body geometry and free stream flow properties (including fluid properties of state) must be specified.

For the gas to be considered, the free-stream density, viscosity, Prandtl number, specific heat ratio, and gas constant must be specified. A viscosity-temperature relationship also must be specified. (For air, treated as a perfect gas, the Sutherland viscosity-temperature equation is used in the program and the free stream density and viscosity are automatically calculated).

With these inputs specified, the laminar boundary layer properties are computed using the method of local similarity solutions of Kemp, Rose, and Detra,⁶ along with the momentum thickness correlation of Stetson.¹⁹ These solutions apply to compressible flow and include the effects of dissociation and equilibrium air conditions. For the turbulent boundary layer case, the momentum integral solution of Reshotko and Tucker⁷ is used.

Boundary layer transition is also included in the computer program. A transition point location along the body may be specified or a transition Reynolds number based on momentum thickness may be specified. If neither of the above are specified, the program will compute a transition Reynolds number using the criteria developed in Reference 5, and for compression corners the program will compute a critical Reynolds number criteria for transition. Then beginning with a laminar boundary layer calculation, the program will switch to a turbulent calculation at the specified transition point or at the point where the specified or computer transition Reynolds number is reached.

After completing the laminar or turbulent calculations over the forebody, the boundary layer program yields the integrated momentum defect as well as transition point and forebody base values of local Reynolds number based on momentum thickness, local momentum defect, local density, and local velocity. The boundary layer momentum defect then is matched to that of the viscous wake for the start of wake calculations.

2. WAKE COMPUTER PROGRAM

a. Calculations

Calculations to determine the wake flow field behind a forebody may be performed for the following cases and conditions:

1. Two dimensional or axisymmetric forebodies at 0-deg angle of attack
2. Inviscid wake flows and laminar or turbulent viscous wake flows
3. Incompressible, subsonic, transonic or supersonic flows

b. Viscous Wake

The primary input to the viscous wake computer program is the forebody boundary layer momentum defect. In addition, the free stream properties and the local and total pressures at the edge of the boundary layer at the base of the forebody also are required. Since the forebody boundary layer program and the wake program are both a part of the total "Forebody and Wake Computer Program" certain required inputs are carried over from the boundary layer program and need not be specified again in order to begin the wake calculations. Thus, the new inputs required for the wake computer program are:

1. Wake neck locations, x/D , at which wake profiles are to be calculated
2. Starting point for the viscous wake solution
3. Starting point value of the form parameter,
4. Viscosity model number
5. Viscosity coefficient, k
6. Enthalpy ratio coefficient, k_3
7. Forebody bow shock shape (for inviscid wake only)

Generally, the starting point for the viscous wake solution is the wake neck location. However, the rear stagnation point or any other point downstream of the rear stagnation point (for which the value of ξ is known) may be used. Four different viscosity models are currently stored in the computer program (see Section III). Viscosity model number 4 along with a viscosity coefficient equal to 0.020 is currently used for all viscous wake calculations. Because the loss of momentum defect between the forebody base and the viscous wake downstream of the recirculation region is considered to be negligible, the enthalpy ratio is set equal to unity.

With the wake inputs defined, the viscous wake calculations may be carried out using a momentum integral method of solution (see Section III) which is applicable to both laminar and turbulent flow.

For the viscous wake solution, it first must be determined whether the wake is laminar or turbulent. If the forebody boundary layer is turbulent, then the wake obviously is turbulent. But if the forebody boundary layer is laminar, a test must be made for wake transition. If the wake transition Reynolds number is not known, a wake transition criteria based on experimental data and contained in the computer program may be used. This test for wake transition is made only at the beginning of the wake calculations, and thus the viscous wake in the presence of a riser line or tow cable will be either wholly laminar or wholly turbulent. The above criteria is applicable only to supersonic and hypersonic wake flows. For subsonic wake flows, the transition Reynolds number must be specified.

Inviscid Wake

For the inviscid wake, deviations from the free stream conditions are primarily due to the presence of shock waves - both the bow shock wave and imbedded shocks (flare induced compression waves, viscous wake recompression shock, etc.). For supersonic flow, the inviscid wake calculation procedure assumes these imbedded shock waves are negligible. It therefore uses only the bow shock wave together with the mass flow balance calculation procedure to predict the inviscid wake profiles.

The bow shock shape is input in terms of a polynomial curve fit to the experimental shock shape of the form

$$\frac{r}{d_N} = a + b \left(\frac{x}{d_N} \right) + c \left(\frac{x}{d_N} \right)^2 + d \left(\frac{x}{d_N} \right) \left(\frac{r}{d_N} \right) \quad (118)$$

where d_N is a normalizing diameter. The polynomial coefficients a , b , c , d in Equation (118) were obtained using a multiple regression curve fit program into which an experimental shock shape was input. For subsonic and transonic flow the inviscid wake is treated as corresponding to the free stream condition.

A sample computer output format is reproduced on the following pages. This computer run was made for a blunted cone-cylinder-flare configuration in a Mach 3 air flow regime. As indicated, pertinent forebody boundary layer data are provided including the momentum defect at the base. Wake computations are then carried out using this data and equating the forebody base momentum defect with the momentum defect in the wake. In the example, viscous and inviscid wake calculations are provided for two axial wake stations: $x/D = 9$ and $\bar{x}/D = 11$.

BOUNDARY LAYER AND WAKE COMPUTER PROGRAM

BLUNTED CONE-CYLINDER-FLARE-CYLINDER

CASE: THREE DIMENSIONAL FLOW

FLOW PROPERTIES:

FREE STREAM MACH NO	3.000	
FREE STREAM VELOCITY	2120.681	FT/SFC
FREE STREAM STATIC PRES	23.100	LB/FT SQ
FREE STREAM TOTAL PRES	848.523	LB/FT SQ
TOTAL PRES BEHIND SHOCK	278.608	LB/FT SQ
FREE STREAM STATIC TEMP	208.000	DEG P
TOTAL TEMP	582.399	DEG R
BODY WALL TEMP	567.000	DEG R
FREE STREAM DENSITY	6.4719E-05	SLUG/FT CU
FREE STREAM VISCOSITY	1.6682E-07	SLUG/FT CU
SPECIFIC HEAT RATIO	1.400	
PRANDTL NO	0.710	
GAS CONSTANT	1716.000	FT SQ/SFC SQ DEG R

BODY GEOMETRY:

BODY IS AXISYMMETRIC

SEMI MAJOR AXIS	0.1340	FT
SEMI MINOR AXIS	0.1340	FT
MEAN BASE RADIUS	0.1340	FT
BODY FINENESS RATIO	4.6010	

MERIDIAN ANGLE PHI	0.0	DEG
--------------------	-----	-----

X COORDINATES (FT)

0.0018	0.0057	0.0147	0.0237	0.2658	1.0217	1.1667	1.2333
--------	--------	--------	--------	--------	--------	--------	--------

R COORDINATES (FT)

0.0103	0.0177	0.0262	0.0296	0.0833	0.0833	0.1342	0.1342
--------	--------	--------	--------	--------	--------	--------	--------

SURFACE COORDINATES (S/R)

0.0	0.0783	0.1409	0.2326	0.3041	0.3042	2.1553	2.1554	7.7958	7.7959	8.9425	8.9426
9.4401											

BOUNDARY LAYER COMPUTATIONS

MERIDIAN ANGLE PHI 0.0 DEG

BODY SURFACE COORDINATES (S/R)

0.0 0.0783 0.1409 0.2326 0.3041 0.3042 2.1553 2.1554 7.7958 7.7959 8.9425 8.9426
9.4401

LOCAL BODY RADIUS/BASE RADIUS

0.0 0.0771 0.1325 0.1953 0.2298 0.2208 0.6219 0.6219 0.6219 0.6219 1.0012 1.0012
1.0012

LOCAL MACH NUMBER

0.2018 0.2018 0.5737 0.8170 1.5752 1.8890 1.8890 2.2769 2.2769 1.8010 1.8010 2.2666
2.2666

LOCAL STATIC PRESSURE/TOTAL PRESSURE BEHIND BOW SHOCK

0.9720 0.9720 0.8000 0.6450 0.2441 0.1518 0.1518 0.0829 0.0829 0.1710 0.1710 0.0829
0.0829

LOCAL TOTAL PRESSURE/TOTAL PRESSURE BEHIND BOW SHOCK

1.0000 1.0000 1.0000 1.0000 1.0000 1.0000 1.0000 1.0000 1.0000 0.9840 0.9840 0.9840
0.9840

BOUNDARY LAYER TRANSITION CRITERIA

TRANSITION REYNOLDS NUMBER TO BE DETERMINED BY PROGRAM

LOCATION	S/R	PHI(DEG)	LOCAL VELOCITY (FT/SEC)	LOCAL DENSITY (SLUG/FT CU)	MOMENTUM THICKNESS(FT)	MOMENTUM THICKNESS REYNOLDS NO	LOCAL MOMENTUM DEFECT (SLUG/SEC SQ)
TRANS PT	7.796	0.0	1887.121	0.470803E-04	0.107470E-02	422.6328	0.1802
BASE	9.440	0.0	1882.908	0.468635E-04	0.839094E-03	326.3481	0.1394

TRANSITION OCCURRED AT (S/R) 7.796

FOREBODY BOUNDARY LAYER MOMENTUM DEFECT (LB) 0.117378E 00

WAKE COMPUTATIONS

FOREBODY BOUNDARY LAYER INPUTS

FREE STREAM MACH NO 3.000
 FREE STREAM VELOCITY 2120.681 FT/SEC
 FREE STREAM STATIC TEMP 209.000 DEG R
 TOTAL TEMP 582.399 DEG R
 BODY WALL TEMP 562.000 DEG R
 SPECIFIC HEAT RATIO 1.400
 MFAN BASE RADIUS 0.1340 FT

FOREBODY BASE CONDITION INPUTS

BL MOMENTUM DEFECT 0.117378 LB
 TOTAL PRES AT BODY BASE 278.608 LB/FT SQ
 STATIC PRES AT BODY BASE 23.100 LB/FT SQ

VISCOUS WAKE INPUTS

STARTING PT LOCATION (X0/R) 4.000
 STARTING PT VALUE OF FORM PARAMETER (X1) 22.900

INVISCID WAKE INPUTS

BOW SHOCK SHAPE COEFFICIENTS, $Y/DN = A + B(X/DN) + C(X/DN)**2 + D(X/DN)(Y/DN)$

A	B	C	D	DN
0.503700E-01	0.256668E 01	0.189860E 01	-0.464700E 01	0.166667E 00

WAKE TRANSITION

WAKE IS TURBULENT

VISCOUS WAKE

WAKE X/D STATION 0.00
 VISCOSITY MODEL NO 4
 VISCOSITY COEFF, K 0.02
 ENTHALPY RATIO, K3 1.00

X/D	THETA/DEL	DELTA/DEL	DELTA/D	DELTA*	U1
9.00	0.130149E 00	0.101721E 01	0.435346E 00	0.262763E-01	0.198712E 04

ETA	R/D	U	M	M/MINF	Q/QINF	PT/PINF	RHO/RHOINF	T/TINF
0.0	0.0	0.171950F 04	0.191830F 01	0.639433E 00	0.408875F 00	0.689288F 01	0.330397E 01	0.161293E 01
0.10	0.462007E-01	0.172826F 04	0.193510E 01	0.645032E 00	0.416066E 00	0.707447E 01	0.324317F 01	0.160099E 01
0.20	0.919545E-01	0.174980F 04	0.197717E 01	0.659058E 00	0.434357E 00	0.755166E 01	0.309542E 01	0.157140E 01
0.30	0.134999F 00	0.177799F 04	0.203383E 01	0.677942E 00	0.459605F 00	0.824755E 01	0.290654E 01	0.153232E 01
0.40	0.181189E 00	0.180747F 04	0.209590E 01	0.698634E 00	0.488089E 00	0.908632E 01	0.271225E 01	0.149050E 01
0.50	0.224575E 00	0.183474E 04	0.215547F 01	0.718490E 00	0.516228E 00	0.997303E 01	0.253773E 01	0.145137E 01
0.60	0.267275E 00	0.185709E 04	0.220609F 01	0.735362E 00	0.540757E 00	0.107950E 02	0.239815E 01	0.141890E 01
0.70	0.309486F 00	0.187309F 04	0.224343E 01	0.747810E 00	0.559219E 00	0.114448E 02	0.230009E 01	0.139540E 01
0.80	0.351439E 00	0.188256F 04	0.226596F 01	0.755321E 00	0.570509F 00	0.118556E 02	0.224287E 01	0.138141E 01
0.90	0.393343F 00	0.188650F 04	0.227543E 01	0.758478E 00	0.575288F 00	0.120327E 02	0.221925E 01	0.137557E 01
1.00	0.433346E 00	0.188712E 04	0.227693E 01	0.758976E 00	0.576044E 00	0.120608E 02	0.221555E 01	0.137465E 01

INVISID WAKE

N	R/D	U	M	M/MINF	Q/QINF	PT/PINF	RHO/RHOINF	T/TINF
0.02	0.980458E-01	0.188712F 04	0.227693F 01	0.758977E 00	0.576046E 00	0.120609E 02	0.221554E 01	0.137465E 01
0.10	0.351030F 00	0.211040F 04	0.295991F 01	0.986604E 00	0.973387E 00	0.345799E 02	0.104408E 01	0.101741E 01
0.18	0.671161F 00	0.211943E 04	0.299506E 01	0.998353E 00	0.996708E 00	0.364615E 02	0.100531E 01	0.100212F 01
0.25	0.955080F 00	0.212001F 04	0.299734F 01	0.999112E 00	0.998224E 00	0.365863E 02	0.100286E 01	0.100114E 01
0.33	0.124094F 01	0.212014F 04	0.299796F 01	0.999288E 00	0.998576E 00	0.366153F 02	0.100229E 01	0.100092E 01
0.41	0.152771F 01	0.212019E 04	0.299806F 01	0.999355E 00	0.998710E 00	0.366264E 02	0.100208E 01	0.100083E 01
0.48	0.181497F 01	0.212022E 04	0.299816E 01	0.999398E 00	0.998776E 00	0.366318E 02	0.100197E 01	0.100079E 01
0.56	0.210251E 01	0.212023E 04	0.299822F 01	0.999406E 00	0.998812E 00	0.366348F 02	0.100191E 01	0.100076E 01
0.64	0.239025F 01	0.212024E 04	0.299825E 01	0.999417E 00	0.998834E 00	0.366367E 02	0.100187E 01	0.100075E 01
0.72	0.267812F 01	0.212025E 04	0.299828E 01	0.999425E 00	0.998851F 00	0.366380E 02	0.100185F 01	0.100074E 01
0.79	0.296607F 01	0.212025F 04	0.299829E 01	0.999431F 00	0.998861E 00	0.366388E 02	0.100183E 01	0.100073E 01
0.87	0.325410F 01	0.212025F 04	0.299830E 01	0.999435E 00	0.998870E 00	0.366395E 02	0.100182E 01	0.100073E 01
0.95	0.354217F 01	0.212025F 04	0.299831F 01	0.999437E 00	0.998875E 00	0.366400E 02	0.100181E 01	0.100072E 01
1.03	0.383029F 01	0.212026F 04	0.299832E 01	0.999439E 00	0.998879E 00	0.366403E 02	0.100180E 01	0.100072E 01
1.10	0.411843F 01	0.212026E 04	0.299832F 01	0.999441E 00	0.998882E 00	0.366405E 02	0.100180E 01	0.100072E 01
1.18	0.440661F 01	0.212026F 04	0.299833E 01	0.999442E 00	0.998885E 00	0.366407E 02	0.100179E 01	0.100072E 01
1.26	0.459490F 01	0.212026F 04	0.299833F 01	0.999443E 00	0.999886E 00	0.366409E 02	0.100179E 01	0.100072E 01
1.33	0.498301E 01	0.212026E 04	0.299833E 01	0.999444E 00	0.999888F 00	0.366411E 02	0.100179E 01	0.100071E 01
1.41	0.527124F 01	0.212026F 04	0.299834E 01	0.999446E 00	0.998891E 00	0.366412E 02	0.100178E 01	0.100071E 01
1.49	0.555347F 01	0.212026F 04	0.299834E 01	0.999446E 00	0.998892E 00	0.366414E 02	0.100178E 01	0.100071E 01
1.57	0.584727F 01	0.212026E 04	0.299834F 01	0.999447E 00	0.998894E 00	0.366415E 02	0.100178E 01	0.100071E 01

VISCOS WAKE

WAKE X/D STATION 11.00
 VISCOSITY MODEL NO 4
 VISCOSITY COEFF, K 0.02
 ENTHALPY RATIO, K2 1.00

X/D	THETA/DEL	DELTA/DEL	DELTA/D	DELTA*	U1
11.00	0.123251E 00	0.101466F 01	0.469976E 00	0.262115F-01	0.188712E 04

ETA	R/D	U	M	M/MINF	Q/QINF	PT/PINF	RHO/RHOINF	T/TINF
0.0	0.0	0.174508F 04	0.196785E 01	0.555950E 00	0.430269E 00	0.744308F 01	0.312761E 01	0.157792E 01
0.10	0.494809E-01	0.175251F 04	0.198254E 01	0.660849E 00	0.436720E 00	0.761493E 01	0.307703E 01	0.156766E 01
0.20	0.985419E-01	0.177076E 04	0.201926E 01	0.673087E 00	0.453046E 00	0.806254E 01	0.295402E 01	0.154229E 01
0.30	0.146928F 00	0.179455E 04	0.206350E 01	0.689499E 00	0.475408F 00	0.870573F 01	0.279643E 01	0.150883E 01
0.40	0.194537E 00	0.181962F 04	0.212217E 01	0.707389E 00	0.500399E 00	0.946698E 01	0.263390E 01	0.147313E 01
0.50	0.241391E 00	0.184273F 04	0.217339E 01	0.724463E 00	0.524847E 00	0.102566E 02	0.248742E 01	0.143979E 01
0.60	0.297611E 00	0.186167E 04	0.221659E 01	0.738997E 00	0.545968E 00	0.109757E 02	0.236989E 01	0.141218E 01
0.70	0.333382E 00	0.187573F 04	0.224850F 01	0.749498F 00	0.561748F 00	0.115359E 02	0.228710E 01	0.139224E 01
0.80	0.379918E 00	0.188326F 04	0.226763E 01	0.755877E 00	0.571350F 00	0.118867F 02	0.223869E 01	0.138038E 01
0.90	0.424411F 00	0.189660F 04	0.227566E 01	0.758554E 00	0.575404F 00	0.120370E 02	0.221868E 01	0.137543E 01
1.00	0.469996E 00	0.188712E 04	0.227693F 01	0.758976E 00	0.576044F 00	0.120608F 02	0.221555E 01	0.137465E 01

INVISID WAKE

N	R/D	U	M	M/MINF	Q/QINF	PT/PINF	RHO/RHOINF	T/TINF
0.02	0.978243E-01	0.188717F 04	0.227693E 01	0.758977E 00	0.576046E 00	0.120609F 02	0.221554E 01	0.137465E 01
0.11	0.430893E 00	0.211418F 04	0.297445E 01	0.991484F 00	0.983040F 00	0.353502E 02	0.102778E 01	0.101102E 01
0.20	0.751522F 00	0.211971E 04	0.299616F 01	0.998720E 00	0.997441E 00	0.365219E 02	0.100412E 01	0.100165E 01
0.29	0.107660F 01	0.212008E 04	0.299763E 01	0.999211E 00	0.998422F 00	0.366026E 02	0.100254E 01	0.100101E 01
0.37	0.140355F 01	0.212017F 04	0.299800E 01	0.999332E 00	0.998664F 00	0.366226F 02	0.100215E 01	0.100086E 01
0.46	0.173135F 01	0.212071F 04	0.299914F 01	0.999380E 00	0.998761F 00	0.366305E 02	0.100199E 01	0.100080E 01
0.55	0.205960F 01	0.212023F 04	0.299821E 01	0.999405F 00	0.998809F 00	0.366345F 02	0.100192E 01	0.100077E 01
0.64	0.239812E 01	0.212024F 04	0.299825E 01	0.999417E 00	0.998834E 00	0.366366E 02	0.100187E 01	0.100075E 01
0.73	0.271681E 01	0.212025F 04	0.299828F 01	0.999426E 00	0.998852E 00	0.366381E 02	0.100184E 01	0.100074E 01
0.81	0.304562F 01	0.212025F 04	0.299830F 01	0.999432E 00	0.998864F 00	0.366390F 02	0.100183F 01	0.100073E 01
0.90	0.337452E 01	0.212025F 04	0.299831E 01	0.999436F 00	0.998871E 00	0.366397E 02	0.100181E 01	0.100072E 01
0.99	0.370347E 01	0.212026F 04	0.299831E 01	0.999438E 00	0.998876E 00	0.366401E 02	0.100181F 01	0.100072E 01
1.08	0.403247E 01	0.212026F 04	0.299832F 01	0.999441E 00	0.998882F 00	0.366405F 02	0.100180E 01	0.100072E 01
1.17	0.436151F 01	0.212026F 04	0.299833E 01	0.999442E 00	0.998885F 00	0.366408F 02	0.100179E 01	0.100072E 01
1.26	0.469058F 01	0.212026F 04	0.299833E 01	0.999444E 00	0.998888E 00	0.366410E 02	0.100179E 01	0.100071E 01
1.34	0.501967F 01	0.212026F 04	0.299833E 01	0.999445E 00	0.998890E 00	0.366412E 02	0.100178E 01	0.100071E 01
1.43	0.534878F 01	0.212026F 04	0.299834F 01	0.999446E 00	0.998891F 00	0.366413E 02	0.100178E 01	0.100071E 01
1.52	0.567790F 01	0.212026F 04	0.299834F 01	0.999447E 00	0.998894E 00	0.366414E 02	0.100178E 01	0.100071E 01
1.61	0.600704F 01	0.212026F 04	0.299834F 01	0.999447E 00	0.998894E 00	0.366415F 02	0.100178E 01	0.100071E 01
1.70	0.633618F 01	0.212026F 04	0.299834E 01	0.999447E 00	0.998894E 00	0.366415E 02	0.100178E 01	0.100071E 01
1.79	0.666534E 01	0.212026F 04	0.299834F 01	0.999447E 00	0.998895E 00	0.366416E 02	0.100178E 01	0.100071E 01



LIST OF SYMBOLS

A	coefficient in shock shape equation, Equation (85)
a	sonic velocity, ft/sec
a_i	coefficients in velocity profile, Equation (21)
B	temperature function, Equation (102)
c_p	heat capacity at constant pressure
c_v	heat capacity at constant volume
D	maximum body diameter (axisymmetric) or height (two-dimensional), inches
d	water depth, inches
Fr	froude number (ratio of water velocity to surface wave propagation velocity)
h	enthalpy
H	total enthalpy
j	$j = 0$, two-dimensional flow; $j = 1$, axisymmetric flow
K	turbulence constant, Equation (43)
L	body length; characteristic length, inches
ℓ	length, inches; constant, Equation (43)
ℓ'	body length from nose to plane containing sonic point
M	Mach number; momentum
m	constant, Equation (43); transformed coordinate, Equation (57)
n	constant, Equation (43); transformed coordinate, Equation (18); exponent in shock shape equation, Equation (85)
p	pressure
Pr	Prandtl number
R	configuration radius (axisymmetric) or height (two-dimensional), inches

R_B	radial dimension of body in plane containing body sonic point
Re	Reynolds number
R_1	gas constant
r	radial coordinate (axisymmetric) or transverse coordinate (two-dimensional); radius
r_s	distance from axis of symmetry to bow wave measured normal to axis
S	detached bow wave standoff distance
s	distance from stagnation point measured along the body surface; enthalpy
T	temperature
U	free stream turbulence parameter
u	axial velocity component
V	velocity
v	radial velocity component
x	axial coordinate; axial wake coordinate
y	lateral coordinate in tow channel
$Z_{1,2...6}$	dummy parameters, Equations (87) and (88)
α	angle of attack, degrees
β	stream tube deflection at a given free-stream Mach number; pressure gradient parameter, Equation (90)
γ	specific heat ratio
Δ	transformed wake radius or thickness, Equation (19); quantity increment
δ	wedge semiapex angle, degrees; wake radius or thickness
δ_B	boundary layer thickness
δ_D	wake diameter or thickness ($\delta_D = 2$)
δ^*	wake displacement thickness

δ_m^*	transformed wake displacement thickness, Equation (58)
ϵ	trailing wave divergence half angle, degrees
η	nondimensional transformed radial coordinate, Equation (20)
θ	bow wave angle, degrees; momentum thickness, inches
θ_T	enthalpy thickness
μ	Mach angle, degrees; dynamic viscosity
ν	kinematic viscosity
ξ	wake form factor, Equation (23), laminar boundary layer form factor, Equation (90)
ξ^*	laminar boundary layer form parameter, Equation (92)
ξ_T^*	turbulent boundary layer form parameter, Equation (77) and (78)
ρ	density
ϕ	meridian angle, <u>e.g.</u> , Equation (99)

Subscripts:

aw	adiabatic wall
B	base
G_L	centerline
e	edge of forebody boundary layer
K	integer, Equation (59)
L	local condition, characteristic length reference
m	conditions in transformed coordinate system, <u>e.g.</u> , Equation (58)
n	body nose
o	stagnation conditions; wake centerline conditions; wake starting point (wake neck or rear stagnation point)
p	pitot pressure
s	base shoulder; bow shock coordinate
t	total conditions

tr	transformation conditions
w	wall conditions
θ	momentum thickness condition
ϕ	meridian angle, <u>e.g.</u> , Equation (114)
1	reference conditions forward of shock wave or hydraulic jump; wake edge conditions
2	reference conditions behind shock wave or hydraulic jump
∞	free stream conditions

LIST OF REFERENCES

- Orlin, W. J.; Lindner, N. J.; and Bitterly, J. G.: Application of The Analogy Between Water Flow With A Free Surface And Two-Dimensional Compressible Gas Flow. NACA Rept. 875, 1947.
- Moeckel, W. E.: Approximate Method for Predicting Form and Location of Detached Shock Waves Ahead of Plane or Axially Symmetric Bodies. NACA TN 1921, 1949.
- Babish, C. A.: Drag Level Staging Through Modification of Supersonic Wake Fields By Trailing Aerodynamic Decelerators. Paper presented at the AIAA Aerodynamic Deceleration System Conference, Houston, Texas, Sept. 7-9, 1966, pp. 55-63.
- Babish, C. A.: Equations, Tables, and Charts for Flow of Shallow-Water With a Free Surface. AFFDL-TM-69-2-FDFR, April 1969.
- Henke, D. W.: Establishment of an Unsymmetrical Wake Test Capability for Aerodynamic Decelerators, Vol. II, Analysis of High Speed Axisymmetric Wakes and PARASONIC Parachute Performance. Technical Report AFFDL-TR-67-192, Goodyear Aerospace Corporation, March 1968.
- Kemp, N. H.; Rose, P. H.; and Detra, R. W.: Laminar Heat Transfer Around Blunt Bodies in Dissociated Air. Rep. RR 15, Avco-Everett Research Laboratory, May 1968.
- Reshotko, E.; and Tucker, M: Approximate Calculation of the Compressible Turbulent Boundary Layer with Heat Transfer and Arbitrary Pressure Gradient. NACA Rep. TN 4154, December 1957.
- Schlichting, H. (J. Kestin, trans): Boundary Layer Theory. McGraw-Hill Book Co., Inc., Fourth Edition, 1960.
- Nerem, R. M.; and Henke, D. W.: Theoretical and Experimental Studies of Supersonic Turbulent Wakes and Parachute Performance. Paper presented at the AIAA 2nd Aerodynamic Deceleration Systems Conference, Sept 23-25, 1968 at El Centro, California.
- Batt, R. G.; and Kubota, T.: Experimental Investigation of Far Wakes Behind Two-Dimensional Slender Bodies at $M_{\infty} = 6$. AIAA Paper No. 68-700 presented at the AIAA Fluid and Plasma Dynamics Conference at Los Angeles, California, June 24-26, 1968.
- Zakkay, V.; and Fox, H.: An Experimental and Theoretical Investigation of the Turbulent Far Wake. AIAA Journal, Vol. 5, No. 3, March 1967, pp. 568-574.

12. Nerem, R. M.: An Approximate Method for Including the Effect of the Inviscid Wake on the Pressure Distribution on a Ballute-Type Decelerator. Rep. GER-11824, Goodyear Aerospace Corporation, November 1964.
13. Nerem, R. M.: Pressure and Heat Transfer on High-Speed Aerodynamic Decelerators of the BALLUTE Type. Proceedings of the AIAA Aerodynamic Systems Deceleration Conference, Houston, Texas, September 7-9, 1966.
14. Harleman, D. R. F.: Studies On The Validity Of The Hydraulic Analogy To Supersonic Flow, Parts I and II. A.F. Technical Rep. No. 5985, May 1950.
15. Moeckel, W. E.: Experimental Investigation of Supersonic Flow with Detached Shock Waves for Mach Numbers between 1.8 and 2.9. NACA RM E50D05, July 1950.
16. Campbell, J.; Grow, J.W.: Experimental Flow Properties for the Value of a 120-Degree Cone at Mach 2.2. NASA TN D-5365, 1969.
17. McShera, J. T.: Wind-Tunnel Pressure Measurements In The Wake of A Cone-Cylinder Model At Mach Numbers of 2.30 and 4.65. NASA TN D-2928, August 1965.
18. Henke, D. W.: Establishment of An Unsymmetrical Wake Test Capability For Aerodynamic Decelerators, Volume III, Experimental Wake Survey and Body Surface Pressure Data. AFFDL-TR-67-192, August 1968.
19. Stetson, K. F.: Boundary-Layer Transition on Blunt Bodies with Highly Cooled Boundary Layers. J. Aeron. Sci., Vol 27, No. 2, February 1960 pp 81-91.
20. Low, M.: Boundary-Layer Transition at Supersonic Speeds. NACA RM E56E10, 1956.
21. Gazley, C., Jr.: Boundary Layer Stability and Transition in Supersonic Flow. J. Aeron. Sci., January 1953.
22. Stainback, C. P.: Some Effects of Roughness and Variable Entropy on Transition at a Mach Number of 8. AIAA Paper No. 67-132.
23. Deem, R. E.: Boundary Layer Transition at Hypersonic Speeds. SM-43056, January 1964.
24. Stewart, D. G.: Some Observations of Boundary Layer Transition on Cones at Subsonic and Supersonic Speeds. ARL/ME-267, May 1965.

25. Korkegi, R. : Transition Studies and Skin Friction Measurements on an Insulated Flat Plate at a Mach Number of 5.8. J. Aeron. Sci., Vol 25, No. 2, February 1956, p 97.
26. Nagamatsu, H. T.; Sheer, R. E.; and Graber B.C. : Hypersonic Laminar Boundary Layer Transition on an Eight-Foot Long, Ten-Degree Cone, $M_1 = 9.1 - 16$. AIAA Paper No. 66-494 presented at the 4th Aerospace Sciences Meeting, Los Angeles, June 1966.
27. Braslow, A. L. : A Review of Factors Affecting Boundary Layer Transition. NASA TN D-3384, August 1966.
28. Diaconis, N. S.; Wisniewski, R. J.; and Jack, J. R. : Heat Transfer and Boundary Layer Transition on Two Blunt Bodies at Mach Number 3.12. NACA TN 4099, October 1957.
29. Stetson, K. F. : Boundary Layer Transition on Blunt Bodies with Highly Cooled Boundary Layers. J. Aeron. Sci., Vol 27, No. 2, December 1957, p. 885.
30. Van Driest, E. R.; and Boison, J. C. : Experiments on Boundary Layer Transition at Supersonic Speeds. J. Aeron. Sci., Vol 24, No. 12, December 1957, p. 885.
31. Reshotko, E. : Transition Reversal and Tollmien-Schlichting Instability. Phys. Fluids, Vol 6, No. 3, March 1963, p. 335.
32. Stetson, K. F.; and Rushton, G. H. : A Shock Tunnel Investigation of the Effects of Nose Bluntness, Angle of Attack and Boundary Layer Cooling on Boundary Layer Transition at a Mach Number of 5.5. AIAA Paper No. 66-495 presented at the AIAA 4th Aerospace Sciences Meeting, Los Angeles, June 1966.